

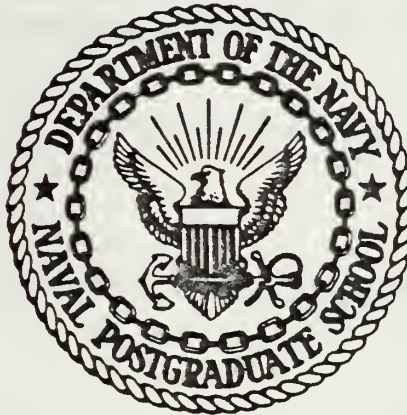
THE INFLUENCE OF THERMOMECHANICAL PROCESSING  
AND HEAT TREATMENT ON THE FATIGUE RESISTANCE  
AND FRACTOGRAPHIC CHARACTERISTICS OF  
A HIGH-CARBON BEARING STEEL

Ik Sik Chung



# NAVAL POSTGRADUATE SCHOOL

## Monterey, California



# THESIS

THE INFLUENCE OF THERMOMECHANICAL PROCESSING  
AND HEAT TREATMENT ON THE FATIGUE RESISTANCE  
AND FRACTOGRAPHIC CHARACTERISTICS OF  
A HIGH-CARBON BEARING STEEL

by

Ik Sik Chung

December 1979

Thesis Advisor:

Donald H. Boone

Approved for public release; distribution unlimited

Prepared for:

Naval Sea Systems Command  
Washington, DC

T197027

NAVAL POSTGRADUATE SCHOOL  
Monterey, California

Rear Admiral T. F. Dedman  
Superintendent

Jack R. Borsting  
Provost

This thesis prepared in conjunction with research supported in part by the Naval Sea Systems Command under work request N0002479-WR9G078.

Reproduction of all of part of this report is authorized.



REPORT DOCUMENTATION PAGE		READ INSTRUCTIONS BEFORE COMPLETING FORM
1. REPORT NUMBER NPS 69-79-012	2. GOVT ACCESSION NO.	3. RECIPIENT'S CATALOG NUMBER
4. TITLE (and Subtitle) The Influence of Thermomechanical Processing and Heat Treatment on the Fatigue Resistance and Fractographic Characteristics of a High-Carbon Bearing Steel		5. TYPE OF REPORT & PERIOD COVERED Master's Thesis; December 1979
7. AUTHOR(s) Ik Sik Chung		6. PERFORMING ORG. REPORT NUMBER
9. PERFORMING ORGANIZATION NAME AND ADDRESS Naval Postgraduate School Monterey, California 93940		8. CONTRACT OR GRANT NUMBER(s)
11. CONTROLLING OFFICE NAME AND ADDRESS Naval Postgraduate School Monterey, California 93940		10. PROGRAM ELEMENT, PROJECT, TASK AREA & WORK UNIT NUMBERS  N0002479-WR9GO78
14. MONITORING AGENCY NAME & ADDRESS (if different from Controlling Office)		12. REPORT DATE December 1979
		13. NUMBER OF PAGES 119 pages
		15. SECURITY CLASS. (of this report) Unclassified
		15a. DECLASSIFICATION/DOWNGRADING SCHEDULE
16. DISTRIBUTION STATEMENT (of this Report) Approved for public release; distribution unlimited		
17. DISTRIBUTION STATEMENT (of the abstract entered in Block 20, if different from Report)		
18. SUPPLEMENTARY NOTES		
19. KEY WORDS (Continue on reverse side if necessary and identify by block number) AISI 52100 Steel, Thermomechanical processing, fatigue resistance, high carbon bearing steel		
20. ABSTRACT (Continue on reverse side if necessary and identify by block number) This study examined the effects of thermomechanical processing and subsequent conventional heat treatment on microstructure and fatigue in AISI 52100 steel. The thermomechanical processing techniques are essentially those described by Sherby and his co-workers at Stanford University. Previous research by that group and at the Naval Postgraduate School has demonstrated that a wide range of ferrite matrix grain sizes and carbide particle distributions can be obtained in this steel. Studies parallel with this		



are examining the subsequent heat treatment response of these structures and also the fracture toughness attainable. In this study on fatigue, it was found that both the fatigue life at a given cyclic stress and the endurance limit were improved by processing to produce an ultra-fine grained ferrite-carbide microstructure prior to heat treatment. Improvement in fatigue resistance was especially pronounced when the material was heat treated to fine Bainitic, rather than Martensitic microstructures. These improvements are postulated to result from changes in crack propagation mode and improved resistance to fatigue crack propagation.



Approved for public release; distribution unlimited

The Influence of Thermomechanical Processing  
and Heat Treatment on the Fatigue Resistance  
and Fractographic Characteristics of  
a High-Carbon Bearing Steel

by

Ik Sik Chung  
Commander, Republic of Korea Navy  
B.A., R.O.K. Naval Academy, 1967  
B.S. in Metallurgy, Seoul National University, 1970 •

Submitted in partial fulfillment of the  
requirements for the degree of

MASTER OF SCIENCE IN ENGINEERING SCIENCE

from the

NAVAL POSTGRADUATE SCHOOL  
December 1979

1912

CHYRE

oil



## ABSTRACT

This study examined the effects of thermomechanical processing and subsequent conventional heat treatment on microstructure and fatigue in AISI 52100 steel. The thermomechanical processing techniques are essentially those described by Sherby and his co-workers at Stanford University. Previous research by that group and at the Naval Postgraduate School has demonstrated that a wide range of ferrite matrix grain sizes and carbide particle distributions can be obtained in this steel. Studies parallel with this are examining the subsequent heat treatment response of these structures and also the fracture toughness attainable. In this study on fatigue, it was found that both the fatigue life at a given cyclic stress and the endurance limit were improved by processing to produce an ultra-fine grained ferrite-carbide microstructure prior to heat treatment. Improvement in fatigue resistance was especially pronounced when the material was heat treated to fine Bainitic, rather than Martensitic microstructures. These improvements are postulated to result from changes in crack propagation mode and improved resistance to fatigue crack propagation.



## TABLE OF CONTENTS

I.	INTRODUCTION-----	14
A.	PURPOSE-----	14
B.	BACKGROUND-----	14
C.	PREVIOUS RESEARCH-----	16
D.	FATIGUE FAILURE OF METALS-----	18
II.	EXPERIMENTAL PROCEDURE-----	22
A.	MATERIAL PREPARATION-----	22
B.	FACILITIES USED-----	22
	1. General-----	22
	2. Rolling-----	23
	3. Tensile and Hardness Testing-----	24
	4. Heat Treating-----	24
	5. Fatigue Testing-----	25
	6. Microstructural and Fractographic Analysis--	26
C.	THERMAL-MECHANICAL PROCESSING-----	26
	1. Specimen Group AR (As Rolled)-----	26
	2. Specimen Group QT (Quenched and Tempered)---	29
	3. Specimen Group RQ (Rolled, Quenched and Tempered)-----	33
	4. Specimen Group QI (Quenched and Isothermally Transformed)-----	33
	5. Specimen Group RI (Rolled and Isothermally Transformed)-----	35
D.	SPECIMEN PREPARATION-----	35
	1. Tensile Test Specimen-----	35
	2. Fatigue Test Specimen-----	38
	3. Micrograph and Fractograph Test Specimen---	40
IV.	RESULTS -----	41
A.	MECHANICAL TESTING RESULTS-----	41
	1. Hardness Testing Results-----	41
	2. Tensile Testing Results-----	41
	3. Fatigue Testing Results-----	42
B.	MICROSTRUCTURAL AND FRACTOGRAPHIC RESULTS-----	53
	1. Specimen Group AR-----	53
	2. Specimen Group QT-----	73
	3. Specimen Group QI-----	78
	4. Specimen Group RQ-----	84



5.	Specimen Group RI-1-----	88
6.	Specimen Group RI-2-----	95
7.	Tensile Test Specimen-----	104
IV.	DISCUSSION-----	108
A.	GENERAL-----	108
B.	EFFECTS OF THERMOMECHANICAL PROCESSING ON MICROSTRUCTURE AND MECHANICAL PROPERTIES-----	108
V.	CONCLUSIONS-----	115
VI.	RECOMMENDATIONS FOR FURTHER RESEARCH-----	116
.	LIST OF REFERENCES-----	117
	INITIAL DISTRIBUTION LIST-----	119





## LIST OF TABLES

I.	Results of Mechanical Testing-----	43
II.	Comparison of Fatigue Performance of Each Specimen--	55
III.	Comparison of Fractograph of Each Specimen Group----	103



## LIST OF FIGURES

1.	Fatigue Test Machine-----	27
2.	Isothermal-Mechanical Processing of AR Specimen Group-----	30
3.	Heat Treatment Process of Specimen Group QT-----	34
4.	Heat Treatment Process of Specimen Group RQ-----	34
5.	Heat Treatment Process of Specimen Group QI-----	36
6.	Heat Treatment Process of Specimen Group RI-1-----	36
7.	Heat Treatment Process of Specimen Group RI-2-----	36
8.	Tensile Test Specimen-----	37
9.	Fatigue Test Specimen-----	37
10.	Macrograph of Fatigue Test Specimen Surface x70-----	39
11.	Macro-Fractograph of Tensile Test Specimen Group RI-2 x20-----	44
12.	SEM Fractograph of Tensile Test Specimen Group RI-2 x 1,000-----	44
13.	SEM Fractograph of Tensile Test Specimen Group RI-2 x2,000-----	45
14.	SEM Fractograph of Tensile Test Specimen Group RI-2 x1,000-----	45
15.	SEM Fractograph of Tensile Test Specimen Group RI-2 x2,000-----	46
16.	S-N Curves of Specimen Groups AR-1 and AR-5-----	48
17.	S-N Curves of Specimen Groups AR-2, AR-3 and AR-4---	49
18.	S-N Curves of Specimen Groups QT and RQ-----	51
19.	S-N Curves of Specimen Groups QI, RI-1 and RI-2-----	52
20.	S-N Curves of Specimen Groups AR-5 and RI-2-----	54
21.	Macro-Fractograph of Specimen AR-2-1 x10-----	56



22.	SEM Fractograph of Specimen AR-2-1 x100-----	56
23.	SEM Fractograph of Specimen AR-2-1 x1,000-----	57
24.	SEM Fractograph of Specimen AR-2-1 x2,000-----	57
25.	SEM Fractograph of Specimen AR-2-1 x1,000-----	58
26.	SEM Fractograph of Specimen AR-2-1 x2,000-----	58
27.	Macro-Fractograph of Specimen AR-3-5 x10-----	59
28.	SEM Fractograph of Specimen AR-3-5 x1,000-----	60
29.	SEM Fractograph of Specimen AR-3-5 x1,000-----	60
30.	SEM Fractograph of Specimen AR-3-7 x1,000-----	61
31.	SEM Fractograph of Specimen AR-3-7 x1,200-----	61
32.	SEM Fractograph of Specimen AR-3-7 x2,400-----	62
33.	SEM Fractograph of Specimen AR-3-7 x1,200-----	62
34.	SEM Fractograph of Specimen AR-3-7 x2,400-----	63
35.	SEM Microstructure of Specimen AR-3-7 x5,000-----	63
36.	Macro-Fractograph of Specimen AR-4-9 x10-----	64
37.	SEM Fractograph of Specimen AR-4-9 x1,050-----	64
38.	SEM Fractograph of Specimen AR-4-9 x5,300-----	65
39.	Macro-Fractograph of Specimen AR-4-10 x10-----	65
40.	SEM Fractograph of Specimen AR-4-10 x2,400-----	66
41.	SEM Fractograph of Specimen AR-4-10 x5,000-----	66
42.	Microstructure of Specimen AR-4-10 x100-----	67
43.	Microstructure of Specimen AR-4-10 x400-----	67
44.	Macro-Fractograph of Specimen AR-1-2 x10-----	68
45.	Macro-Fractograph of Specimen AR-1-3 x10-----	68
46.	SEM Fractograph of Specimen AR-1-3 x500-----	69
47.	SEM Fractograph of Specimen AR-1-3 x1,000-----	69
48.	Macro-Fractograph of Specimen AR-5-5 x10-----	70





49.	SEM Fractograph of Specimen AR-5-5 x500-----	70
50.	SEM Fractograph of Specimen AR-5-5 x1,000-----	71
51.	SEM Fractograph of Specimen AR-5-5 x1,000-----	71
52.	SEM Fractograph of Specimen AR-5-5 x2,000-----	72
53.	Microstructure of Specimen QT-0-3 x400-----	74
54.	Macro-Fractograph of Specimen QT-0-8 x10-----	74
55.	Macro-Fractograph of Specimen QT-0-1 x10-----	75
56.	Macro-Fractograph of Specimen QT-0-5 x10-----	75
57.	SEM Fractograph of Specimen QT-0-3 x1,000-----	76
58.	SEM Fractograph of Specimen QT-0-3 x5,000-----	76
59.	SEM Fractograph of Specimen QT-0-6 x1,000-----	77
60.	SEM Fractograph of Specimen QT-0-6 x5,000-----	77
61.	Macro-Fractograph of Specimen QI-0-5 x10-----	79
62.	Macro-Fractograph of Specimen QI-0-7 x10-----	79
63.	SEM Fractograph of Specimen QI-0-3 x1,000-----	80
64.	SEM Fractograph of Specimen QI-0-3 x5,000-----	80
65.	SEM Fractograph of Specimen QI-0-5 x100-----	81
66.	SEM Fractograph of Specimen QI-0-5 x1,000-----	81
67.	SEM Fractograph of QI-0-8 x1,000-----	82
68.	SEM Fractograph of QI-0-8 x2,000-----	82
69.	Microstructure of Specimen QI-0-7 x400-----	83
70.	Macro-Fractograph of Specimen RQ-0-1 x20-----	85
71.	Macro-Fractograph of Specimen RQ-0-2 x10-----	85
72.	Microstructure of Specimen RQ-0-1 x400-----	86
73.	Microstructure of Specimen RQ-0-1 x1,200-----	86
74.	SEM Fractograph of Specimen RQ-0-1 x1,200-----	87
75.	SEM Fractograph of Specimen RQ-0-1 x5,000-----	87



76.	Macro-Fractograph of Specimen RI-1-1 x10-----	89
77.	Macro-Fractograph of Specimen RI-1-2 x10-----	89
78.	Macro-Fractograph of Specimen RI-1-4 x10-----	90
79.	Macro-Fractograph of Specimen RI-1-6 x10-----	90
80.	SEM Fractograph of Specimen RI-1-1 x55-----	91
81.	SEM Fractograph of Specimen RI-1-1 x2,200-----	91
82.	SEM Fractograph of Specimen RI-1-1 x2,200-----	92
83.	SEM Fractograph of Specimen RI-1-1 x1,020-----	92
84.	SEM Fractograph of Specimen RI-1-1 x2,000-----	93
85.	SEM Fractograph of Specimen RI-1-1 x5,000-----	93
86.	Microstructure of Specimen RI-1-1 x100-----	94
87.	Microstructure of Specimen RI-1-1 x400-----	94
88.	Macro-Fractograph of Specimen RI-2-2 x10-----	96
89.	Macro-Fractograph of Specimen RI-2-5 x10-----	96
90.	Macro-Fractograph of Specimen RI-2-6 x10-----	97
91.	Macro-Fractograph of Specimen RI-2-3 x10-----	97
92.	Microstructure of Specimen RI-2-3 x100-----	98
93.	Microstructure of Specimen RI-2-3 x400-----	98
94.	SEM Fractograph of Specimen RI-2-3 x1,100-----	99
95.	SEM Fractograph of Specimen RI-2-3 x2,000-----	99
96.	SEM Fractograph of Specimen RI-2-3 x2,000-----	100
97.	Micrograph of Secondary Crack of Specimen RI-2-8 x100-----	101
98.	Micrograph of Secondary Crack of Specimen RI-2-8 x400-----	101
99.	Micrograph of Secondary Crack of Specimen RI-2-8 x400-----	102
100.	Macro-Fractograph of Tensile Specimen Group RQ x18--	105
101.	SEM Fractograph of Tensile Specimen Group RQ x200--	105



102.	SEM Fractograph of Tensile Specimen Group RQ x1,000-	106
103.	SEM Fractograph of Tensile Specimen Group RQ x5,000-	106
104.	SEM Fractograph of Tensile Specimen Group RQ x500---	107
105.	SEM Fractograph of Tensile Specimen Group RQ x1,000-	107
106.	Plot of Endurance Limit Versus Hardness-----	110
107.	Plot of Cycles to Failure Versus Hardness-----	113
108.	Micrograph of Quenching Crack of Specimen Group AR-3 x400-----	114





## ACKNOWLEDGMENT

I wish to express my deep appreciation to Professor Donald H. Boone and Professor Terry R. McNelley for the many hours of guidance and assistance they gave me, Mr. Tom Kellogg and John Moulton for their support, and my wife, In Sook, for her efforts in heat treating and overall moral support, and to the Naval Postgraduate School Foundation whose financial support for specimen preparation and for fatigue machine equipment made this study possible.



## I. INTRODUCTION

### A. PURPOSE

The purpose of this research was to characterize the fatigue properties of an extensively warm-worked high carbon steel, AISI 52100, both as-rolled and with subsequent heat treatment, and to establish the relationship between the resulting mechanical properties and microstructure for this material. This effort is part of ongoing research at the Naval Postgraduate School (NPS) into the structural, mechanical and ballistic properties of this steel. This work follows that of Goesling [1], Hamilton and Rowe [2], Hillier [3], Martin and Phillips [4], and Taylor [5], who emphasized the mechanical and the ballistic characteristics of these materials.

The ultimate goal of this research effort is to understand the mechanical, microstructural, processing and compositional variables which govern the desired mechanical properties of this unique class of materials, the high carbon steels. It is believe that this understanding will lead to eventual utilization of these warm-worked high carbon and ultra-high carbon steels in important application such as armor in military use and as an improved bearing material.

### B. BACKGROUND

High-carbon steels are normally those containing 0.6 to 1.0 weight % carbon. Cast irons typically contain from about 2.1% carbon up to about 4.5% carbon.



Ultra-high carbon (UHC) steels can be defined as occupying the composition range between the high-carbon steels and the cast irons, i.e., from 1.0 percent to about 2.0 percent carbon.

In the past, high-carbon and UHC steels have been considered brittle materials, suitable for applications such as simple tools or bearing plates, where high hardness and wear resistance are important but little ductility or ability to absorb plastic deformation or impact loads are required.

The NPS research effort is an outgrowth of a discovery by Professor Oleg Sherby of the Department of Materials Science and Engineering at Stanford University, that a microstructure consisting of a fine, particulate distribution of spheroidal carbide in a fine ferrite matrix can be obtained [6]. This kind of microstructure results from extensive warm-working of UHC steels (usually by rolling) while cooling through the austenite plus carbide region of the phase diagram, followed by isothermally working the material below the  $A_1$  temperature. This microstructure results in a steel with both high strength and high ductility. These steels also exhibit superplasticity at temperatures slightly below the eutectoid temperature ( $A_1$ ), with fracture elongations up to 1100%. When these steels are subsequently austenitized at a temperature slightly above the eutectoid and then quenched, a fine-grained martensite plus fine, spheroidal carbide microstructure results [7]. This microstructure suggests a material which can have a high resistance to unstable crack propagation combined with high strength and a high fatigue limit. It should be emphasized that such microstructures also exhibit high



hardnesses (HRC >60). Conventional heat treatment of such high carbon and UHC steels can produce a similar hardness but with a coarser, less crack-resistant microstructure.

### C. PREVIOUS RESEARCH

The NPS research effort involving high-carbon and UHC steels was started by Lieutenant Commander William Goesling under the guidance of Professor Terry R. McNelley. The interest in these steels was centered on their potential use as armor material, where hardness and toughness are prime requirements. This initial effort resulted in the fabrication of the NPS Ballistic Test Facility and the establishment of procedures for data collection. The initial test results indicated that AISI 52100 steel, when processed following the Sherby method, compared favorably with existing armors [1].

Ballistic examination of the 52100 steel was continued by Lieutenant Commander Donald Rowe and Captain Douglas Hamilton who examined the further effects of heat treatment on this material's ballistic performance. They determined that austenitizing, quenching and tempering this steel, a treatment which increased tensile strength and reduced ductility, significantly reduced its ballistic performance. Microstructural examination determined that there was considerable grain growth during austenitizing and that the subsequent quench produced a relatively coarse martensite. This martensitic structure was less resistant to penetration by relatively soft fragment simulating projectiles than the rolled structure of the same steel [2].

The scope of the research effort was broadened by Lieutenant Ronald Martin and Lieutenant James Phillips who commenced studies





on a 1.67% carbon steel while continuing the study of 52100 steel. Special attention was given to the metallographic characterization of these steels after they were penetrated by 0.22 caliber, 17-grain fragment simulating projectiles. Both materials were subjected to various rolling conditions and the 52100 steel was given several subsequent annealing treatments to determine the effects of these processes on resistance to penetration. It was determined that "warm-worked UHC steels have a lesser tendency to form adiabatic shear bands as compared to several conventional steel armors." These adiabatic shear bands are associated with reduced ballistic penetration resistance. Warm-worked 52100 steel's ballistic performance was found superior to conventional armors [4].

Ballistic research has continued with the work of Lieutenant Commander Randy Hillier who has further expanded the program to include various new UHC steel alloys. The effects of chromium and nickel alloying additions on ballistic performance were examined. A 1.5% plain carbon steel was also tested. None of these materials, however, has yet demonstrated ballistic performance as good as the "baseline" 52100 steel [3].

Fracture toughness studies on several high carbon and UHC steels was conducted by Lieutenant Commander James Taylor. It was determined that a commercial alloy, AISI 52100 steel, processed similarly to the other experimental alloys, did not have coarse carbides present to as great an extent, and was significantly tougher, as manifested by a strength ratio twice that of the other alloys" [5].



In summary, the commercial alloy, AISI 52100, when processed via the Sherby method, has been shown to possess excellent ballistic and fracture resistance characteristics in the warm-rolled condition. The behavior of this material in a heat-treated condition is still the subject of study and determining the fatigue behavior of this steel in a heat-treated condition is a portion of this study.

#### D. FATIGUE FAILURE OF METALS

Fatigue is a progressive localized permanent structural change that occurs in a material subjected to repeated or fluctuating strains at stresses having a maximum value less than the tensile strength of the material. Fatigue may culminate in cracking or fracture after a sufficient number of fluctuations.

The three necessary factors leading to fatigue failure are: (1) a maximum tensile stress of sufficiently high value, (2) a large enough variation or fluctuation in the applied stress, and (3) a sufficiently large number of cycles of the applied stress. In addition, there are a host of other variables, such as stress concentration, corrosion, temperature, overload, metallurgical structure, residual stresses, and combined stresses which alter the conditions for fatigue.

Traditionally, fatigue life has been expressed as the total number of stress cycles required for a fatigue crack to be initiated and then to grow large enough to produce catastrophic failure. Fatigue data also can be expressed in terms of crack-growth rate. In this study, fatigue data are expressed in terms of total life.



Most laboratory fatigue testing is done either with uniform axial loading or in uniform bending, thus producing only tensile and compressive stresses. This fluctuating stress cycle can be considered to be made up of two components: a mean, or steady, stress  $\sigma_m$ , and an alternating, or variable, stress  $\sigma_a$ . The stress is usually cycled either between a maximum and a minimum tensile stress or between a maximum tensile stress and a maximum compressive stress. The range of stress,  $\sigma_r$ , is the algebraic difference between the maximum and minimum stress in a cycle:

$$\sigma_r = \sigma_{\max} - \sigma_{\min} \quad (1)$$

The alternating stress, then, is one-half the range of stress:

$$\sigma_a = \sigma_r / 2 \quad (2)$$

The mean stress is the algebraic mean of the maximum and minimum stress in the cycle,

$$\sigma_m = (\sigma_{\min} + \sigma_{\max}) / 2 \quad (3)$$

Two ratios are used in presenting fatigue data [9]:

$$R = \sigma_{\max} / \sigma_{\min} \quad (4)$$

$$A = \sigma_a / \sigma_m \quad (5)$$

The result of fatigue tests are usually plotted as maximum stress or stress amplitude to number of cycles,  $N$ , to fracture using a logarithmic scale for the number of cycles. Stress is plotted on either a linear or a logarithmic scale. The resulting



plot of the data points is called an S-N curve. The horizontal portion of an S-N curve represents the maximum stress that the metal can withstand for an infinitely large number of cycles with 50% probability of failure and is called the fatigue endurance limit,  $S_f$ . The stress to which the metal can be subjected for a specified number of cycles is the fatigue strength.

In determining the fatigue limit of a material, it should be recognized that each specimen has its own fatigue limit, a stress above which it will fail but below which it will not fail, and that this critical stress varies from specimen to specimen for often obscure reasons. It is known that inclusions in steel have an important effect on the fatigue limit and its variability, but even vacuum-melted steel (essentially inclusion-free) shows scatter in fatigue limit. The statistical problem of accurately determining the fatigue limit is complicated by the fact that we cannot measure the individual value of the fatigue limit for any given specimen. We can only test a specimen at a particular stress, and if the specimen fails, then the stress would be somewhere above the fatigue limit of the specimen. Since the specimen cannot be retested, even if it did not fail at the test stress, we have to estimate the statistics of the fatigue limit by testing groups of specimens at several stresses to see how many fail at each stress.

The fracture surface that results from fatigue failure has a characteristic appearance, and can be divided into three zones or progressive stages of fracture.

Stage I is the initiation of cracks and their propagation by slip-plane fracture, extending inward from the surface at







approximately  $45^{\circ}$  to the stress axis. A Stage I fracture never extends over more than about two to five grains from the origin.

The transition from Stage I to Stage II fatigue fracture is the change of orientation of the main fracture plane in each grain from one or two shear planes to many parallel plateaus separated by longitudinal ridges. The plateaus are usually normal to the direction of maximum tensile stress.

Stage III occurs during the last stress cycle when the cross section is no longer able to sustain the applied load. The final fracture is the result of a single overload and can be brittle, ductile or a combination of the two [8].



## II. EXPERIMENTAL PROCEDURE

### A. MATERIAL PREPARATION

J. T. Ransom [9] proposed that practically all the fatigue failures in specimens transverse to the primary working direction start at nonmetallic inclusions. The low transverse fatigue limit in steels containing inclusions is generally attributed to stress concentrations at the inclusions, which can be quite high when an elongated inclusion stringer is oriented transverse to the principal tensile stress [9, 10]. The AISI 52100<sup>1</sup> steel used in this study was vacuum-induction melted and vacuum-arc remelted material. This double melting procedure almost completely eliminates nonmetallic inclusions, and this by itself would be expected to provide improved fatigue resistance. There still remain, however, the carbide particles normally present in such a steel, and their size and distribution will also influence the fatigue behavior of the steel. The material used in this study was supplied as a 7.93 cm (3.125 inch) hot-rolled bar in the spheroidize-annealed condition.

### B. FACILITIES USED

#### 1. General

The facilities of the Material Science Group in the Mechanical Engineering Department at the Naval Postgraduate School were adequate to conduct this research except for limited rolling mill capacity and for some specimen preparation

---

<sup>1</sup>Nominal composition of AISI 52100 steel (wt %): C, 1.0; Si, 0.19; Cr, 1.35; Mn, 0.32; Fe Balance.



requirements. Material was rolled, machined into specimens, heat treated, examined microstructurally and mechanically tested. Tensile, fatigue and hardness properties were determined. Both optical and scanning electron microscopy (SEM) techniques were used to examine fatigue fracture surfaces and general metallurgical structures.

## 2. Rolling

AISI 52100 steel used in the fatigue tests conducted in this thesis was rolled at NPS using a Fenn laboratory rolling mill of 5 hp capacity with 10.5 cm (4.13 inch) diameter rolls. This Model 172 rolling mill is a two-high, variable-speed rolling mill with maximum roll separation of 32 mm (1.25 inches) and with 152 mm (6 inches) width rolls. Specimens were equilibrated at their respective temperatures for one hour in a Blue M box-type furnace before rolling. The furnace temperature was closely monitored using a thermocouple placed directly at the specimen location, and the temperature displayed was by a digital thermometer, ensuring temperature stability to  $\pm 5^{\circ}\text{C}$ .

The specimens were taken directly from the furnace to the rolling mill and reduced approximately 1.0 mm (0.04 inch) on each pass (5-10% reduction per pass). A pass consisted of rolling the specimen twice at each roller setting. After each pass, the specimen was returned to the furnace for approximately ten minutes to allow the specimen to return to the rolling temperature. The rolling mill capacity (separating force and power) was not sufficient to allow the variation in roll speed and reduction per pass. The variation of reduction rate and speed are one factor controlling the range of microstructures of these materials.



### 3. Tensile and Hardness Testing

Sheet-type tensile test specimens were machined before heat treatment from 52100 steel; isothermally warm-rolled at 650°C. Specimens were cut such that the longitudinal axis was parallel to rolling direction. Tensile tests were conducted on an Instron Model TT-D Universal Testing Instrument utilizing wedge action grips to minimize nonaxial loading of the specimen. Load-versus-elongation curves were autographically recorded while the specimens were loaded to failure at an extension rate of 5.1 mm (0.2 inch) per minute. The data obtained from these tests were subsequently converted to engineering stresses versus engineering plastic strains to determine the yield stress and ultimate tensile strength.

Hardness testing was conducted on the machined surface of the fatigue specimens using a Wilson Model 1 JR Rockwell Hardness Tester. Hardness results were determined by disregarding the two highest and two lowest values and averaging a minimum of six subsequent test values.

### 4. Heat Treating

A box-type Blue M furnace with solid state proportioning control system and Lindberg Hevi-Duty furnaces with Honeywell Pyr-o-Volt controllers were used for heat treating. Except for the lack of protective atmosphere capabilities, these furnaces were entirely adequate. They maintained temperatures to  $\pm 5^{\circ}\text{C}$ . Each furnace was calibrated prior to heat treating using a





Newport electronic digital thermometer placed directly at the specimen location on the hearth. Oil strategically located oil containers provided adequate quenching facilities. A Lindberg type CR-5 salt bath furnace, using A. F. Holden Co. "Temper 2"® salt, was used for isothermal heat treatment.

## 5. Fatigue Testing

Fatigue tests were conducted on an Tatnall-Krouse Automation Model VSP-150 Variable Speed Plate Fatigue Testing Machine at room temperature. This fatigue machine was designed primarily for the testing of plate material under all ranges of stresses. The machine is of the fixed deflection type and uses the specimen as its own dynamometer. The loading force of the machine is transmitted by the motor through a variable speed pulley and belt to the main shaft. The variable-throw crank at the end of the main drive shaft adjusts the amount of deflection and transmits the force through a rigid connecting rod to the specimen. The machine speed was chosen as 1800 cycles per minute for these fatigue tests. The stress ratio,  $R$ , was  $-1$  and the mean stress,  $S_m$ , was zero.

The load which is to be applied at the connecting pin to produce the desired bending stresses is calculated by a flexure formula as follows. For a rectangular cross section,

$$P = \frac{sbd^2}{6L} \quad (6)$$

where  $P$  is the load at the connecting pin in lbs (to be less than 150 lbs),  $s$  is the bending stress in lbs per square inch,  $L$  the distance in inches between the connecting pin and point of stress,  $s$  ( $L = 3.75$  inch),  $b$  is the width of specimen at a



distance  $L$  from point of load application ( $b = 0.835$  inch) and  $d$  is the thickness of specimen (in inches). The maximum stress used in this study was 100 KSI. The loads used ranged from 15 lbs. to 50 lbs. Fatigue tests at low stresses were carried out to  $10^7$  cycles and the S-N curve was determined with from 8 to 12 specimens [11]. Figure 1 shows the Tatnall-Krouse VSP-150 Variable Speed Plate Fatigue Testing Machine.

## 6. Microstructural and Fractographic Analysis

The Cambridge Stereoscan S4-10 Scanning Electron Microscope (SEM), the Bausch and Lomb Balplan BS 57N1H Research Conference Microscope, the Bausch and Lomb Dynazoom Bench Metallograph and associated grinding and polishing facilities were used for photomicroscopy during this study. Microstructure specimens were examined at 100X, 200X and 400X on the Bausch and Lomb Balplan microscope and photographs taken of etched surfaces.

The fractured surfaces of fatigue tested specimens were examined at 10X and 20X on the Bausch and Lomb Dynazoom Bench macroscope and fractographs were taken of the fractured surfaces. Also, the fracture surfaces were examined at 1000X, 2000X and 5000X on the SEM for a more complete fractographic analysis.

## C. THERMAL-MECHANICAL PROCESSING

### 1. Specimen Groups AR (As Rolled)

Specimen Groups designated AR, represent several isothermally warm-rolled materials. Because they were made in the earlier stage of this research, the heat treatment process was slightly





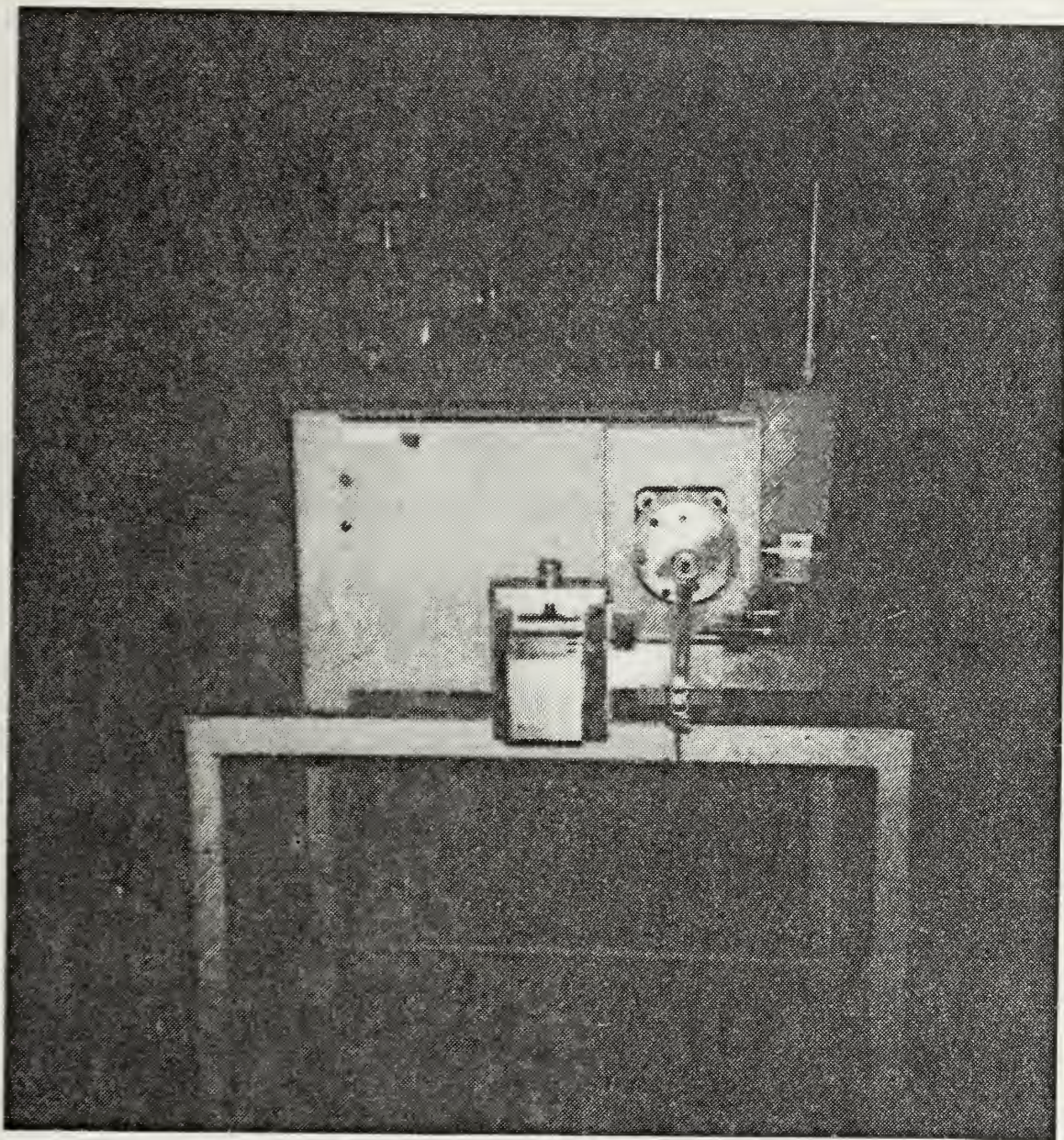


Figure 1. Tatnall-Krouse Automation Model VSP-150 Variable Speed Plate Fatigue Testing Machine.





different in each specific case. These differences are considered minor and the group can be considered as having the same processing. This group AR was divided into the following.

a. Group AR-1

An 8 cm diameter by 30 cm length bar was austenitized at 1000°C for 3.5 hours. It was then forged at 1000°C to the dimensions 5 cm x 7.6 cm x length, and air cooled to 400°C. It was reheated to 650°C and isothermally rolled to a true strain  $\epsilon = -2.0$ , rolling with 0.6 cm (0.25 inch) reduction per pass to a thickness of 0.6 cm (0.25 inch), and then air cooled. The hardness of this material was HRC 33.

b. Group AR-2

The material of group AR-1, 0.6 cm (0.25 inch) thick, 2.54 cm (1 inch) wide, was isothermally rolled further to a total true strain  $\epsilon = -2.8$  at 650°C. The resulting hardness was HRC 34.

c. Group AR-3

In an effort to produce the desired starting structure for the isothermal rolling without the necessity of the high temperature forging process, blocks of AISI 52100 steel, 3.2 cm x 3.2 cm x 7.6 cm (1.25 inch x 1.25 inch x 3 inch), were austenitized at 1050°C for 1.5 hour and interrupted-quenched in room temperature oil. This resulted in a very fine structure, ideally suited for isothermal processing. The blocks were then reheated to 650°C, held for one hour, isothermally deformed by rolling, and air cooled to room temperature. The total rolling true strain was  $\epsilon = -2.0$  and hardness was HRC 29. The slightly lower value of hardness, relative to groups AR-1





and AR-2 is due to the reheating to 650°C for 15 minutes after the last pass to straighten the rolled strip.

d. Group AR-4

This group was processed in the same manner as group AR-3, except for a lower austenitizing temperature, 1000°C, and total rolling true strain  $\epsilon = -2.5$ . The resulting hardness was HRC 30.

e. Group AR-5

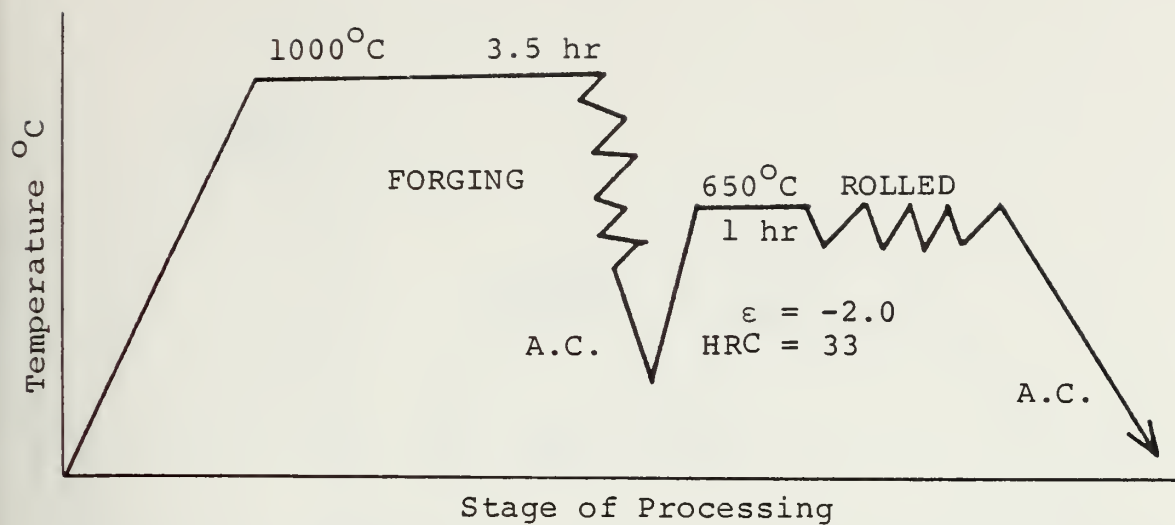
The thermal-mechanical procedures are the same as group AR-1 except a 100°C lower isothermal rolling temperature, 550°C, was used. Figure 2 is a series of schematics of these processing procedures.

2. Specimen Group QT (Quench and Temper)

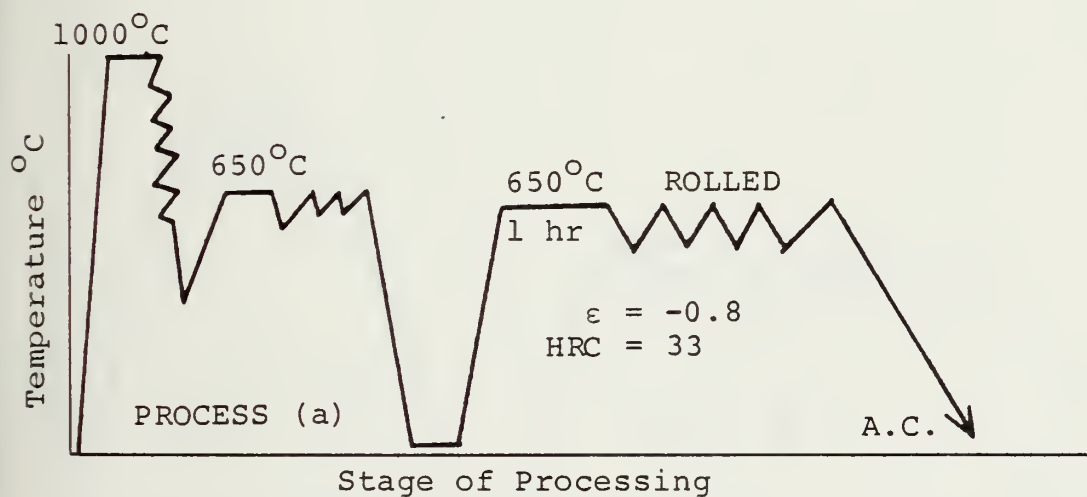
Blocks of 52100 steel, 3.2 cm x 3.2 cm x 7.6 cm (1.25 inch x 1.25 inch x 3 inch), were rolled at 900°C to a thickness of 3.8 mm (0.15 inch) to produce strips for specimen fabrication. After rolling they were homogenized at 850°C for seven hours and furnace cooled to 200°C. These strips were machined into the fatigue specimens (without grinding the surface of the specimens). The pre-machined specimens were reheated to 843°C for 15 minutes and then oil quenched, resulting in a hardness of HRC 62. The specimens were cooled to -26°C for five hours and then tempered at 172°C for ten hours. The specimens were then cooled again to -26°C for 1.5 hours, tempered at 172°C for two hours and air cooled. The resulting hardness obtained was HRC 57-58.

This heat treatment is designated the "Conventional Heat Treatment" and is the standard heat treatment recommended





(a) AR-1



(b) AR-3

Figure 2. Schematic Representation of the Thermal-Mechanical Processing of AR Specimen Group



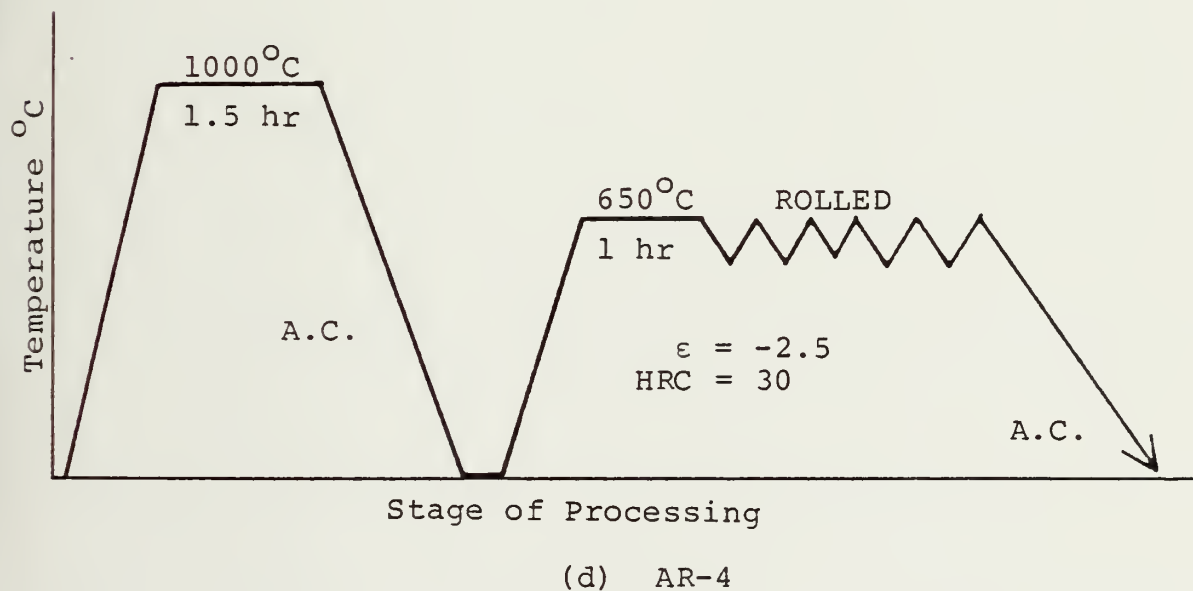
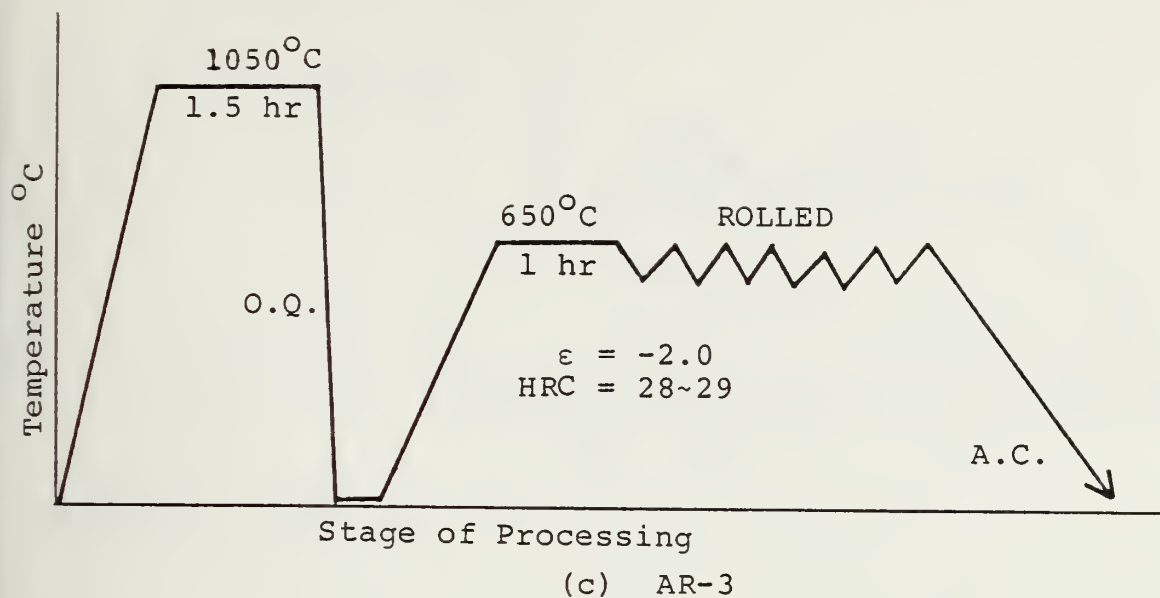


Figure 2. Continued



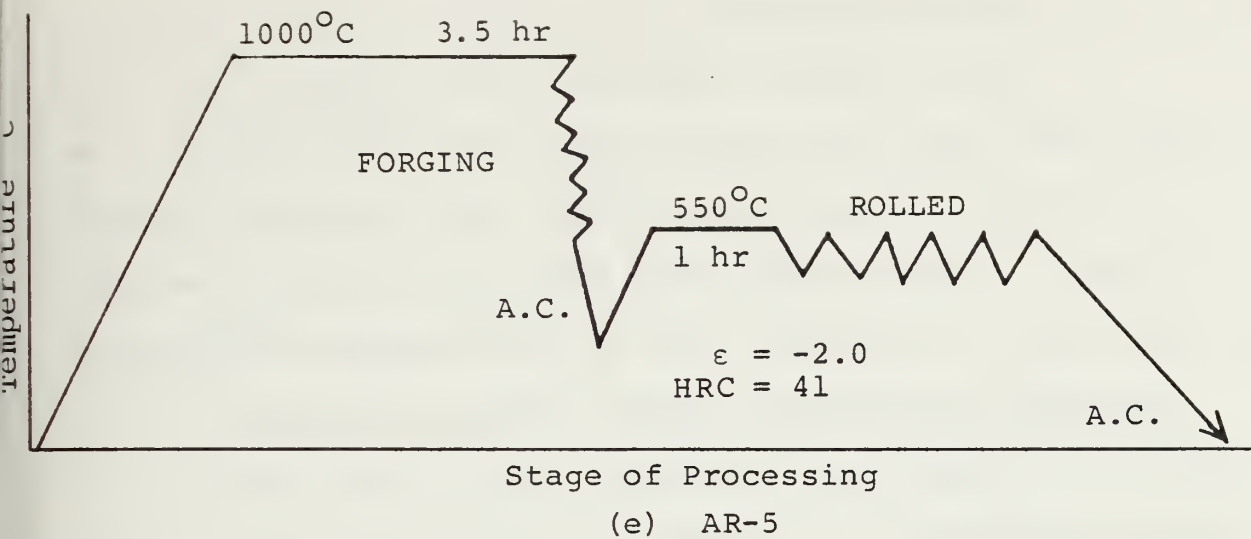


Figure 2. Continued





for 52100 steel for use as a ball bearing material. R. J. Parker, et al [12], showed that the longest fatigue lives were obtained with this heat treatment for AISI 52100 steel. Fatigue properties were better than those for AISI M-1, AISI M-2, AISI M-10 and AISI M-50 series steels. Figure 3 illustrates schematically the heat treatment of this group QT.

### 3. Specimen Group RQ (Rolled, Quenched and Tempered)

This group of heat treatments is a combination of the group AR and group QT heat treatment and processing sequences. The material was austenitized for 1.5 hour at 1050°C, air cooled to room temperature, reheated to 650°C for one hour, and then isothermally rolled to the total strain of  $\epsilon = -1.6$ . Hardness was HRC 28. Fatigue specimens were premachined and hardened; austenitizing was done at 820°C for 20 minutes, followed by oil quenching to obtain an HRC 62.5 hardness. Specimens were then tempered for 24 hours at 160°C and air cooled, giving a final hardness of HRC 60. Figure 4 illustrates the schematic heat treatment process for this group.

### 4. Specimen Group QI (Quench and Isothermally Transformed)

This process originated from R. Kar's [13] suggested heat treatment. Kar proposed that isothermal transformation subsequent to two-cycle austenitization, would give a strength-toughness combination superior to standard quenched and tempered AISI 52100 steel. In this process, 52100 steel strips, already rolled at 900°C, were fully homogenized by holding at 850°C for seven hours followed by furnace cooling. After machining, specimens were austenitized at 1050°C for 1.5 hours, oil quenched (in 100°C oil) reaustenitized at 900°C



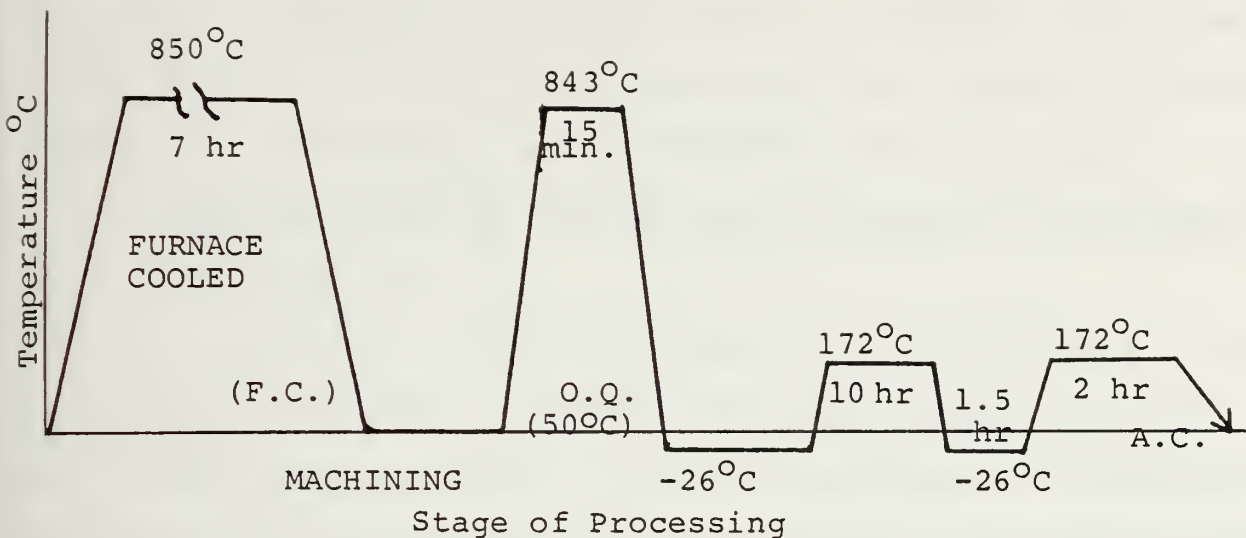


Figure 3. Standard Heat Treatment for AISI 52100 Bearing Steel Which is Oil Quenched and Double Tempered. Specimen Group QT HRC 58.

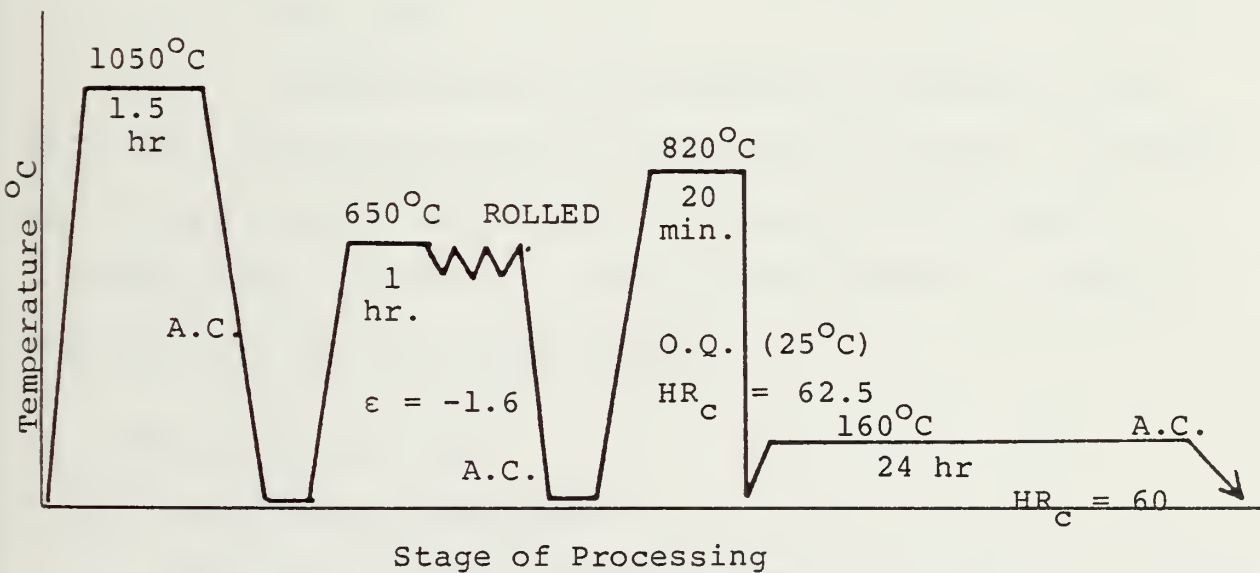


Figure 4. Warm-Rolled, Quenched and Tempered Processing. Specimen Group RQ HRC 60.



for twenty minutes, isothermally transformed at 260°C for one hour in a salt bath and then finally air cooled. A hardness of HRC 51 was obtained for the resulting fine, Bainitic structure. Figure 5 is a schematic of this treatment for this group.

5. Specimen Group RI (Rolled and Isothermally Transformed)

a. Group RI-1

Blocks of AISI 52100 steel, 3.2 cm x 3.2 cm x 7.6 cm (1.25 inch x 1.25 inch x 3 inch), were austenitized at 1050°C for 1.5 hour and air cooled. They were reheated and isothermally rolled at 650°C to a total true strain of  $\epsilon = -1.4$ , followed by air cooling. After machining, specimens were reheated to 837°C for 20 minutes, quenched in a 340°C salt bath and isothermally transformed for 1.8 hours and water quenched. They were then tempered at 285°C for 30 minutes and air cooled, obtaining a hardness of HRC 55.

b. Group RI-2

A second series of pre-machined specimens from Group RI-1 were austenitized at 815°C for 20 minutes, quenched into a salt bath at 343°C, held 1.5 hour and air cooled, obtaining HRC 44 hardness. Figure 6 and Figure 7 illustrate these heat treatments schematically.

D. SPECIMEN PREPARATION

1. Tensile Test Specimens

Sheet-type tensile test specimens, as shown in Figure 8, were machined from the as-rolled sheet of 52100 steel and subsequently heat treated to the specimen group RQ and RI-2 condition. The specimens were cut with the longitudinal direction parallel



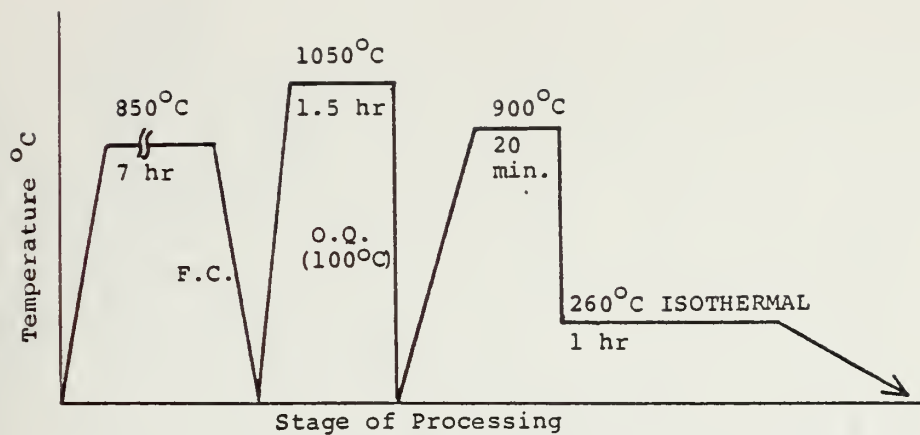


Figure 5. Double Austenitized and Isothermally Transformed Heat Treatment Process. Specimen Group QI HRC 51.

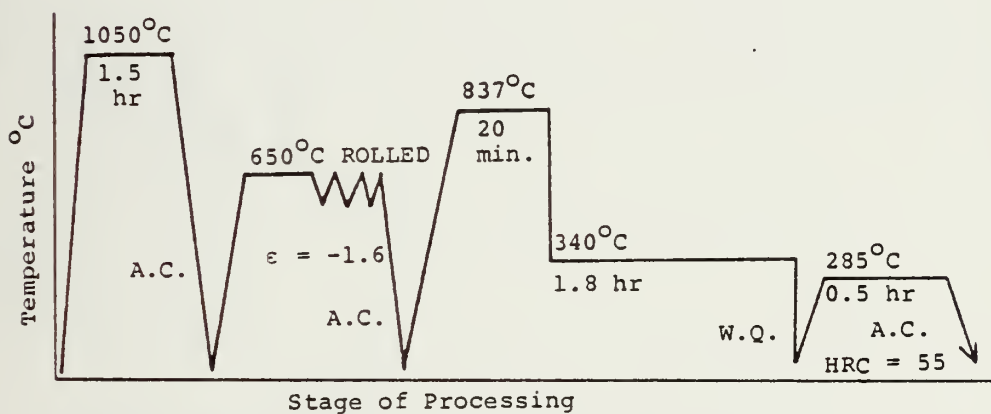


Figure 6. Isothermally Rolled and Transformed, Quenched and Tempered Heat Treatment. Specimen Group RI-1 HRC 55.

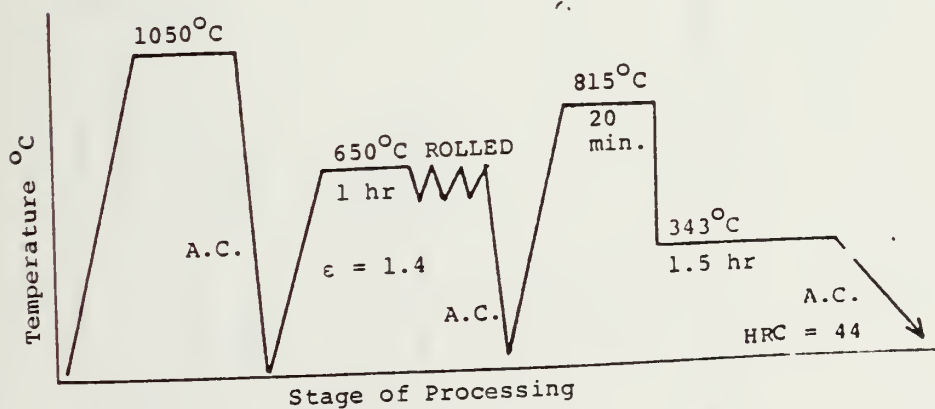
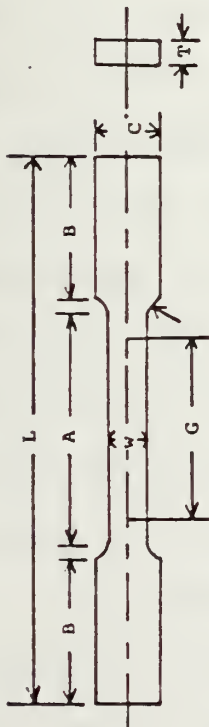


Figure 7. Isothermally Rolled and Isothermally Transformed Heat Treatment. Specimen Group RI-2 HRC 44.







$G = 1.000 \pm 0.003$  in.

$W = 0.250 \pm 0.002$  in.

T = Thickness of material

R = 0.25 in.

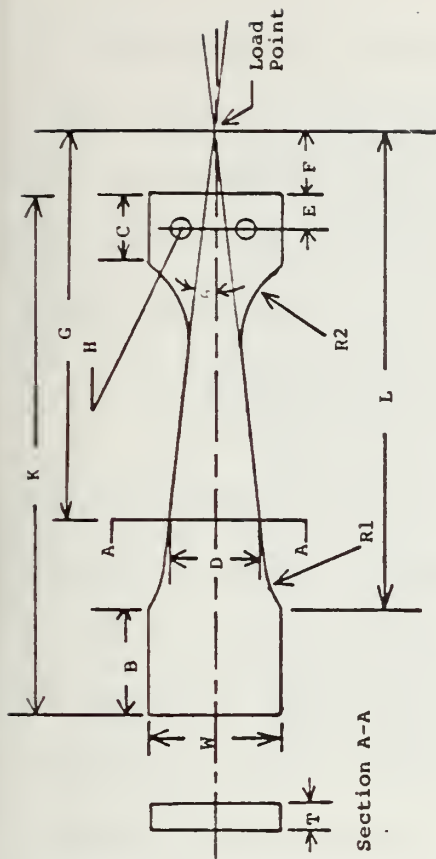
L = 4 in.

A = 1.25 in.

B = 1.25 in.

C = 3/8 in.

Figure 8. Subsize tensile test specimen specifications.



B = 0.750 in.

C = 0.500 in.

D = 0.666 in.

E = 0.250 in.

F = 0.500 in.

G = 3.000 in.

H = 0.1890 in. dia.

K = 4.0 in.

L = 3.75 in.

W = 1.000 in.

T = thickness of material

R1 = 1.00 in.

R2 = 0.75 in.

$\theta = 6^\circ 21'$

Figure 9. Fatigue test specimen specifications.



to the rolling direction; the gage length for all tensile test specimens was one inch. After heat treatment, the surfaces of the specimen were ground to a depth of 0.010 inch per side to remove the decarburized layer; the sides of these specimens were not ground.

## 2. Fatigue Test Specimen

To avoid the difficulties of machining hardened material into specimens after heat treatment, every specimen was machined before final heat treatment. Decarburized surfaces were ground but the side surfaces of the specimens were not ground as loss of critical dimensions would occur. Decarburization of the surface of heat-treated steel is particularly detrimental to fatigue performance [11]. The decarburized side surface, however, might affect fatigue performance and this will be considered later.

The surfaces of the heat treated specimens were ground with a fine stone wheel. The surface roughness was specified by the surface roughness symbol of General Electric Company,  $R_{3\frac{1}{2}}$ , which means that the average peak-to-valley roughness was 118 micro inches. The direction of grinding was always longitudinal to the length of the specimen and rolling direction. The sharp edges of the specimens were also ground with a sandpaper wheel. Figure 9 illustrates the fatigue test specimens. Figure 10 shows the roughness of specimen in a macrograph.

For identification, each specimen was assigned a designator consisting of two letters and two digits. The letters and first digit indicate the specimen group (depending upon thermomechanical





Figure 10. Macrograph shows the surface roughness of a fatigue test specimen. The specimen surface was illuminated at 45 degrees. The average depth from peak to valley is 118 micro inches x70.



processing) and the last digit indicates the specimen tested in each specimen group. For example, AR-5-3 indicated specimen group AR-5 and -3 indicates the third specimen tested.

### 3. Metallographic and Fractographic Test Specimens

Samples were sectioned from specimens tested of each specimen group. The sectioned surface of the specimen was sanded flat and metallographically prepared using alumina micropolish for final polishing. Specimens were ultrasonically cleaned and the polished surface etched in a mixed solution of 2% nital and 2% picral. Immersion times varied from ten seconds to one minute. Often repolishing and reetching improved the quality of the etched surface.







### III. RESULTS

#### A. MECHANICAL TESTING RESULTS

Fatigue, tensile and hardness test results will be described in this section in order to characterize the effects of variation in thermomechanical processing and subsequent conventional heat treatment on microstructure and mechanical properties. The tests were conducted under conditions outlined in the Experimental Procedure section.

##### 1. Hardness Testing Results

Hardness testing was conducted on the grip surface of the fatigue specimens. Ten hardness readings were taken, the lowest two and the highest two readings were excluded, and the remaining six hardness readings were averaged. Table I provides a summary of the hardness testing results.

##### 2. Tensile Testing Results

A limited amount of tensile testing of the 52100 steels was conducted (Table I). Only specimen groups RI-2 and RQ were examined by tensile testing; data for other specimen groups was inferred from the data of other Naval Postgraduate School studies and from the general literature. Two specimens of group RI-2 were tested in tension with almost identical results. The data given are the average of both tests. Two specimens were prepared



from group RQ, but only one specimen was tested. Because of the high hardness it was too difficult to properly hold the specimens in the wedge-action grips of the tensile test machine and problems were also encountered in assuring proper alignment, critical in testing such a hard, low ductility material.

a. Specimen Group RI-2

These specimens had a yield strength of 231 KSI; an ultimate tensile strength of 258 KSI; an elongation to fracture of 9.4% and a reduction in area of 26.5%. The hardness was HRC 50. The tensile fracture surface of these specimens showed quite ductile fracture modes (Figures 11-15) and high values of elongation and reduction in area, notwithstanding the high yield and ultimate tensile strength.

b. Specimen Group RQ

This specimen had yield and ultimate tensile strengths of 227.5 KSI with less than 1% elongation. The tensile fracture surface revealed a quenching crack and a brittle fracture mode.

3. Fatigue Testing Results

a. Specimen Groups AR-1 and AR-5

The specimen groups AR-1 and AR-5 were tested to study the effects of structures produced by different rolling temperatures on fatigue resistance. Because of the limited quantity of specimens available, these materials were subjected to testing with only three specimens from each group. The AR-5 group of



TABLE I  
RESULTS OF MECHANICAL TESTING

Specimen Group	Hardness (HRC)	UTS (KSI)	0.2% Yield Stress (KSI)	Elongation (%)	Reduction of Area (%)
AR-1 (1)	36	138.8	137	16.5	
AR-5	41	NOT TESTED			
AR (425 <sup>o</sup> C Rolled) (2)	49	271.7		3.5	
QI (3)	51	331.0	246		
RQ (4)	60	227.5	227	1.0	0
RI-2	50	258.0	231	9.4	26.5

NOTE: (1) Data from Reference [5]  
 (2) Data from Reference [4]  
 (3) Data from Reference [8]  
 (4) Fractured Due to Quenching Crack





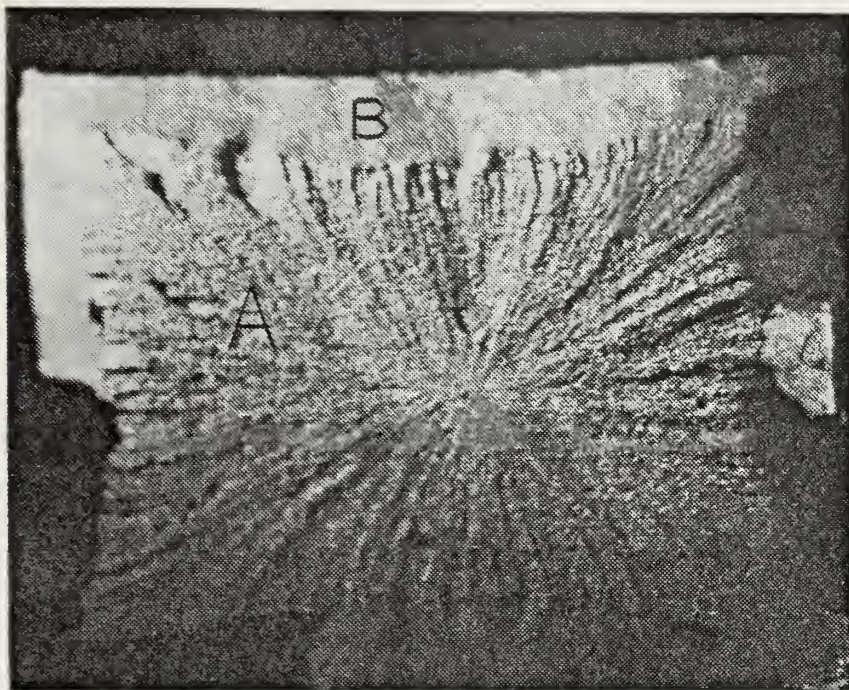


Figure 11. Macrofractograph of a tensile specimen from specimen group RI-2, showing fibrous zone (center), radial zone (A) and shear lips zone (B). Tensile strength was 258 ksi X20.

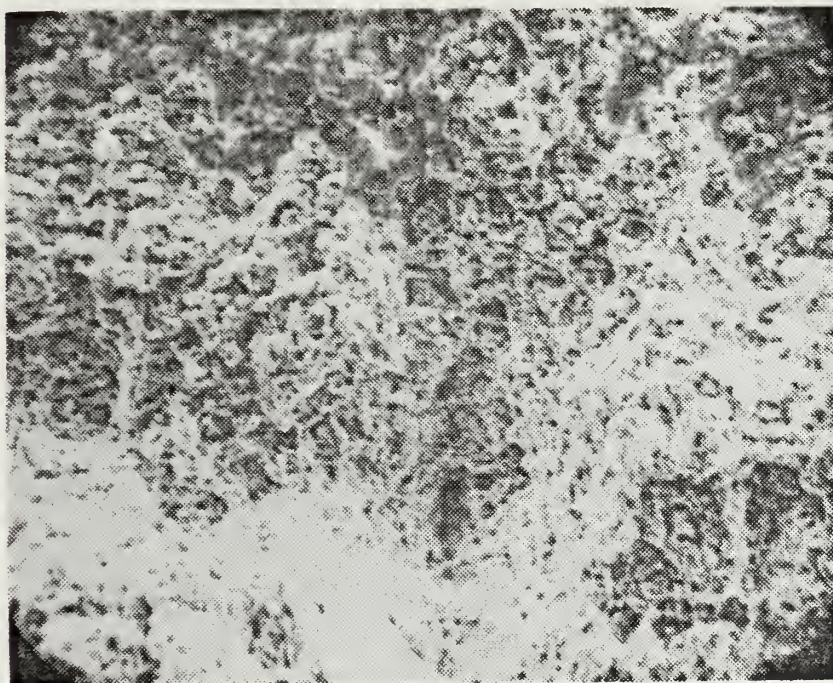


Figure 12. SEM fractograph of the fibrous zone of specimen RI-2 of Fig. 11, showing quite ductile fracture with many microvoids. X1000.





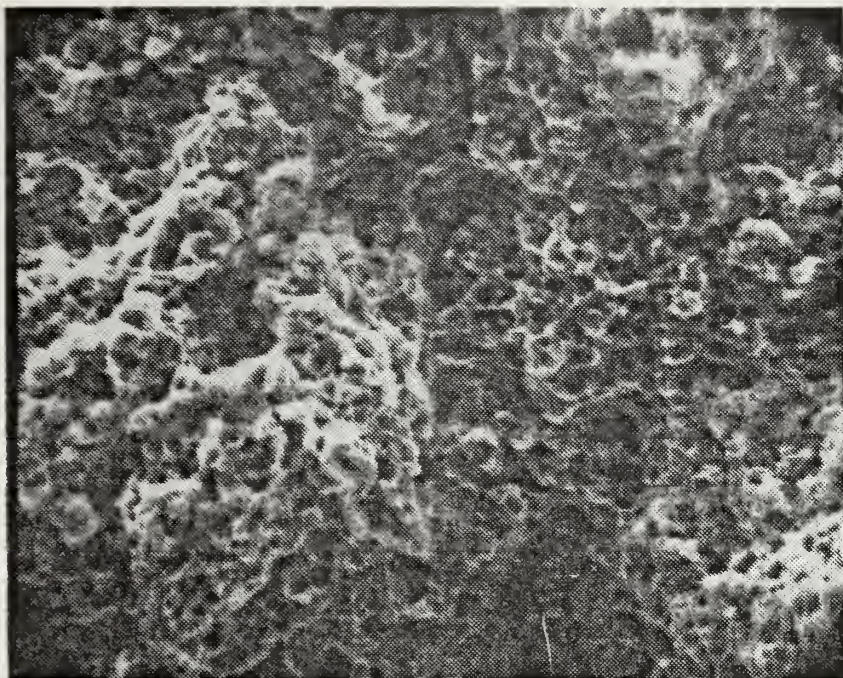


Figure 13. Higher magnification of Fig. 12 fractograph (specimen RI-2), showing an area composed of equiaxed dimples. X2000.

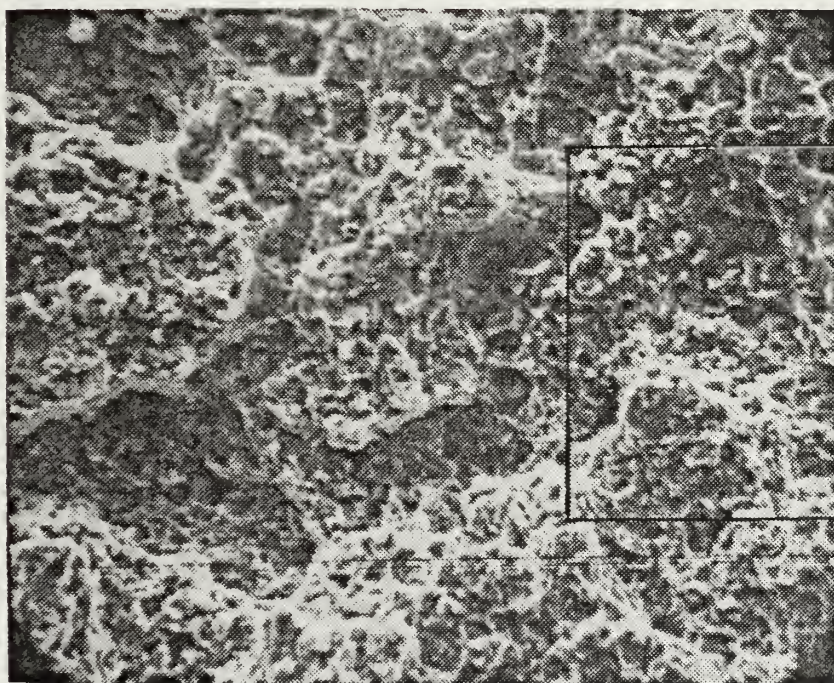


Figure 14. SEM fractograph of fibrous zone of Fig. 11 (marked A) showing various size of dimples and a tear ridge. This fractograph also shows quite ductile fracture. X1000.





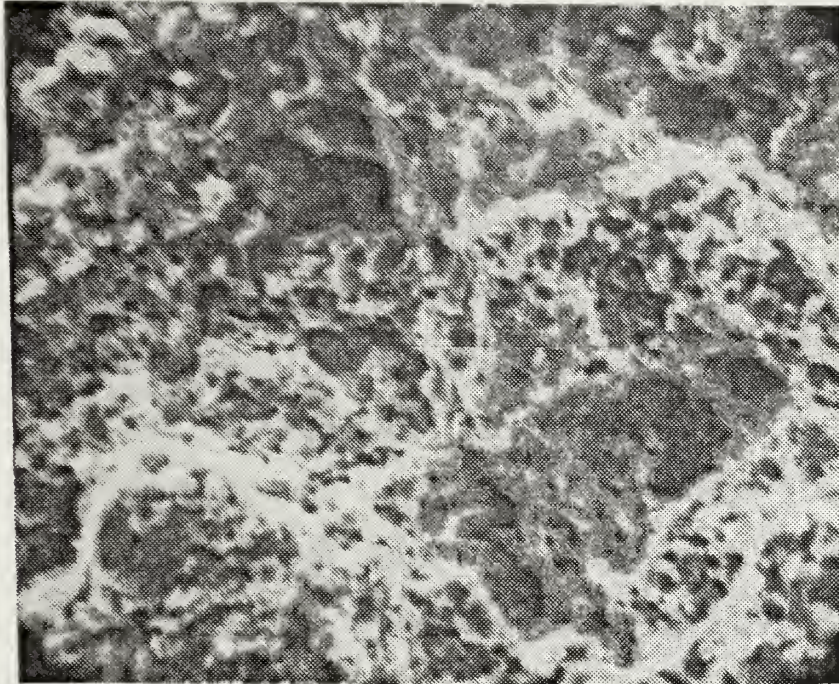


Figure 15. Area outlined by rectangle of Fig. 14 at higher magnification. Fracture occurred entirely by microvoid coalescence. X2000.



specimens, from material rolled at  $550^{\circ}\text{C}$ , showed significantly better fatigue resistance and hardness compared to those of  $650^{\circ}\text{C}$  rolled material. The difference in fatigue life,  $N$ , at 100 KSI maximum stress,  $S_{\text{max}}$ , was 70,300 cycles, and 157,100 cycles at 65 KSI. Specimen AR-1-3 was fractured after 10,024,500 cycles at 50 KSI, but Specimen AR-5-3 survived 10,393,500 cycles at the same maximum stress. Specimen AR-5-3 was retested at a higher stress, 55 KSI, and did not fail after an additional 10,662,900 cycles. Figure 16 is a plot of maximum stress versus fatigue life for the specimen groups AR-1 and AR-5. These graphs suggest that the rolling temperature has significant effect on structure and hence on fatigue performance of 52100 steel.

b. Specimen Groups AR-2, AR-3, and AR-4

Even though the material of these groups was rolled at  $650^{\circ}\text{C}$ , they represent different conditions in processing compared to Group AR-1. Specimen AR-1 was rolled at Viking Metallurgical Corporation in Albany, California, by a high capacity rolling mill, while material for Specimen Groups AR-2, AR-3 and AR-4 were rolled in the laboratory at NPS by a smaller capacity rolling mill. There are, therefore, differences in strain rate per pass, rotational speed of the rollers and actual rolling temperature due to cooling of specimens during rolling deformation. Also, AR-2, AR-3, and AR-5 materials were reheated at  $650^{\circ}\text{C}$  after the last pass for straightening. Thus, the material of these groups was actually annealed at  $650^{\circ}\text{C}$  for 15 minutes.

Specimens from this group showed lower fatigue resistance at both high stress and low stress when compared to Group AR-1. Figure 17 is a plot of stress versus fatigue life;





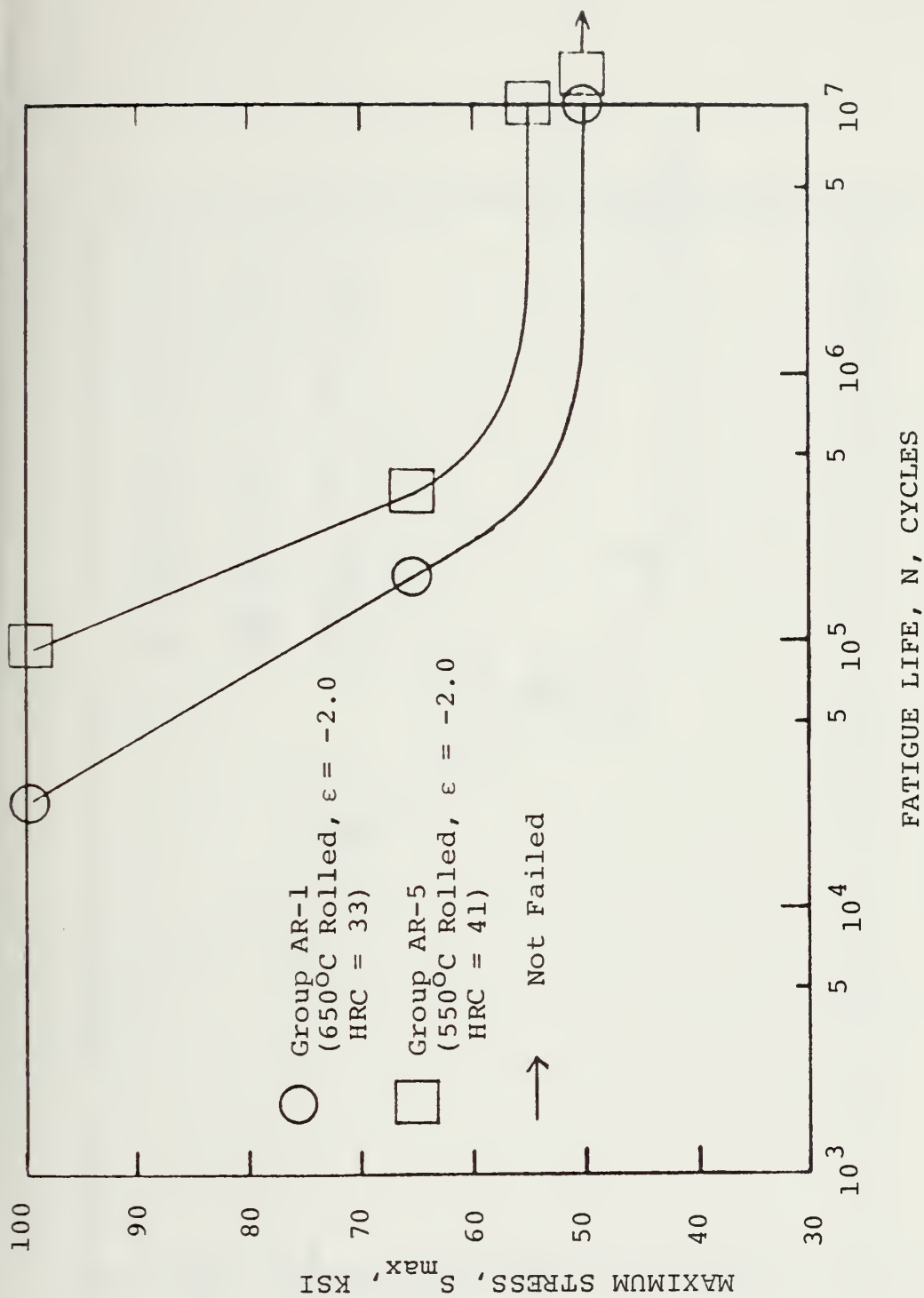


Figure 16. Plot of Maximum Stress Versus Fatigue Life of AR-1 and AR-5 Specimen Groups.



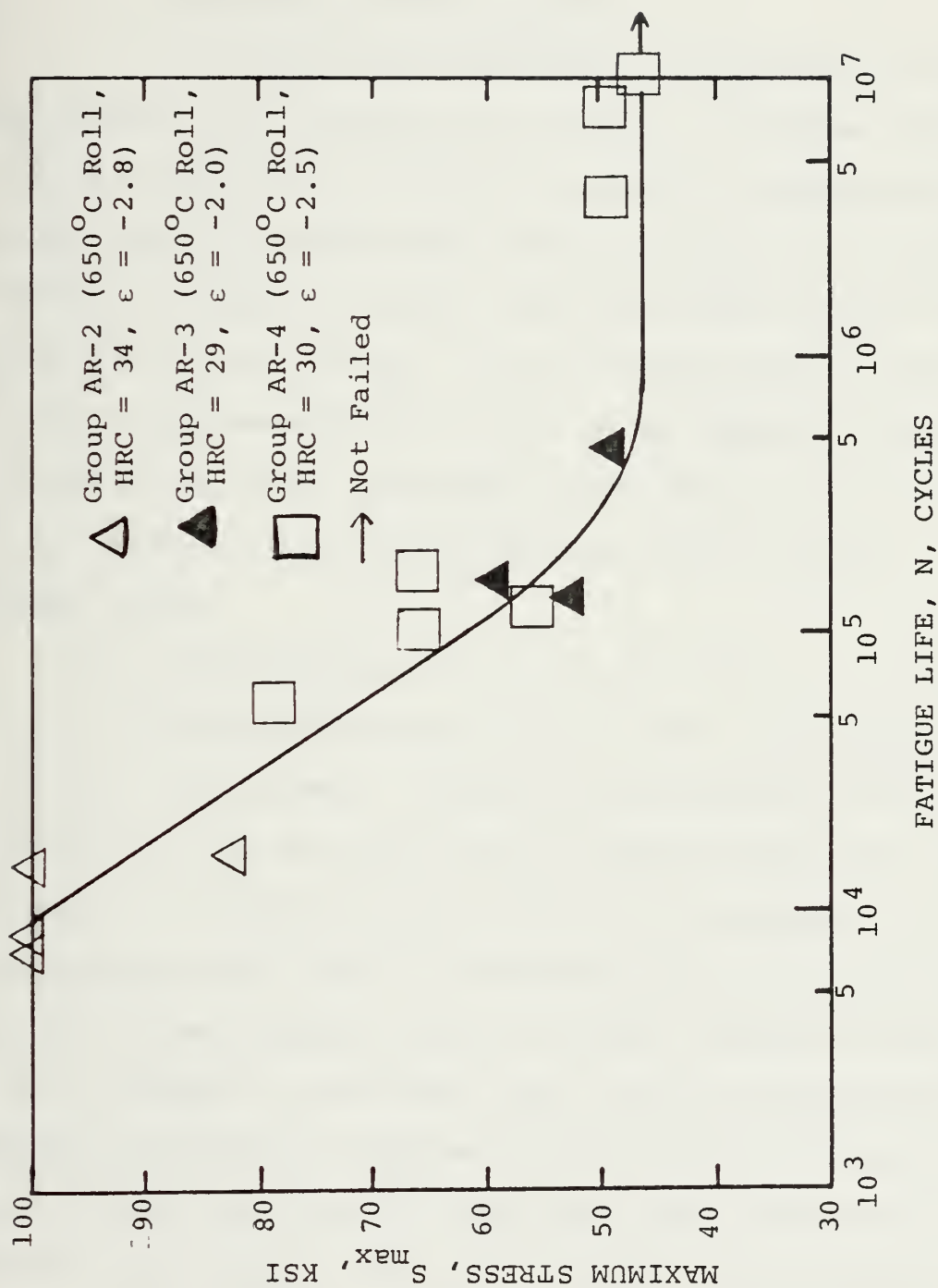


Figure 17. Plot of Maximum Stress Versus Fatigue Life of AR-2, AR-3 and AR-4 Specimen Groups.



data points from all groups are combined into one curve because of similarity of structures. These specimens showed an endurance limit of 47 KSI.

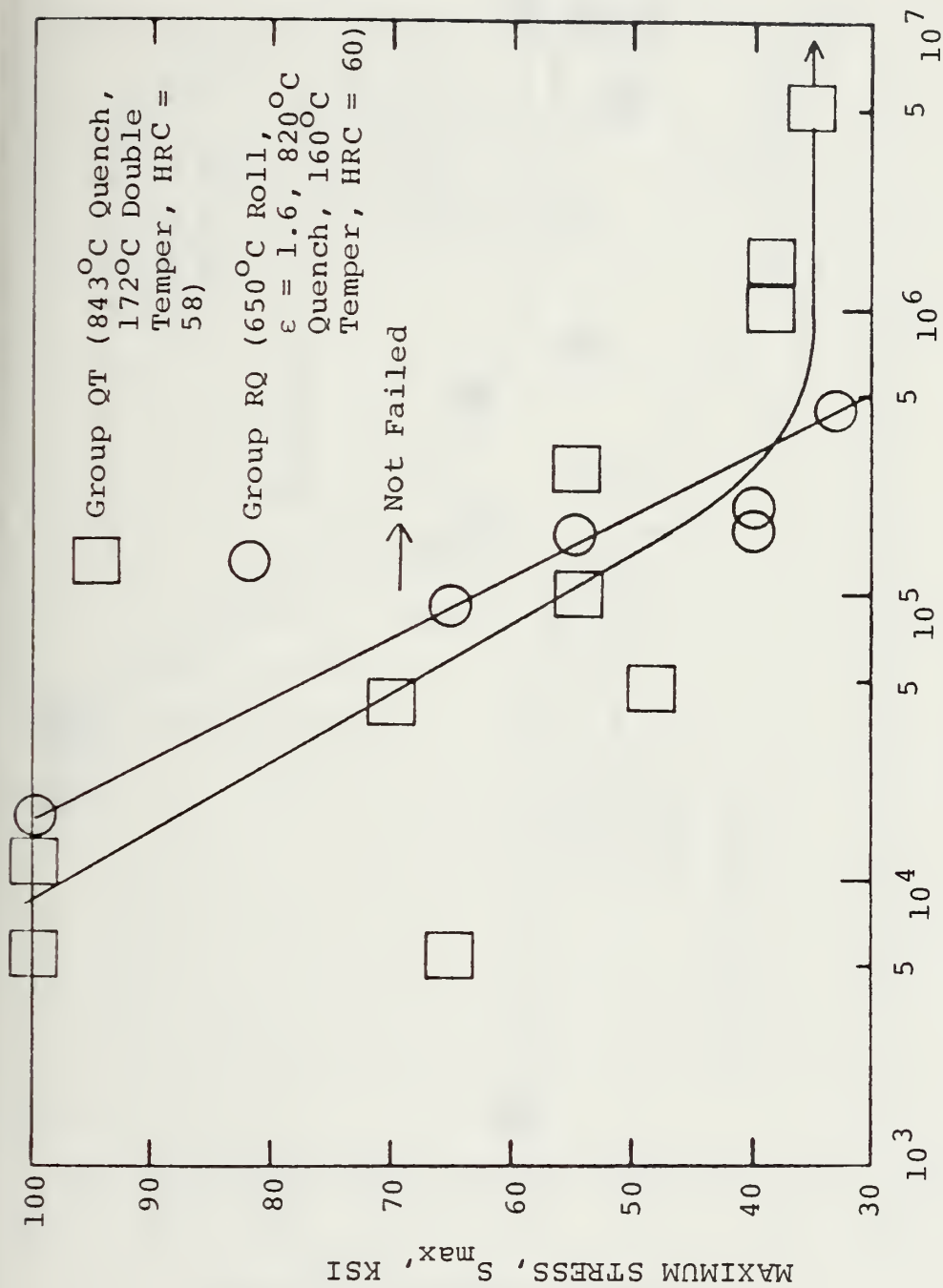
c. Specimen Groups QT and RQ

These two specimen groups are compared with each other because their hardness was similar. Specimen Groups QT and RQ had hardnesses of HRC 58 and HRC 60, respectively. Specimen Group QT showed more scatter in results. Specimen Group RQ has superior fatigue resistance both at high and intermediate stress levels, but the fatigue limit could not be found at stresses above 30 KSI, while Specimen Group QT exhibited a 35 KSI endurance limit. Figure 18 is a plot of maximum stress versus fatigue life for these specimen groups.

d. Specimen Groups QI, RI-1 and RI-2

Specimen Group QI and RI-1 have hardnesses of HRC 52 and HRC 55, respectively. Group RI-1 has superior fatigue resistance in both the high and low stress range when compared to Group QI. Group RI-1 has 38 KSI as its endurance limit while Group QI has 35 KSI. The fatigue data for Specimen Group RI-2 were compared with the similar hardness Groups QI and RI-1 because RI-1 and RI-2 have a similar thermomechanical processing treatments. Specimens from Group RI-2 show conspicuous superiority in the endurance limit compared with the specimens from Group QI and RI-1. Figure 19 is a plot of maximum stress versus fatigue life for these specimen groups.





FATIGUE LIFE, N, CYCLES

Figure 18. Plot of Maximum Stress Versus Fatigue Life of QT and RQ Specimen Groups.





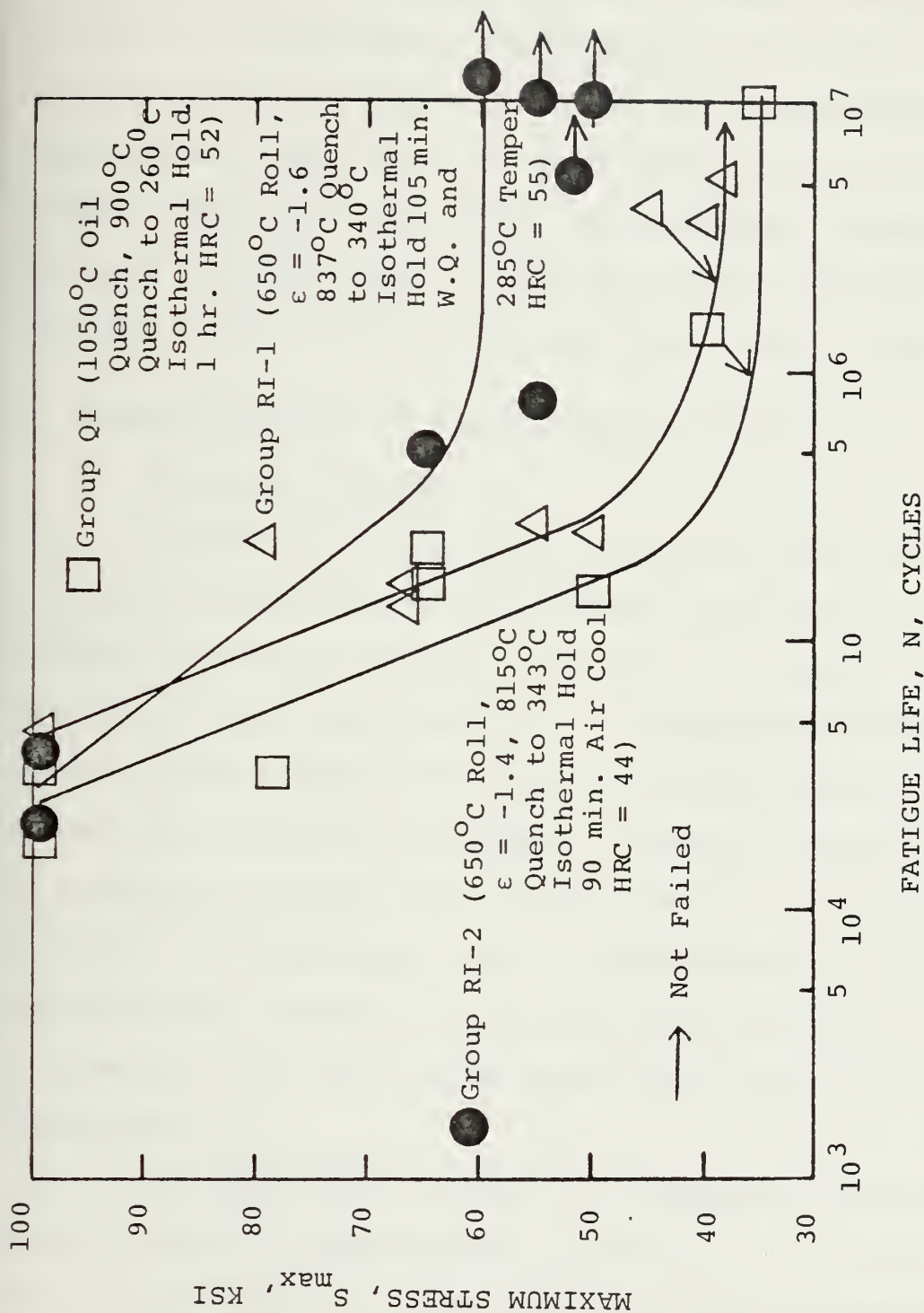


Figure 19. Plot of Maximum Stress Versus Fatigue Life of QI, RI-1 and RI-2 Specimen Groups.



e. Specimen Groups AR-5 and RI-2

Specimen Groups AR-5 and RI-2 were compared to each other in Figure 20 because they have similar hardness, HRC 51 and HRC 44, respectively. Specimen Group AR-5 has better fatigue strength in the high-stress, low-cycle fatigue region than Specimen Group RI-2, but less fatigue strength under low stress, high-cycle conditions. The endurance limits of Specimen Groups RI-2 and AR-5 were 60 KSI and 55 KSI, respectively. The results of these fatigue tests are summarized in Table II.

B. MICROSTRUCTURAL AND FRACTOGRAPHIC RESULTS

1. Specimen Group AR

Figures 21-52 are microstructures, macro-fractographs, and micro-fractographs of the Specimen Group AR-1 through AR-5. Specimen Groups AR-1 and AR-5, processed by Sherby's method, show the break-up and refinement of the massive carbides (cementite) that would otherwise form during cooling from austenite to below the eutectoid. Further, isothermal rolling at a temperature below the eutectoid refines the ferrite grain size and carbide particle size. Specimen Groups AR-2, AR-3 and AR-4 were processed after austenitizing only by rolling at a temperature below the eutectoid and then cooling to room temperature.

No significant structural differences could be detected in the optical microstructure in processing conditions. The microstructures of these specimens reveal an extremely fine banded microstructure, a result of strain-enhanced spheroidization of cementite that occurs during warm-working at 650°C.



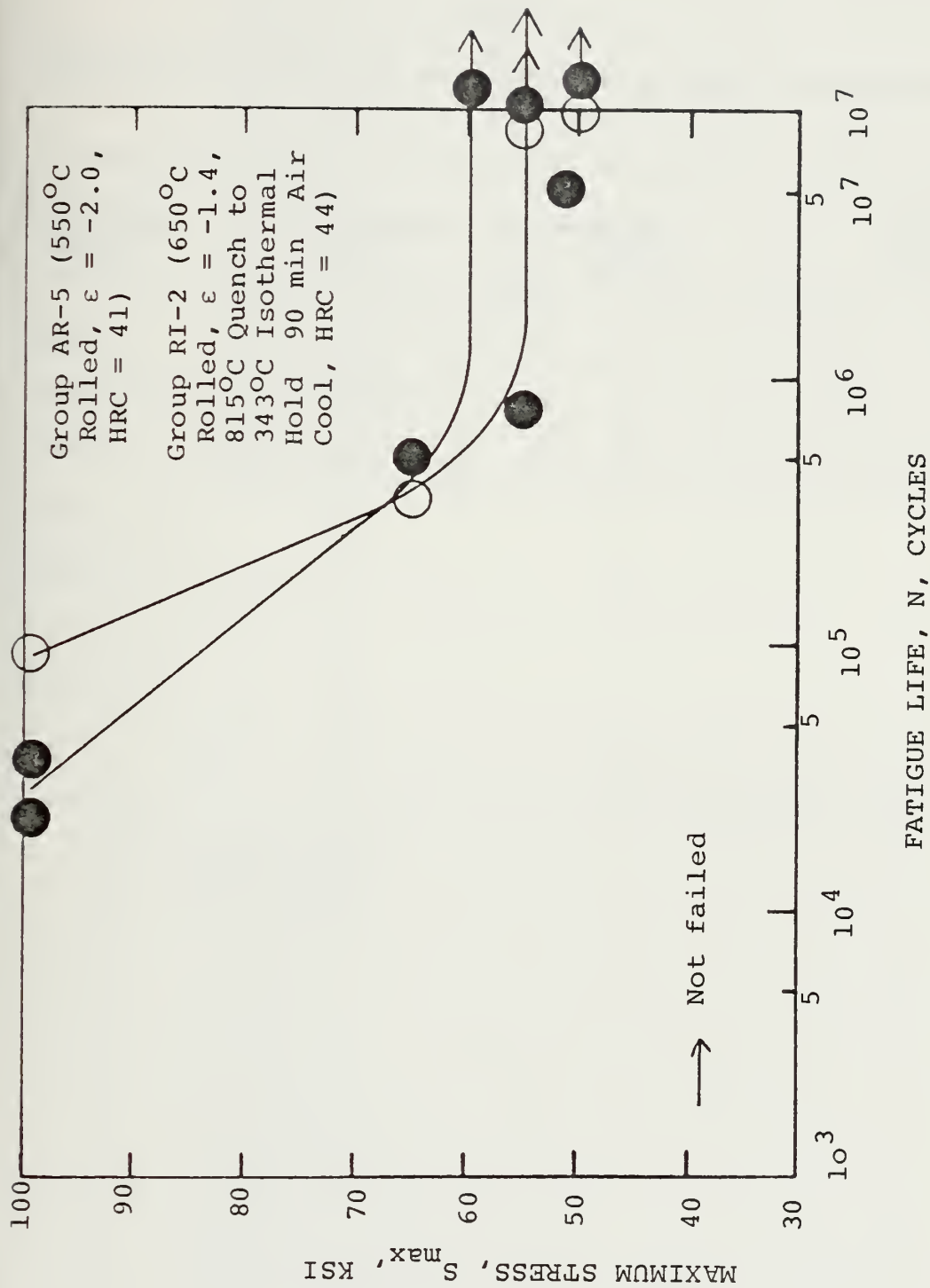


Figure 20. Plot of Maximum Stress Versus Fatigue Life of AR-5 and RI-2 Specimen Groups.



TABLE II

COMPARISON OF FATIGUE PERFORMANCE OF EACH SPECIMEN GROUP

Specimen Group	Hardness $HR_C$	Fatigue Limit	Fatigue Life $f(\sigma)$ $\sigma = 80 \text{ ksi}$
AR-1	33	3	4
AR-2,3,4	28-30	4	7
AR-5	41	2	1
QT	58	7	8
RQ	60	8	6
QI	51	6	5
RI-1	55	5	3
RI-2	44	1	2

1 = Highest Value

8 = Lowest Value





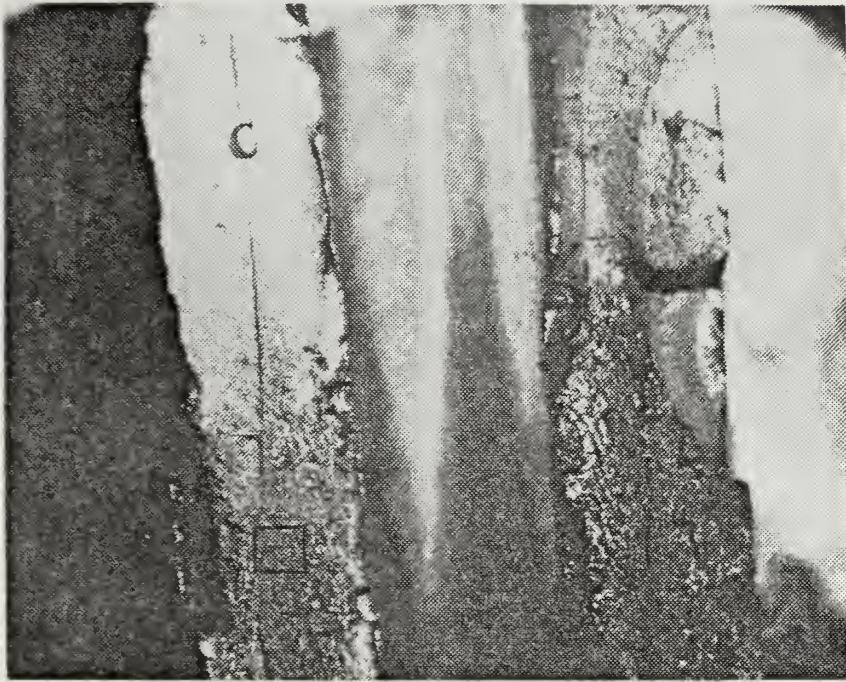


Figure 21. Macrograph of fatigue-fracture surfaces for specimen AR-2-1, fractured after 7,600 cycles at 100 ksi, showing several sites of fracture initiation. X10.



Figure 22. Area outlined by the rectangle in Fig. 21 at higher magnification in SEM, which shows secondary cracks parallel to the specimen surface and normal to the rolling direction. X100.







Figure 23. Area outlined by the rectangle in Fig. 22 at higher magnification. This fracture surface displays a progression of rather fine but extremely irregular striations, separated by secondary cracks. Cleavage facets are visible at A. X1000.



Figure 24. Another secondary crack on the fracture surface at higher magnification. This fracture surface displays fine microvoid coalescence and tear ridges, shown at D. X2000.





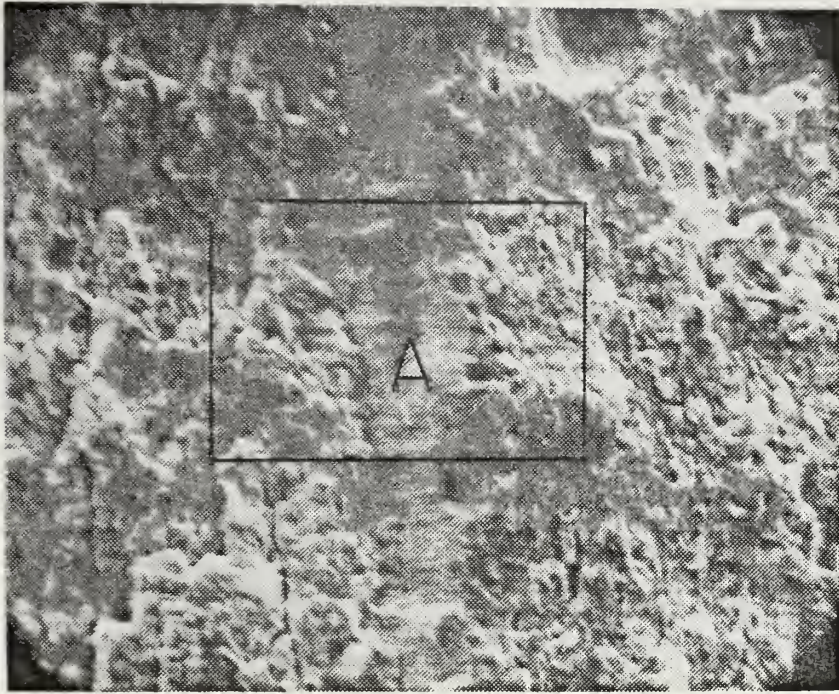


Figure 25. View at position C in Fig. 21. A is the boundary at which two cracks propagating from both the left and right side met. Fragmentary fatigue striations are visible, many of which are associated with a system of fissures. X1000.



Figure 26. Area outline by the rectangle in Fig. 25 at higher magnification showing tear ridges, cleavage facets, microvoid coalescence and secondary cracks. X2000.





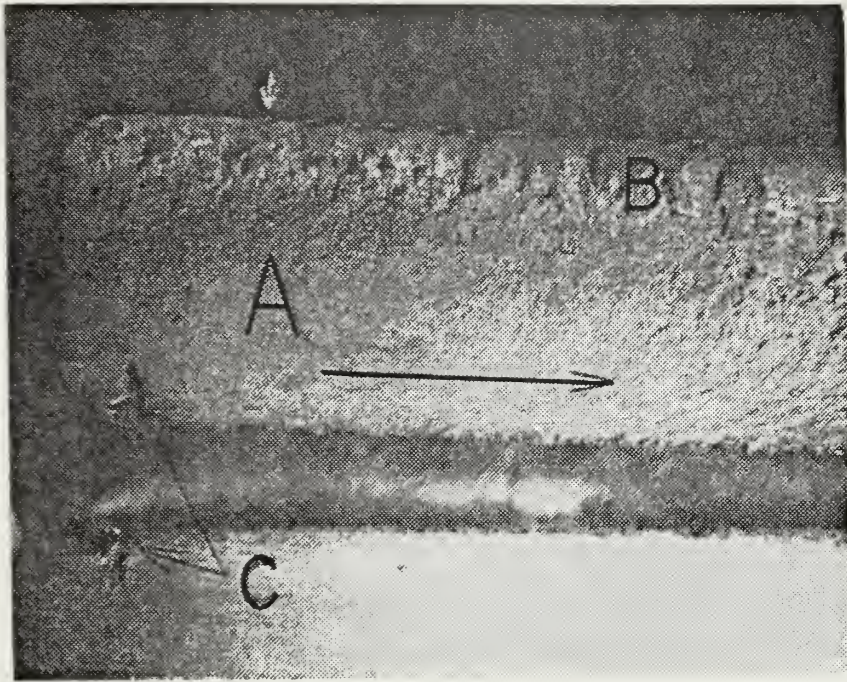


Figure 27. Macro-photograph of fatigue fracture surface of specimen AR-3-5, fractured after 200,000 cycles at 62 ksi. Area A is fatigue zone. Note the lack of beach marks, indicating that the load amplitude and environment were uniform. The region B is the region of final, fast fracture. C indicates the site of fracture initiation; also, it is evident that chevron marks indicate the crack origin. Fatigue crack propagation is fastest in the transverse direction as indicated by the arrow. Shear rupture along the periphery is indicated by arrows. X10.





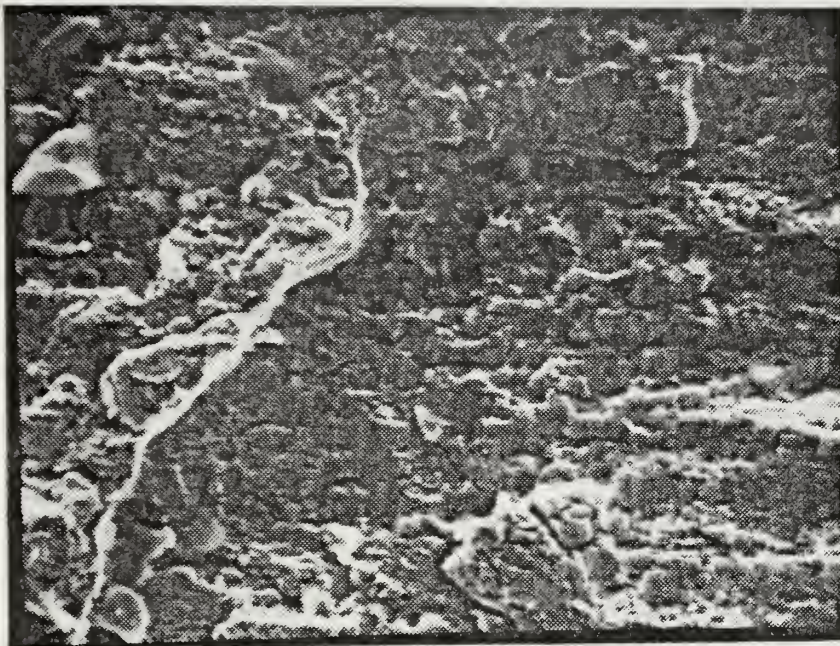


Figure 28. Higher-magnification view of region B in Fig. 27. The banded carbide structure produced many secondary cracks parallel to the surface of the specimen. Microvoid coalescence is evident. Note to cleavage facets. X1000.

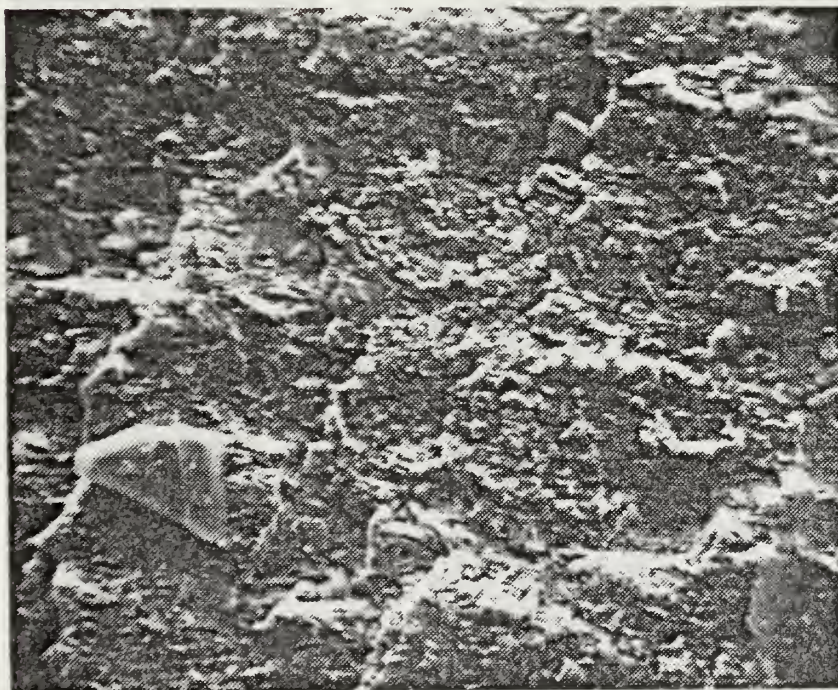


Figure 29. Higher-magnification view of region C in Fig. 27. X1000.





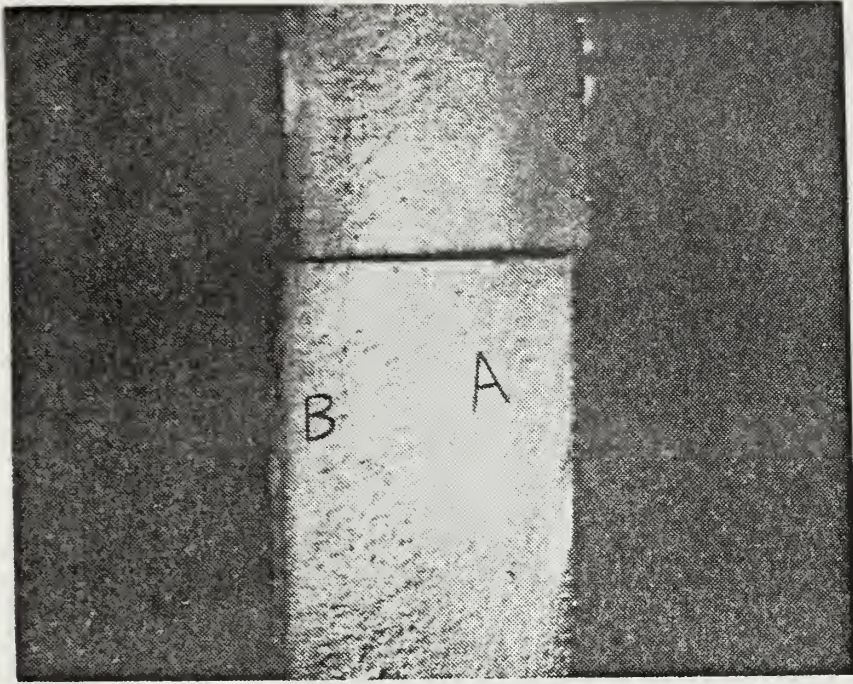


Figure 30. Fatigue fracture surfaces of AR-3-7, fractured after 161,600 cycles at 60 ksi, showing a crescent-shaped fatigue zone with one crack nucleus. X10.

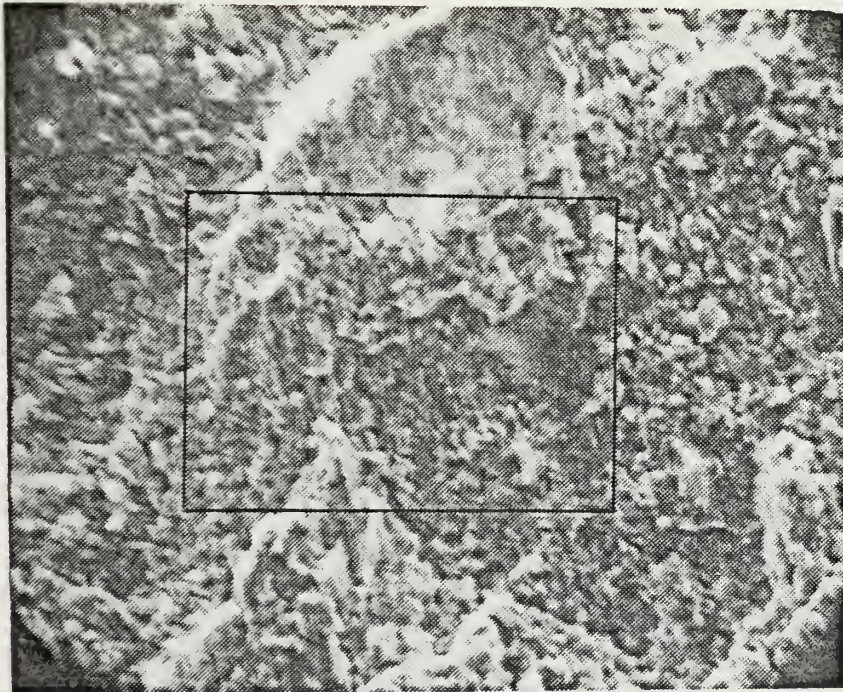


Figure 31. SEM fractograph of Fig. 30, in the fatigue zone, showing transgranular fracture and many secondary cracks. X1200.





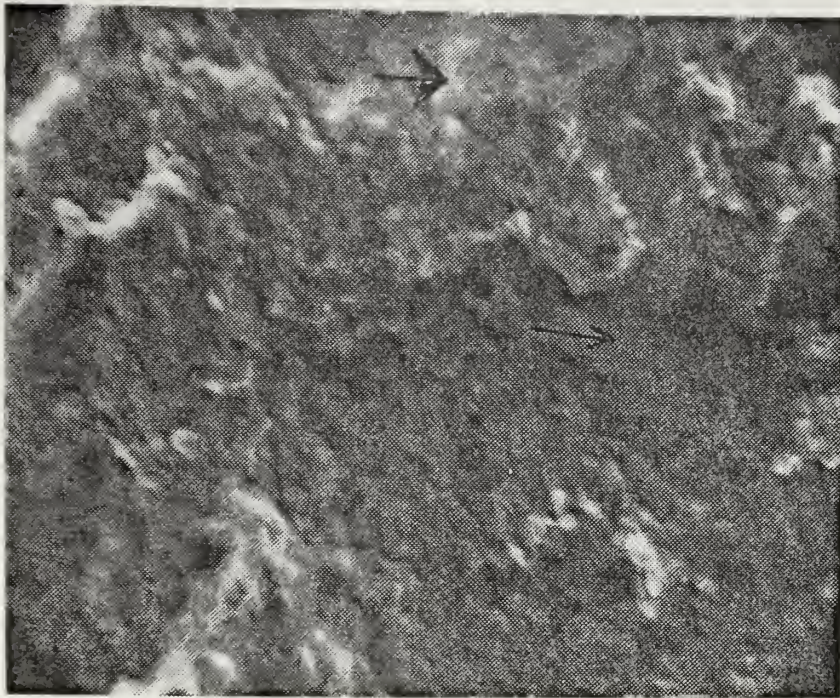


Figure 32. Area outlined by the rectangle in fractograph of Fig. 31. Shown at higher magnification are the fatigue striation shape, secondary cracks and cleavage facets (such as at arrows). X2400.

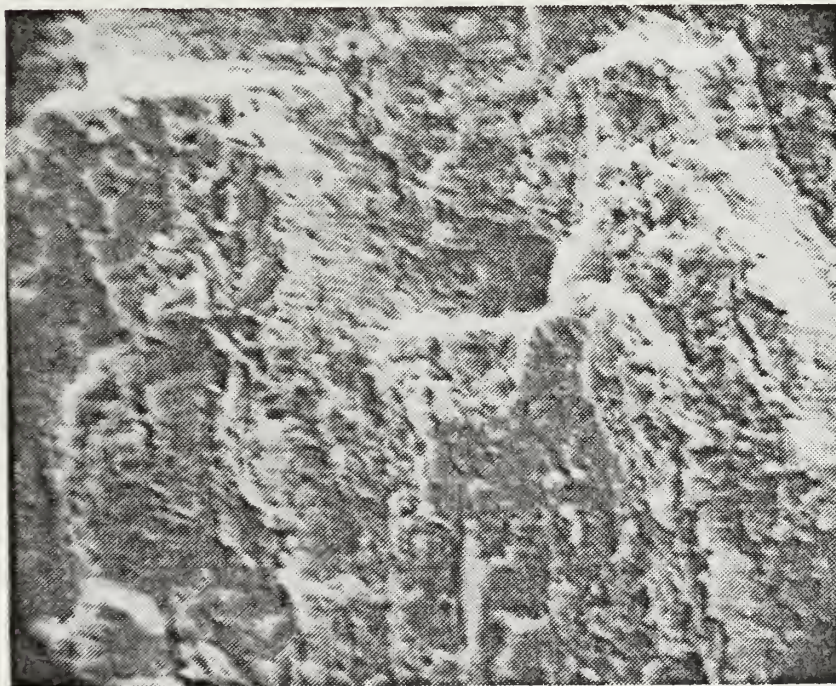


Figure 33. Higher magnification view of the fast fracture region B of Fig. 30, showing characteristic fracture surface of "lamella shape." X1200.





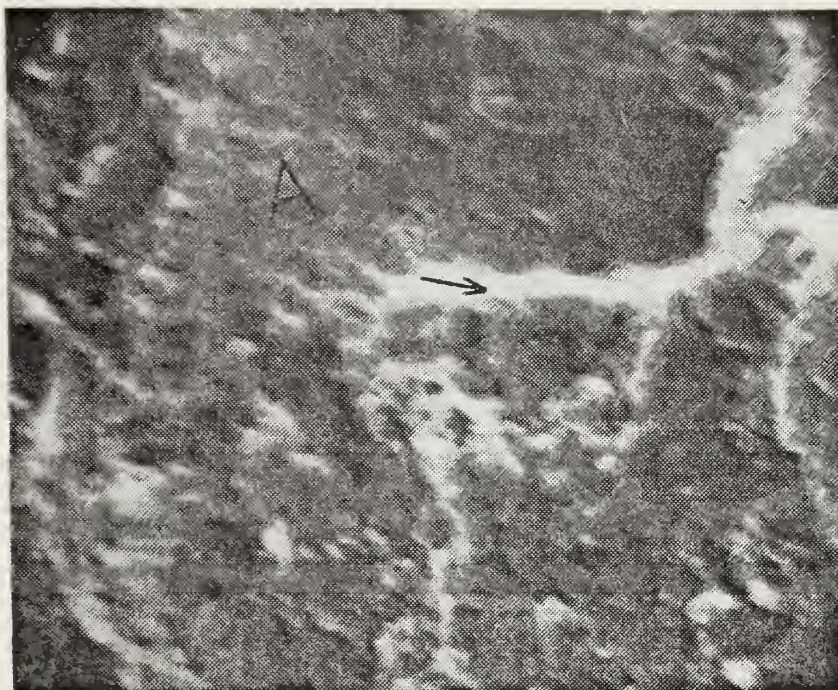


Figure 34. Higher magnification view of Fig. 33, showing tear ridges (at arrows), cleavage facets (A) and crack striations. Irregular microvoid coalescence is evident. X2400.



Figure 35. SEM micrograph of an electro-polished and ion-etched sample showing fine carbide particles dispersed in a ferrite matrix. X5000.





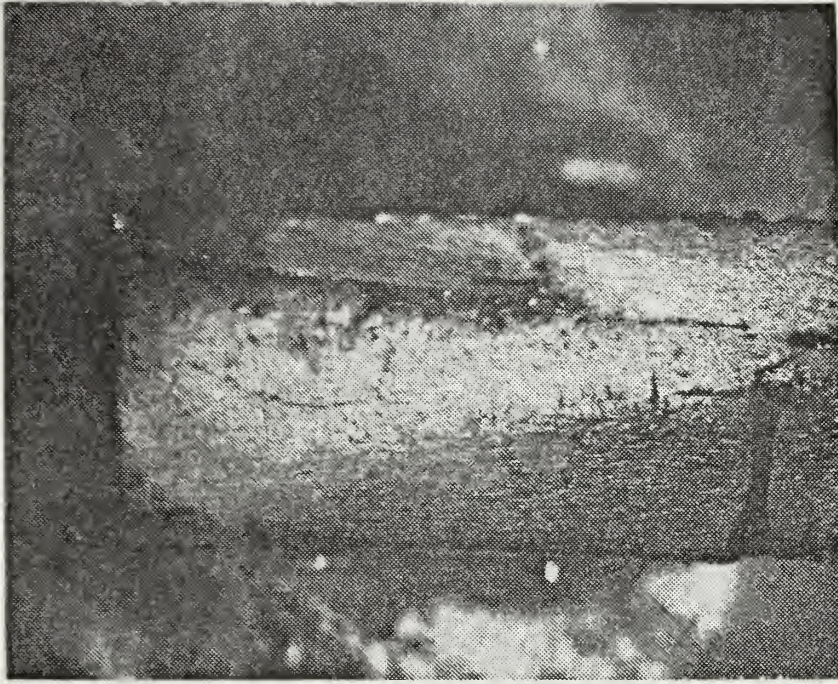


Figure 36. Fatigue fracture surface of specimen AR-4-9, fractured after 7,700,000 cycles at 49 ksi, showing two fatigue zones. X10.

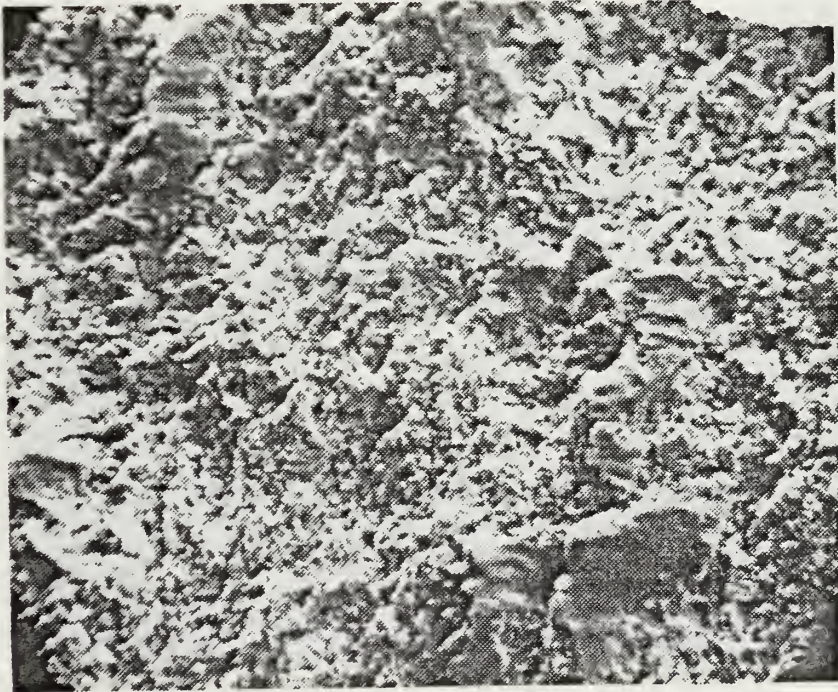


Figure 37. SEM fractograph of Fig. 36, showing a transgranular ductile fracture mode of very fine size. X1050.





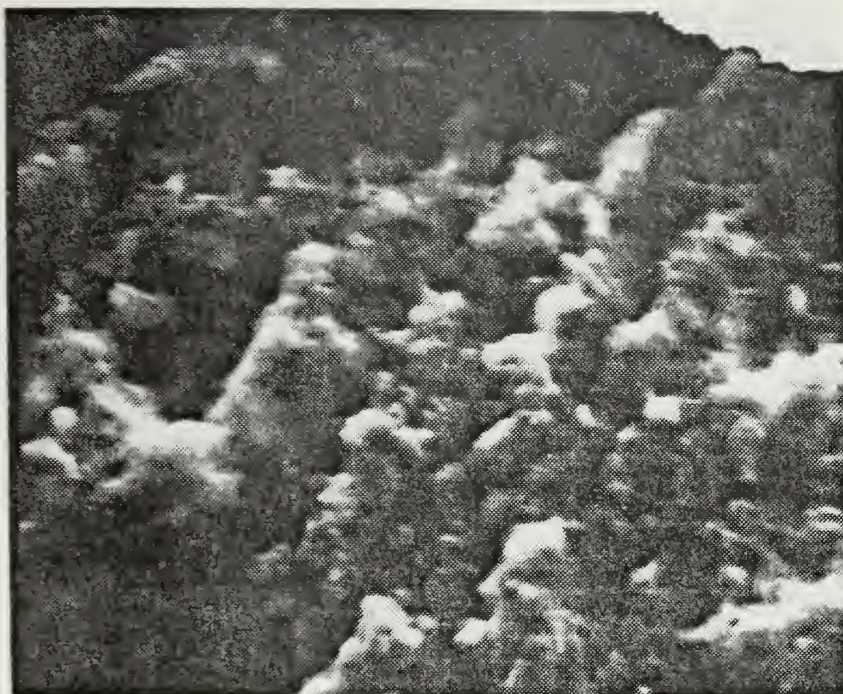


Figure 38. Higher magnification in fatigue zone of Fig. 30, showing cleavage facets and irregular dimples. The grain size is seen to be very small. X5300.

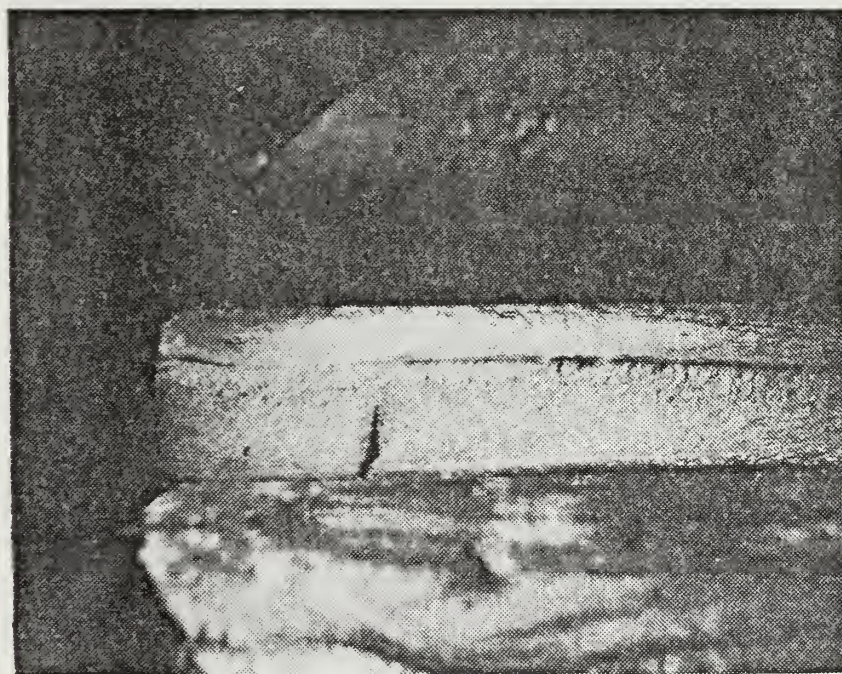


Figure 39. Fatigue fracture surface of specimen AR-4-10, fractured after 100,000 cycles at 66 ksi, showing four initiate sites and intersection of two fatigue zones. X10.





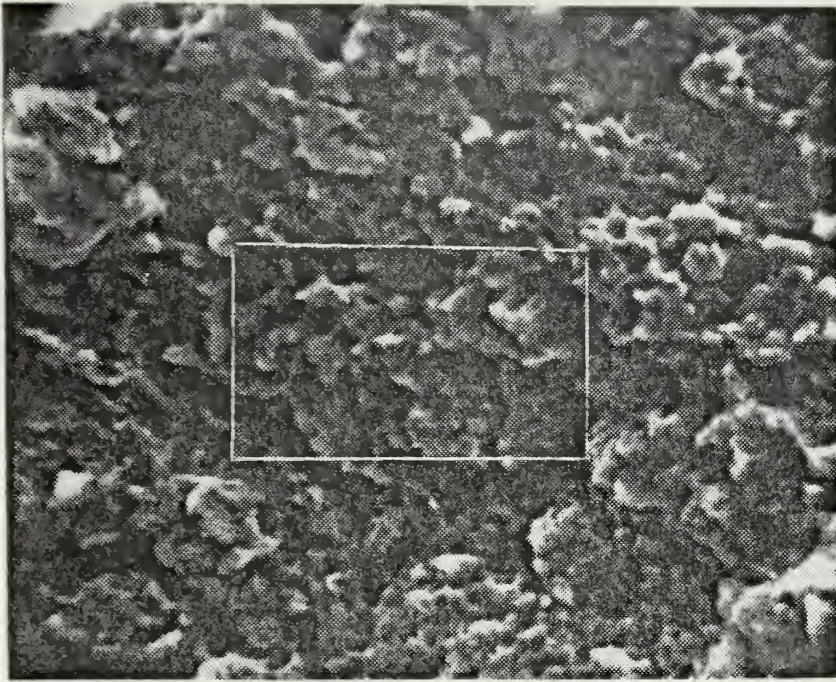


Figure 40. SEM fractograph of fast crack propagation region of Fig. 39, showing irregular dimples and cleavage facets which are separated by secondary crack striations. X2400.

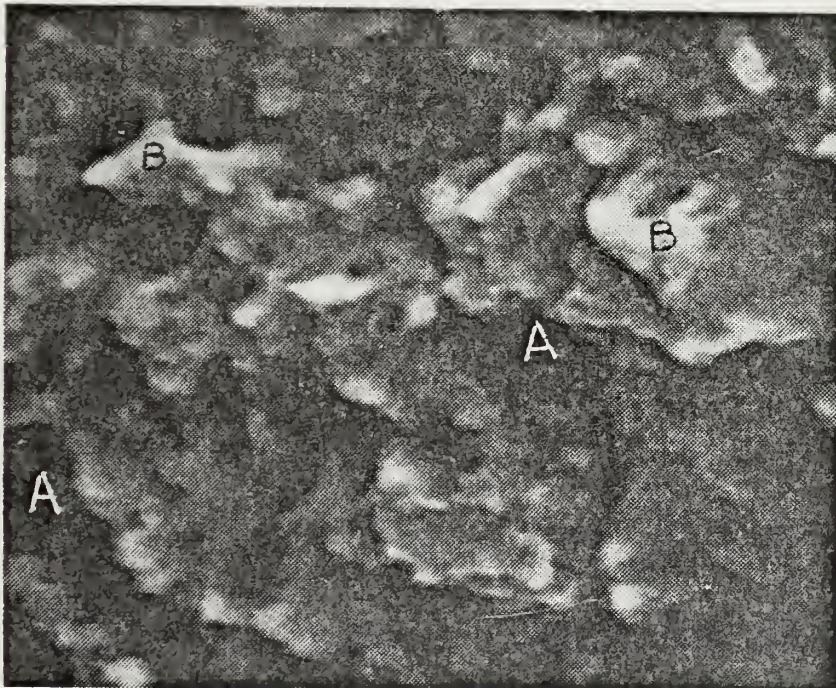


Figure 41. Higher magnification of area in Fig. 40 outlined by the rectangle showing secondary cracks (A), cleavage facets (B) and dimples. X5000.







Figure 42. Micrograph of specimen AR-4-10 in Fig. 39, etched with 2% nital + 2% picric acid solution for 10 seconds. The rolling direction is parallel to the plane of the specimen and horizontal in the micrograph. X100.



Figure 43. Higher magnification of the specimen in Fig. 42, showing a directional dispersion of fine carbide particles in the ferrite matrix. X400.





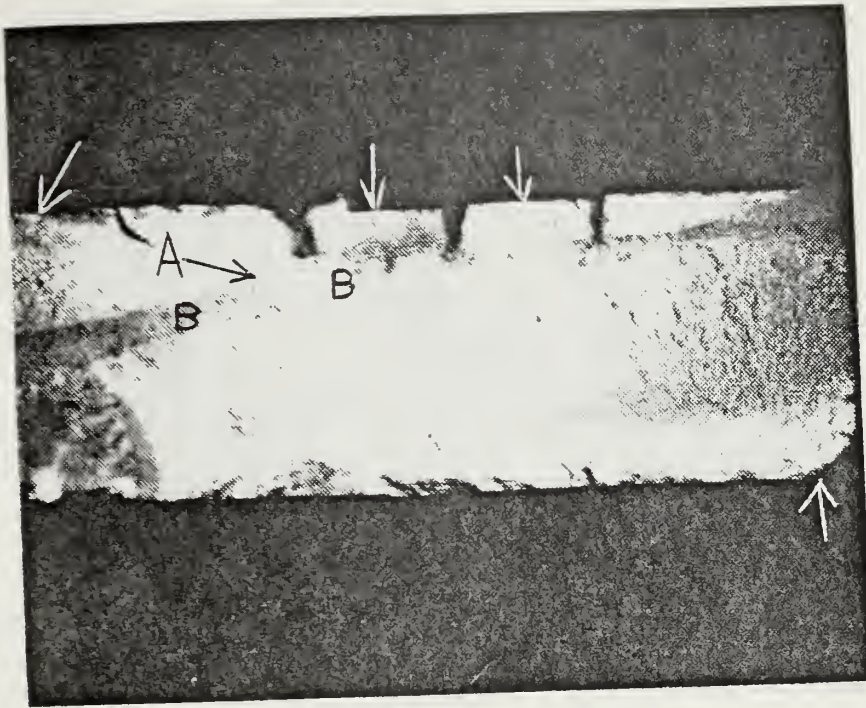


Figure 44. Macro-fractograph of a specimen AR-1-2 which was fractured after 25,300 cycles at 100 ksi, showing several fatigue zones with different crack origins (arrows) occupying the entire fracture surface. Boundary line A is a ratchet mark. Band area B is the fast fracture zone. X10.

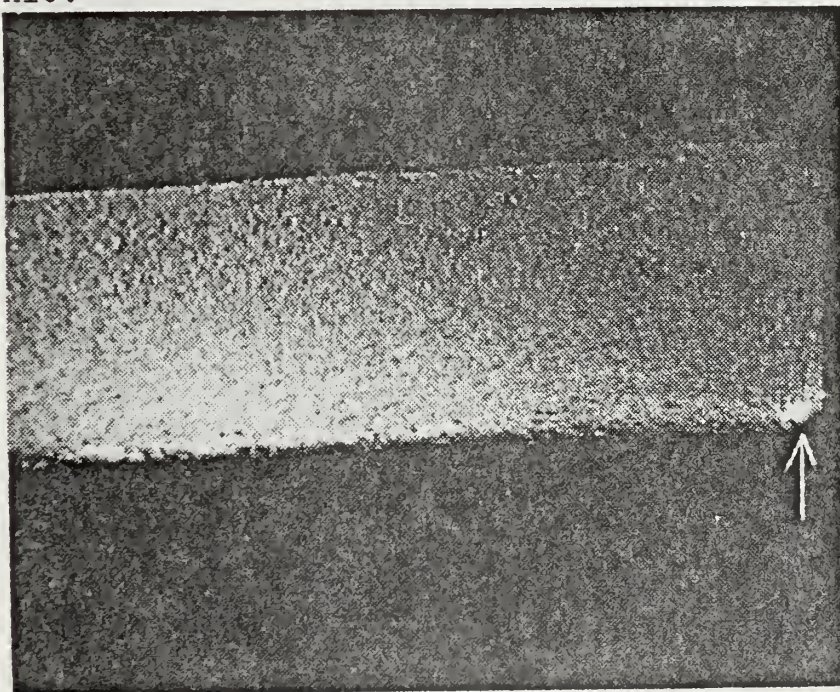


Figure 45. Macro-fractograph of a specimen AR-1-3 which was fractured after 185,700 cycles at 65 ksi, showing fatigue zone with one crack origin, occupying the entire fracture surface. Radial marks indicates crack initiation site. X10.





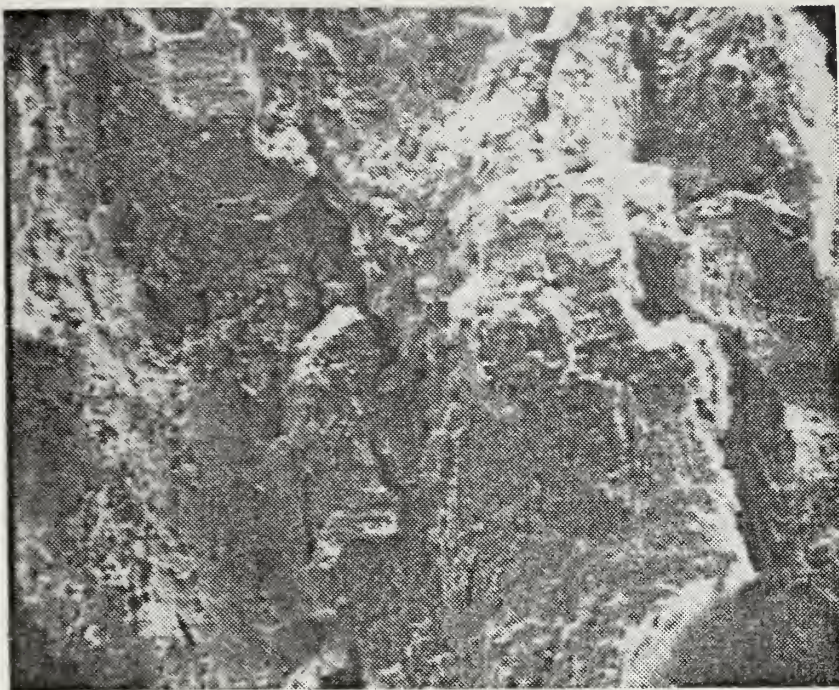


Figure 46. SEM fractograph of a specimen of Fig. 44 in the intersection of fast crack zone and fatigue zone, showing deep secondary cracks normal to the direction of rolling. Tear ridges and dimples are visible. X500.



Figure 47. Fractograph of fast crack zone B of Fig. 44 showing typical lamella-shaped secondary cracks in warm-rolled material. Fracture mode is mostly brittle. X1000.





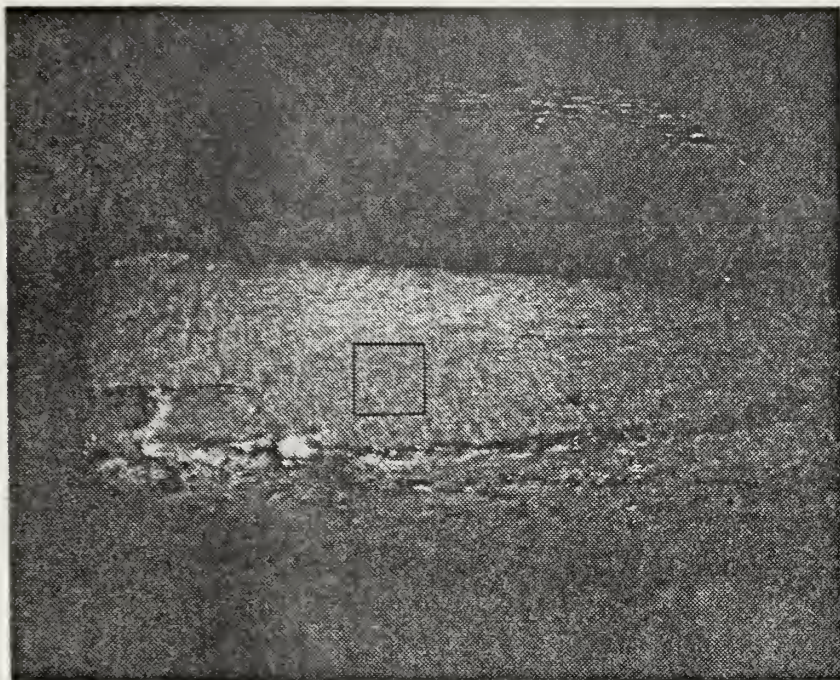


Figure 48. Macro-fractograph of a specimen AR-5-5 which was fractured after 342,800 cycles at 65 ksi, showing half moon shaped fatigue zone with one crack origin and fast fracture zone. X10.

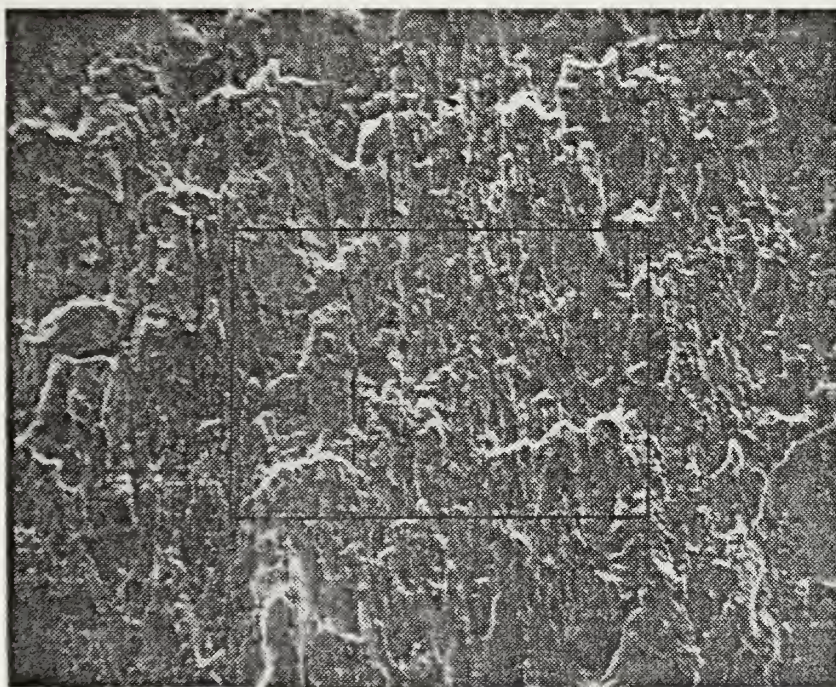


Figure 49. SEM fractograph of Fig. 48 specimen, shows mostly brittle fracture with cleavage facets and many secondary cracks. This area is outlined by rectangle in Fig. 48. X500.







Figure 50. Higher-magnification view of the outlined area in Fig. 49, showing quasicleavage fracture with tear ridges. X1000.

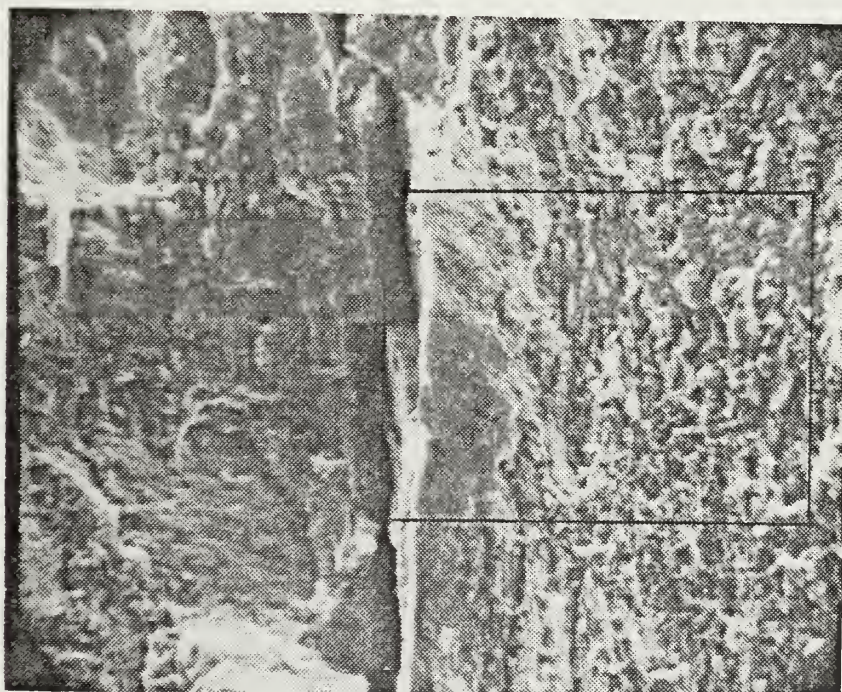


Figure 51. Fractograph on the boundary between the fatigue zone and fast fracture zone in the same specimen of Fig. 50. Quasicleavage with deep secondary cracks is evident. X1000.





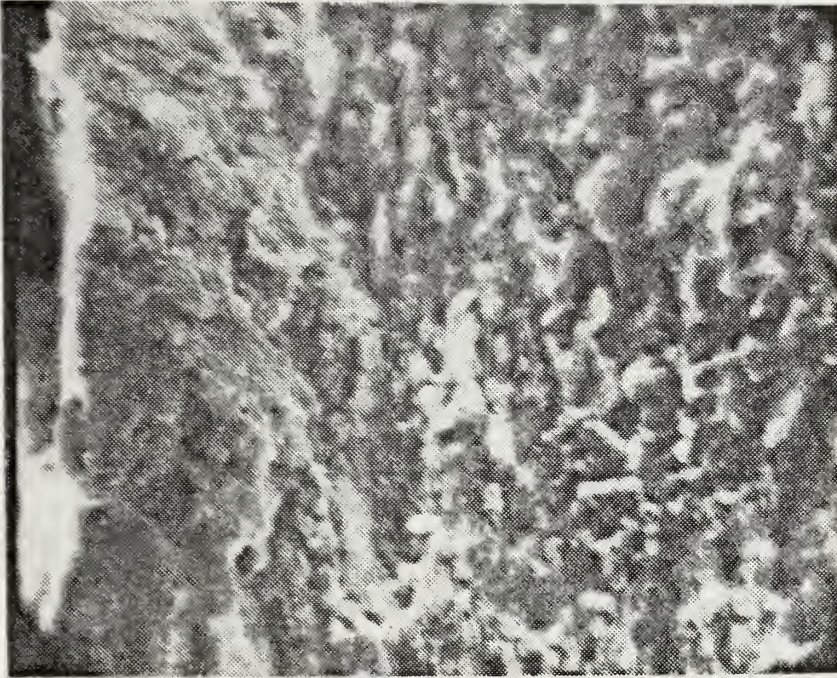


Figure 52. Area outlined by the rectangle in Fig. 51 showing fragmentary fatigue striations, many of which are associated with fissures. X2000.



The SEM fractographs of Specimen Groups AR revealed normally ductile and brittle fracture modes with a number of typical lamella-shaped secondary cracks. These secondary cracks occur in "bunches" and lie normal to the rolling direction, apparently the result of residual stress induced during warm-rolling.

The macro-fractographs of these specimens reveal large fatigue zone and several crack initiation sites. Specimens tested at higher stresses show more crack initiation sites than those tested at lower stresses.

## 2. Specimen Group QT

The microstructure of Group QT, which was conventionally heat treated, reveals large, spheriodal carbide particles dispersed in a matrix of fine martensite and retained austenite (Figure 53). Each macro-fractograph showed a relatively flat, coarse fracture surface without shear lips. Because of the flat fracture surface and absence of any indications of secondary cracking, it is apparent that only one initiation site existed. It is hard, however, to distinguish its exact location. There was no fatigue zone in the fracture surface; a fibrous zone occupied the entire fracture surface. These fracture surfaces are presented in Figures 53 through 56.

The SEM fractographs reveal a brittle fracture surface with partly transgranular fracture and irregular microvoid coalescence (Figures 57 through 60).







Figure 53. Microstructure of specimen QT-0-3, etched in 2% Nital + 2% picral solution for 10 seconds, showing dispersed spheroidal carbides in a matrix of fine martensite and retained austenite. X400.

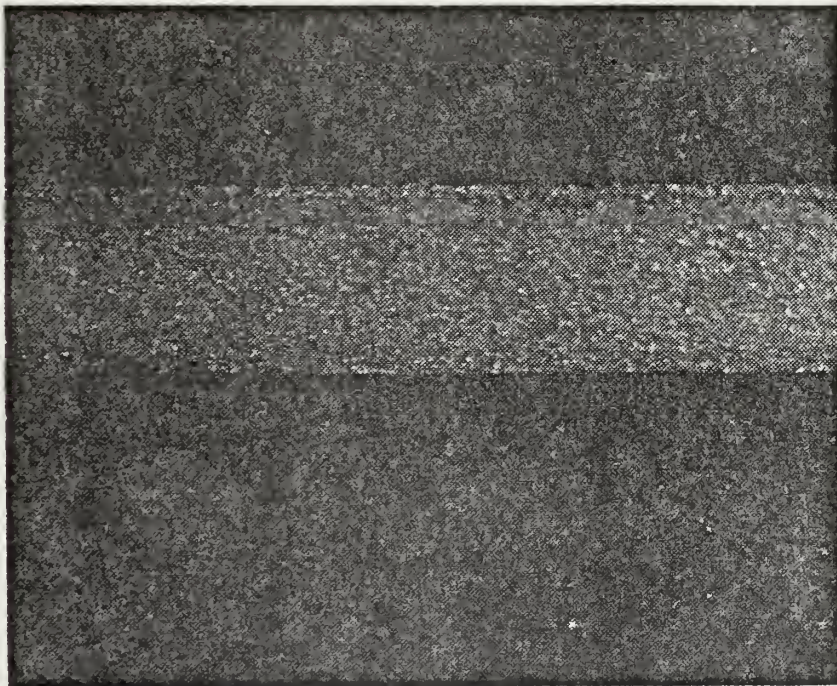


Figure 54. Macro-fractograph of a specimen QT-0-8, fractured after 5,500 cycles at 100 ksi, showing a flat but coarse fracture surface. X10.





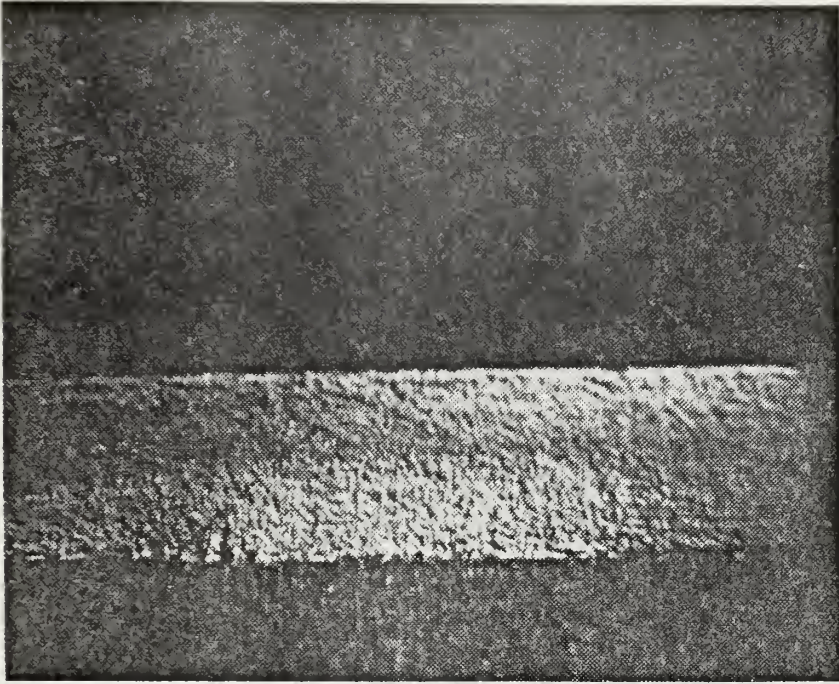


Figure 55. Macro-fractograph of a specimen QT-0-1, which was fractured after 5,300 cycles at 65 ksi, showing half-moon shaped fibrous zone and coarse but flat surface. X10.

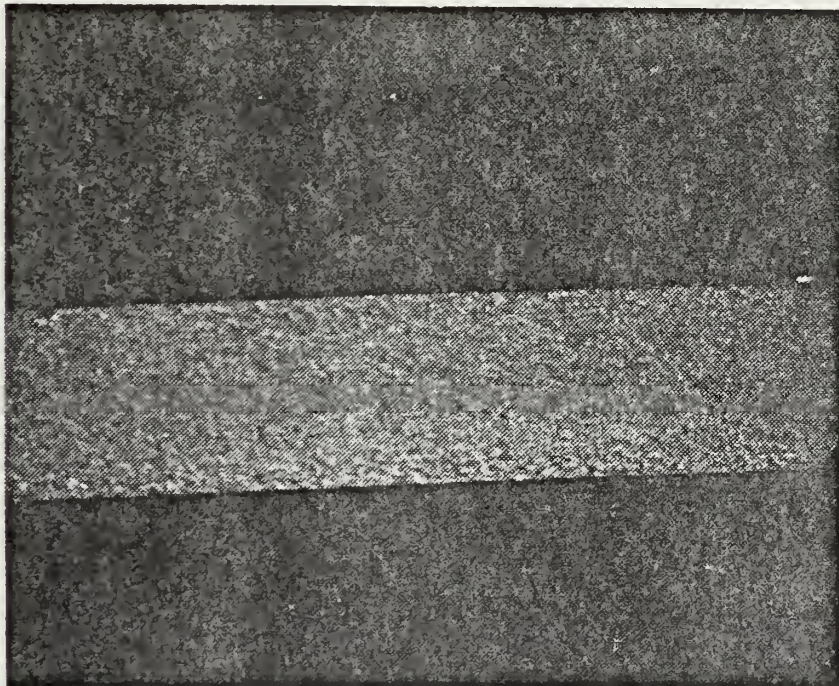


Figure 56. Macro-fractograph of specimen QT-0-5, which was fractured after 46,100 cycles at 48 ksi. Even though tested at a low stress, there is no fatigue zone. X10.





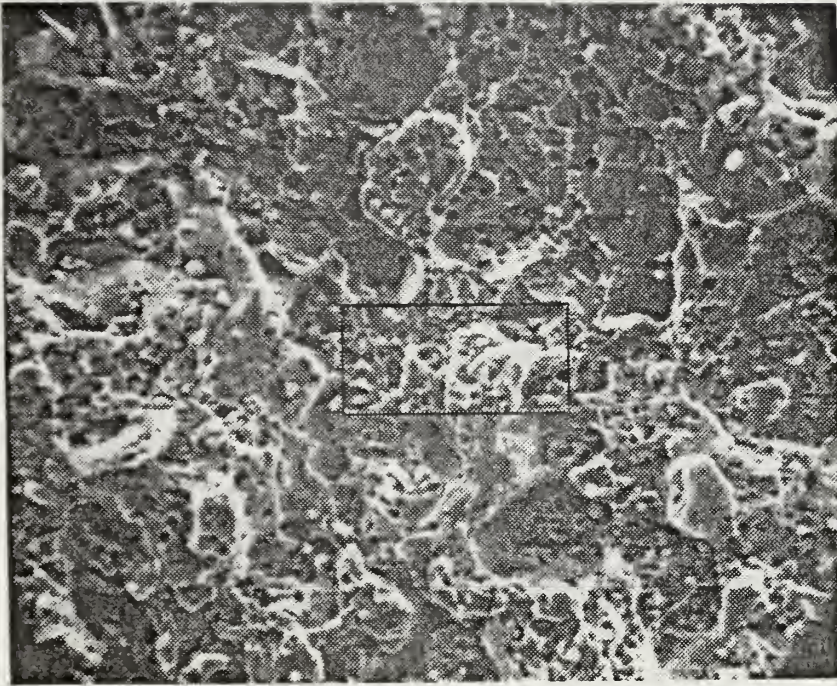


Figure 57. SEM fractograph of the specimen of Fig. 53, fractured after 1,494,400 cycles at 39 ksi, showing partly intergranular fracture and partly transgranular fracture. Irregular voids and tear ridges (white) are evident. X1000.

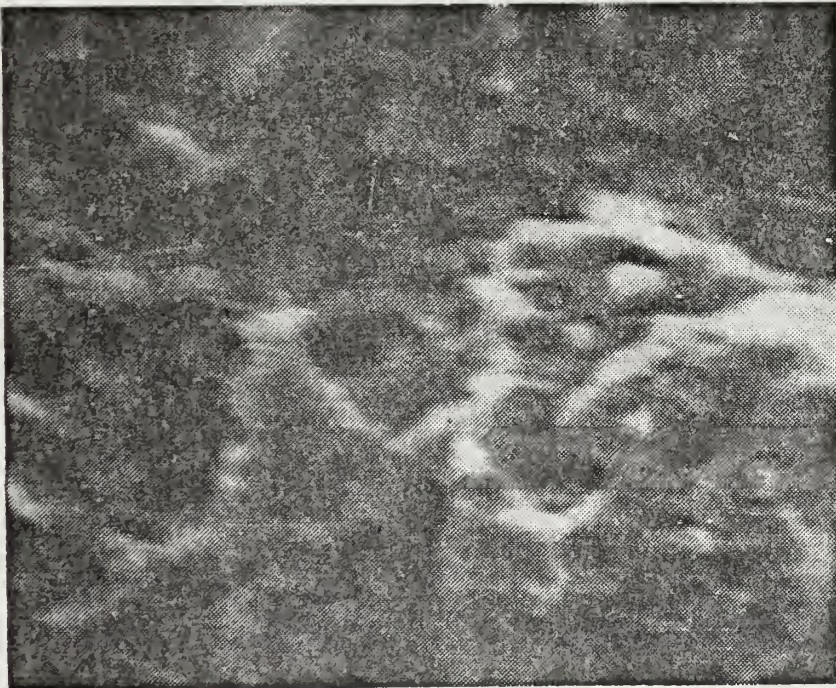


Figure 58. Higher magnification view of the area in Fig. 57, outlined by rectangle, showing large irregular dimples on intergranular fracture surfaces. X5000.





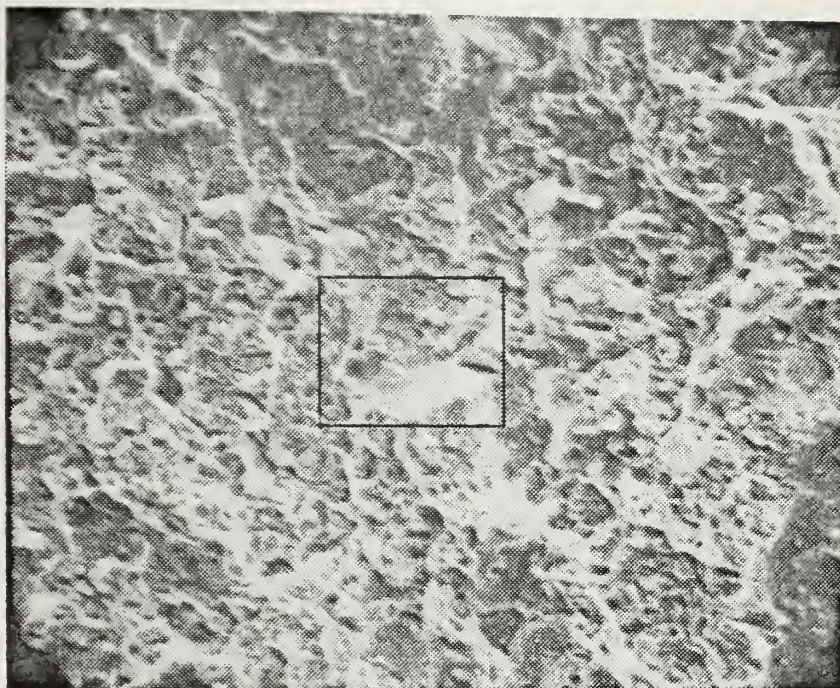


Figure 59. SEM fractograph of specimen QT-0-6, which was fractured after 12,300 cycles at 100 ksi, showing a partly intergranular and partly transgranular fracture surface. It is rated as 70% brittle and 30% ductile. Dimple are visible both on the brittle and ductile fracture areas on the surface. X1000.

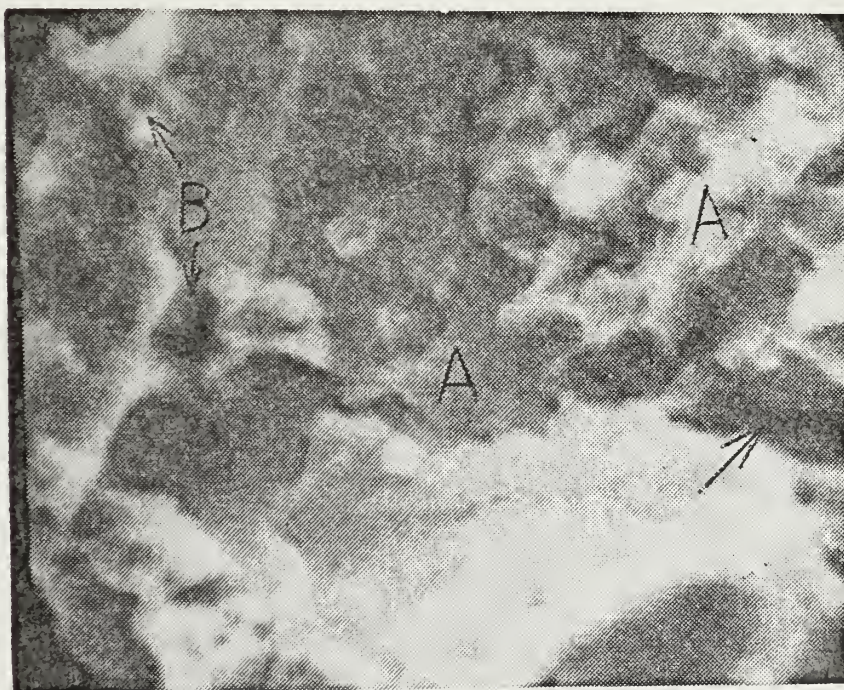


Figure 60. The area outlined by rectangle in fractograph Fig. 59, shown at higher magnification; brittle cleavage facets (marked A), deep secondary cracks (at arrow) and dimples (marked B) are evident. X5000.



### 3. Specimen Group QI

The macro-fractograph (Figures 61-62) revealed a flat but coarse fracture surface without shear lips. The fracture surfaces revealed no fatigue zone and no indication of crack initiation sites or associated fibrous zones. The SEM fractographs showed primarily intergranular crack modes with large "rock candy" features indicating a brittle, intergranular fracture mode (Figures 63 through 68). The microstructure of this specimen showed very coarse, acicular needles of bainite and martensite (Figure 69).





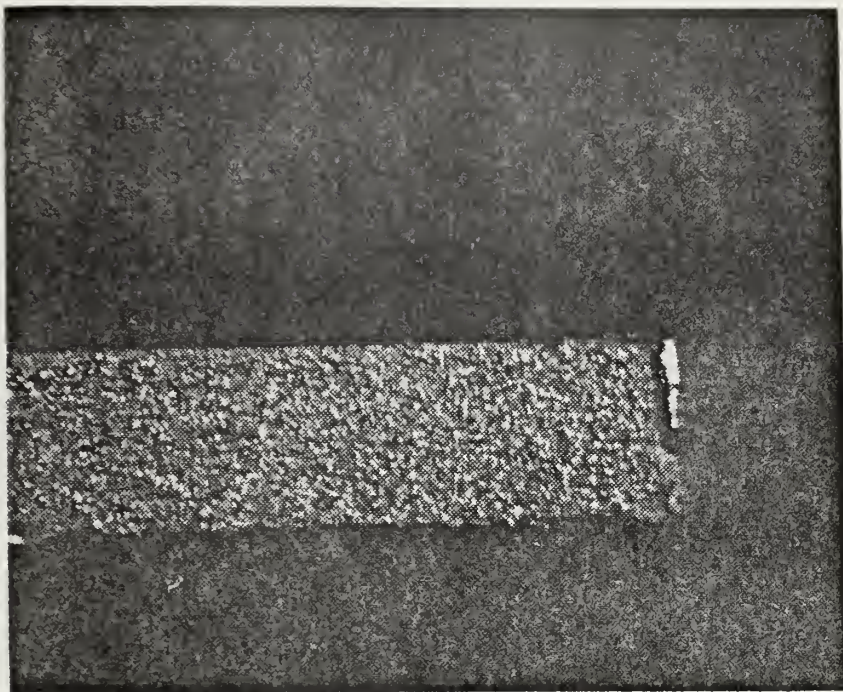


Figure 61. Macro-fractograph of specimen QI-0-5 which was fractured after 20,000 cycles at 100 ksi; the absence of a fatigue zone is evident as is a coarse fracture surface. X10.

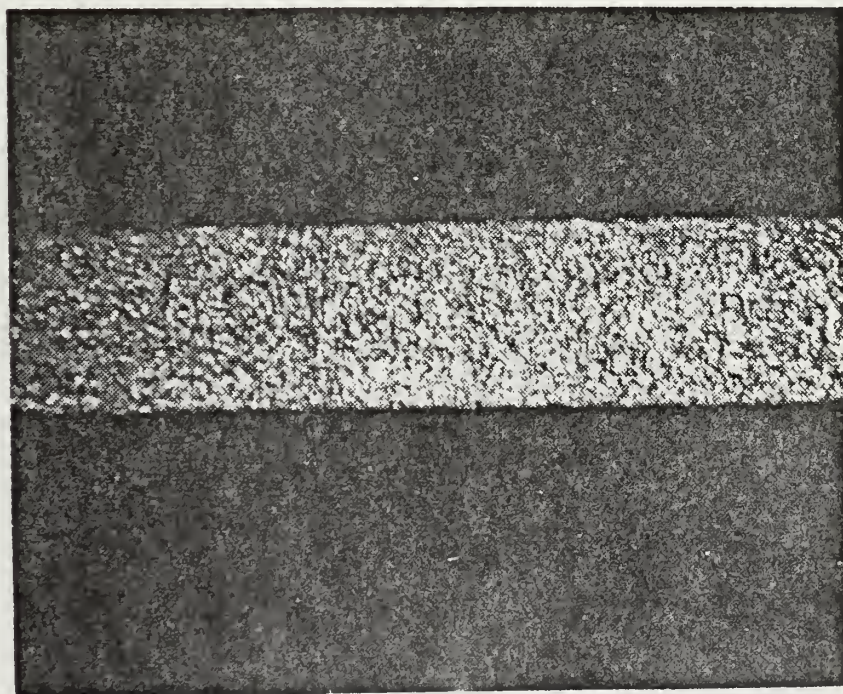


Figure 62. Macro-fractograph of a specimen from the same group as in Fig. 61. QI-0-7, which was fractured after 1,321,300 cycles at 40 ksi, shows a coarse fracture surface and absence of fatigue zone. X10.





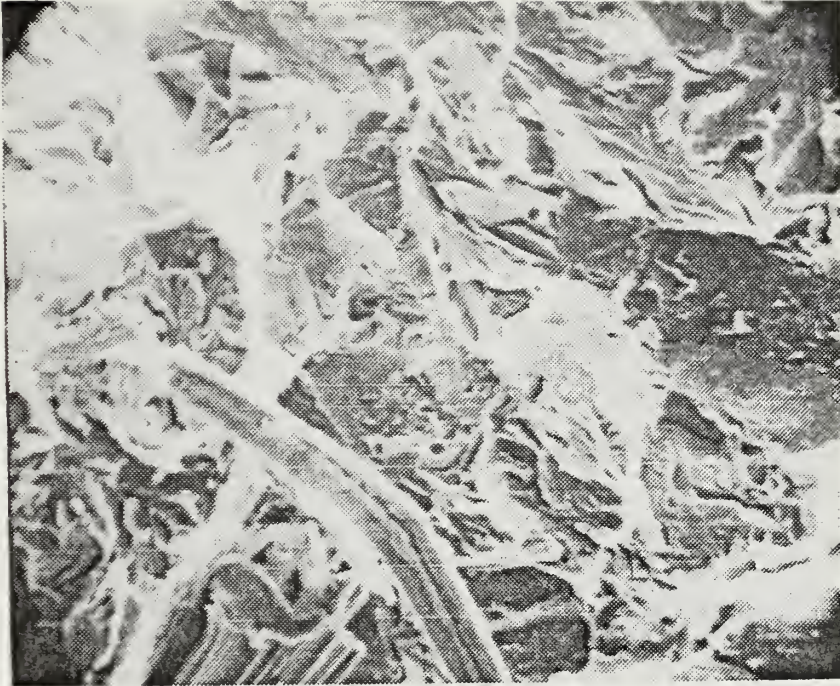


Figure 63. SEM fractograph of specimen QI-0-3, fractured after 3,000,000 cycles at 39 ksi, showing partly intergranular fracture. The fracture surface is rated as 70% brittle and 30% ductile. Note dimples on the surfaces of "Rock Candy" which are indicative of a large grain size. X1000.

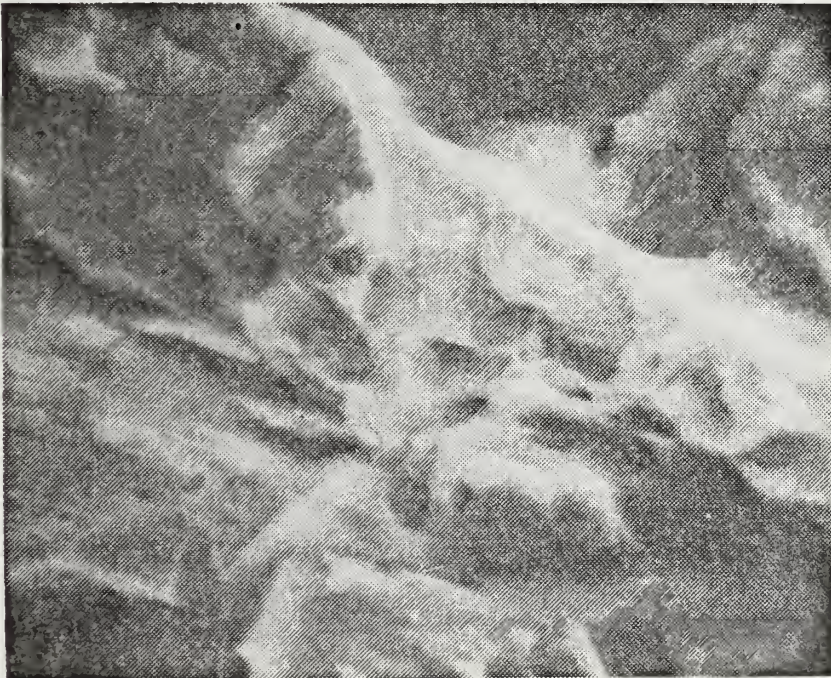


Figure 64. Higher magnification view of Fig. 63, showing dimples oriented in the direction of crack initiation on a transgranular fracture. X5000.





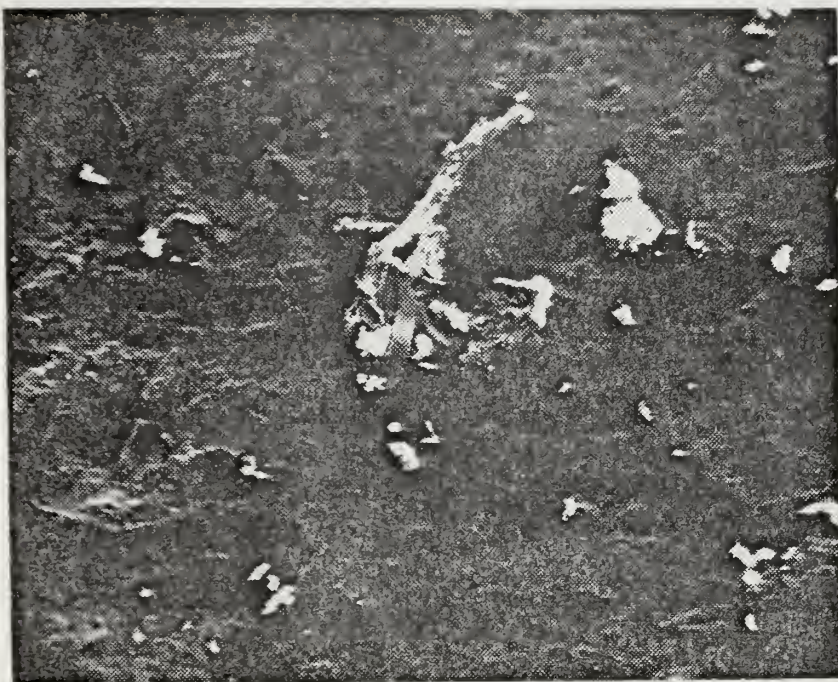


Figure 65. SEM fractograph at low magnification of the same specimen as in Fig. 61, showing a partly intergranular, partly transgranular fracture mode. X100.

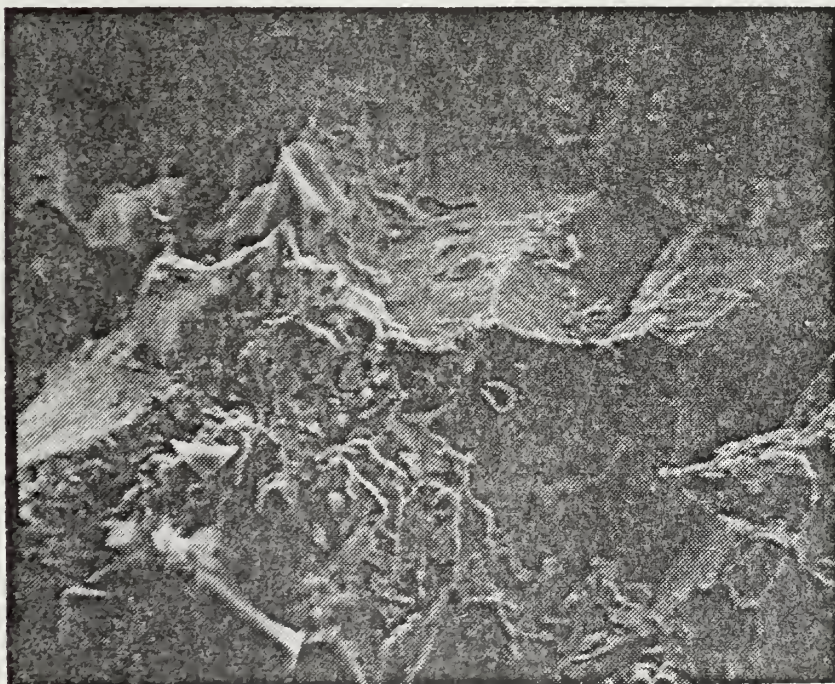


Figure 66. Higher magnification of Fig. 65, which shows brittle and ductile fracture surfaces. Visible are some dimples on large "rock candy" grain boundaries. X1000.





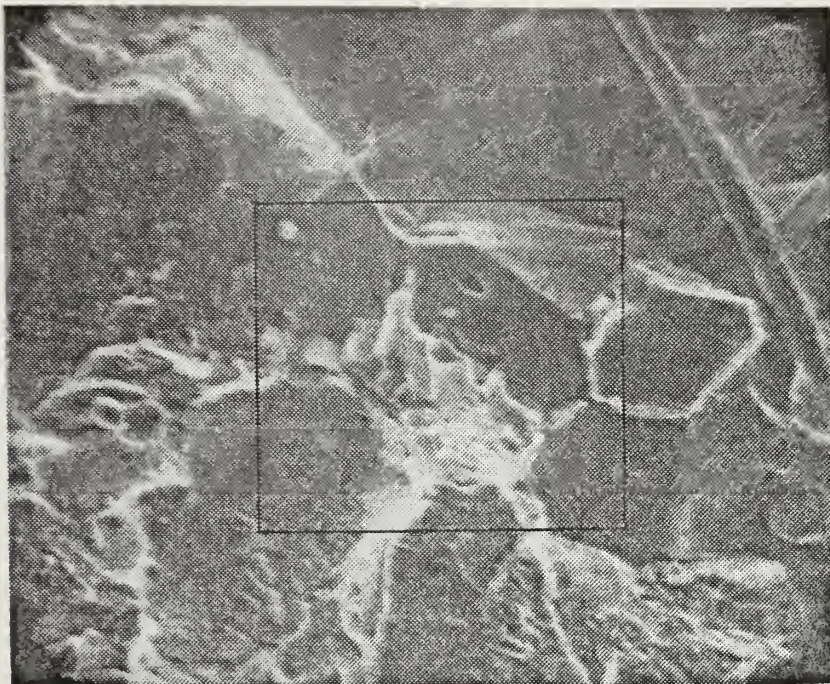


Figure 67. Fractograph of specimen QI-0-8 which was fractured after 212,400 cycles at 65 ksi, showing intergranular fracture (rock candy) and transgranular fracture. Dimples and cleavage facets on intergranular fracture surfaces are evident. X1000.

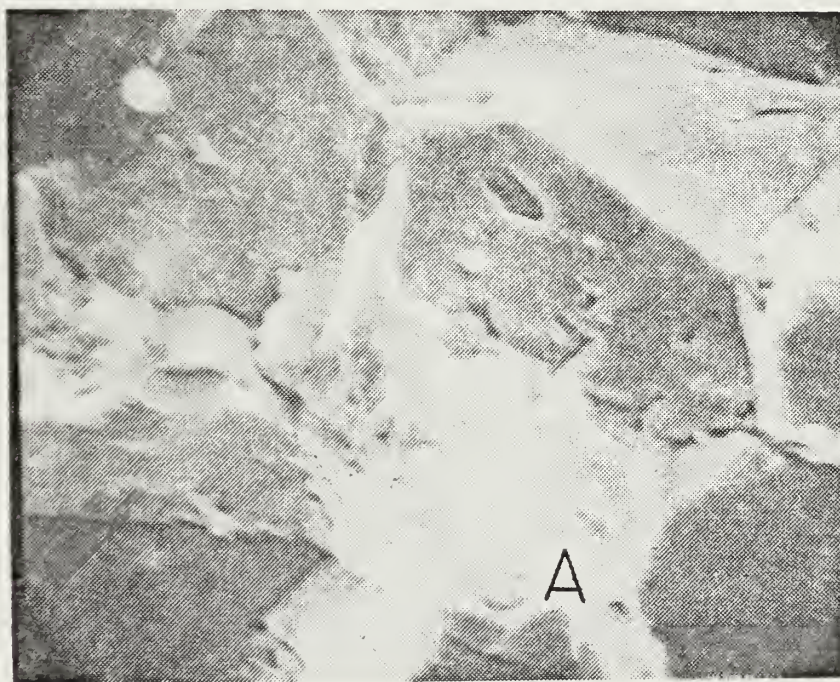


Figure 68. Higher magnification of area outlined by rectangle in Fig. 67; a few dimples on the intergranular fracture surface, due to inclusions, are visible. The radially oriented pattern marked A is the result of local quasicleavage. X2000.





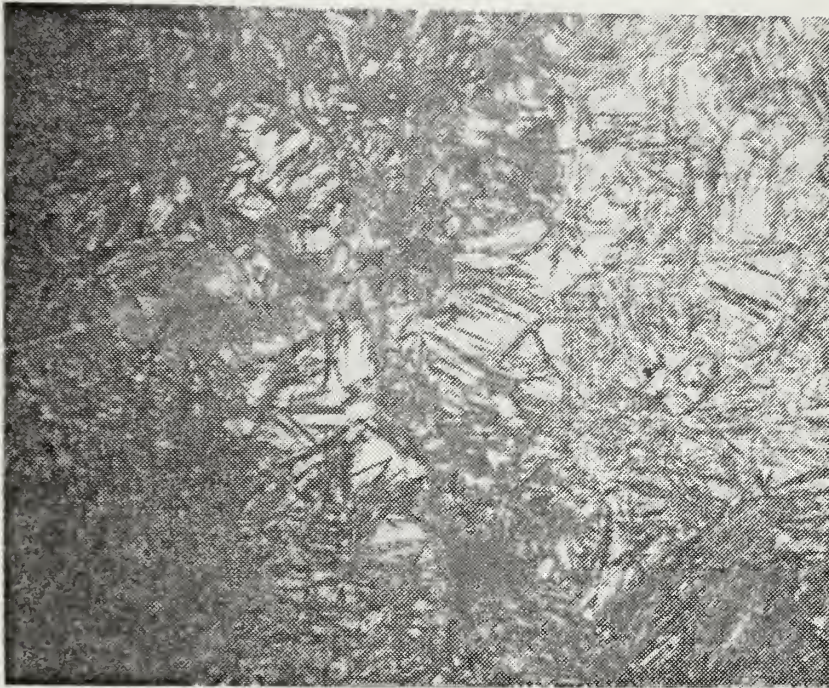


Figure 69. Microstructure of specimen QI-0-7 etched with 2% nital + picral for 10 seconds, showing coarse acicular needles of bainite and martensite based on a pearlite matrix. X400.





#### 4. Specimen Group RQ

The macro-fractograph shows a flat and fine fracture surface with shear lips (Figures 70 and 71). The crack initiation site and fibrous zone were evident, but a fatigue zone was not visible in the fracture surface. The micro-structure of this specimen revealed a combination of fine, tempered martensite, pearlite, and fine dispersed carbide particles (Figure 72). The decarburized layer of this heat treated specimen is shown in Figure 73. The depth of decarburization was 90-145  $\mu\text{m}$  and the grain size in that area was very coarse, 15-30  $\mu\text{m}$ . This large grain size, compared to the rolled condition, is a result of rapid grain growth during austenitizing because there are no obstacles, i.e carbides, to impede the grain growth. The decarburized side surface of the specimen probably did affect the fatigue performance during this test. The SEM fractographs in Figure 74 and 75 revealed a transgranular, but quite brittle fracture mode with cleavage facets and an uneven array of dimples.



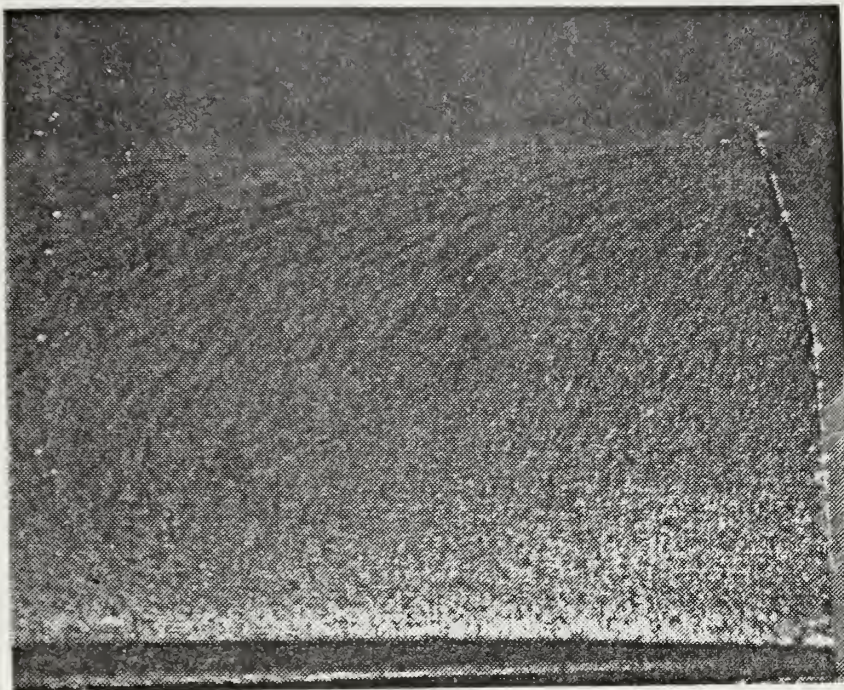


Figure 70. Macro-fractograph of specimen RQ-0-1, which was fractured after 16,500 cycles at 100 ksi, showing a crack initiation site (upper right corner) and chevron marks. Absence of fatigue zone is evident. X20.

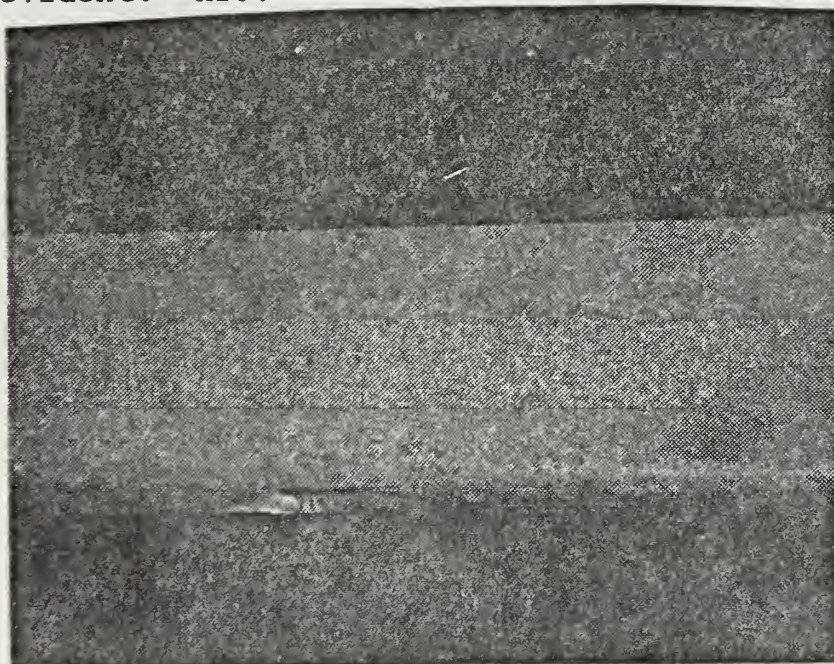


Figure 71. Macro-fractograph of specimen RQ-0-2, which was fractured after 87,800 cycles at 65 ksi, showing flat and fine fracture surface without any fatigue zone or fibrous zone. It appears very brittle. X10.







Figure 72. Microstructure of same specimen as Fig. 73, showing tempered martensite, pearlite and fine dispersed carbide particles. X400.

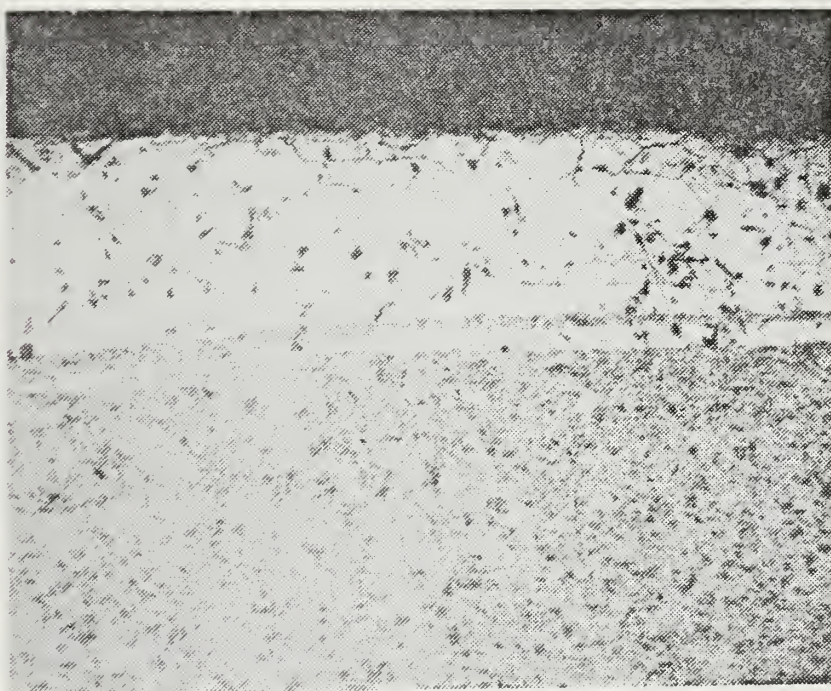


Figure 73. Micro structure of the same specimen as shown in Fig. 70. This shows the decarburized layer of depth 90-145 $\mu$ m and grain size 15-30  $\mu$ m. The lower part shows fine, tempered martensite and pearlite, retained austenite and undissolved carbide particles. Etched with 2% nital + 2% picral solution, 40 seconds. X200.





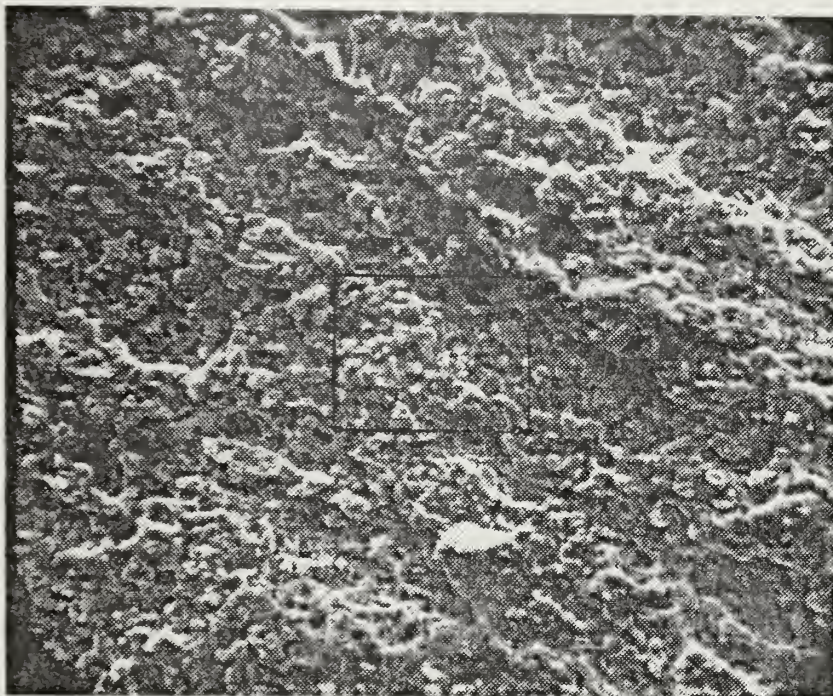


Figure 74. SEM fractograph of the same specimen as Fig. 73, showing an uneven array of dimples facets with a scattering of large voids. X1200.

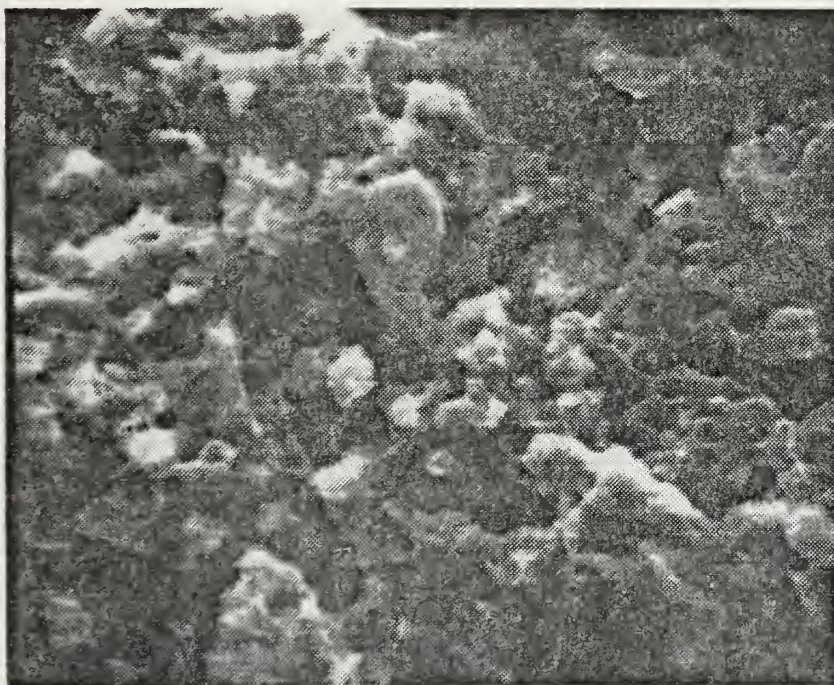


Figure 75. Higher magnification view of the area within the rectangle in fractograph Fig. 74 showing cleavage facets with dimples. X5000.





## 5. Specimen Group RI-1

The macro-fractographs revealed a single crack initiation site and a large fatigue zone. The fatigue zone size increased with decreasing maximum stress. The relatively small size of the fatigue zone at a high stress, 100 KSI, is shown in Figure 76. Fracture occurred after 44,300 cycles in this case. Larger fatigue zones produced by decreasing maximum stress are shown in Figures 77 through 80. The crack origin was easy to identify and every specimen had a shear lip on the fast-fracture side of fracture surface. The fracture surface was otherwise flat and the fatigue zone was easily distinguished with the naked eye from the fibrous, fast fracture zone. The SEM fractographs revealed a ductile fracture mode with some quasicleavage facets, indicative of a brittle fracture mode (Figures 81 through 85). The micro-structure showed fine, banded carbide particles based on the fine, tempered martensite structure (Figures 86 and 87). These carbide particles were slightly larger than those of the Specimen Group AR (as rolled condition without subsequent heat treatment).



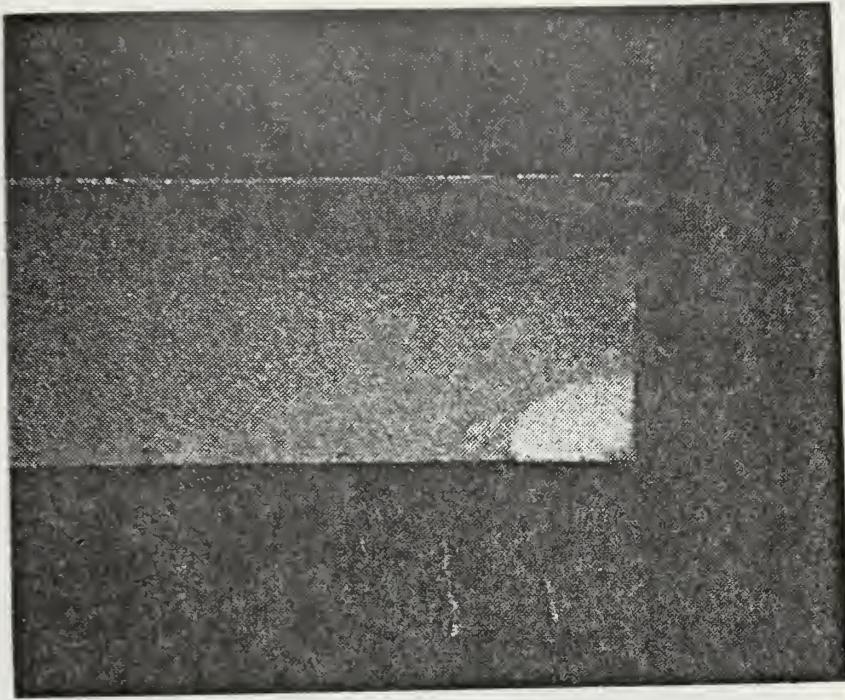


Figure 76. Macro-fractograph of a specimen RI-1-1 which was fractured after 44,300 cycles at 100 ksi, showing the fatigue zone (white quartered circle) with a flat and fine fracture surface. Shear lips are evident at upper edge (white). X10.

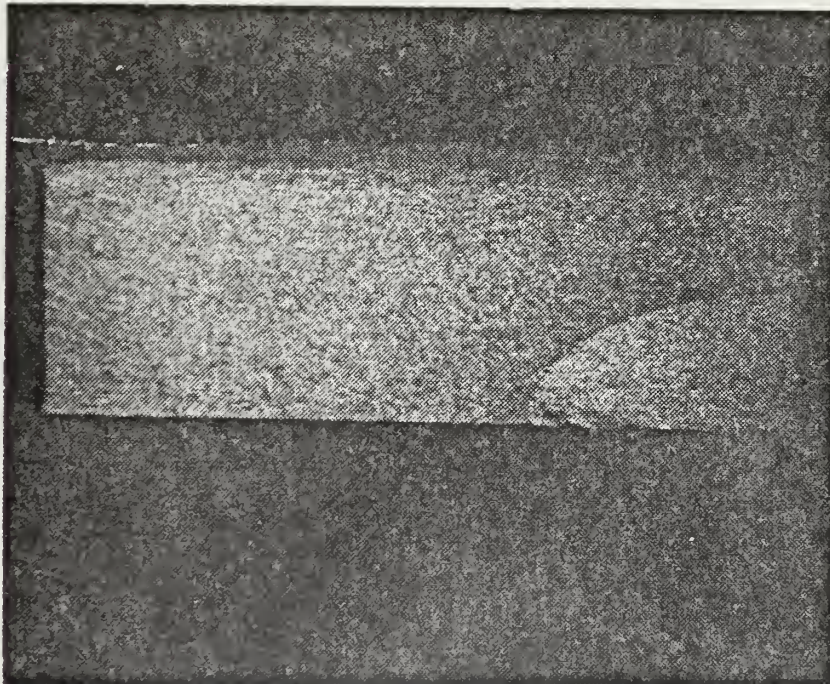


Figure 77. Macro-fractograph of specimen RI-I-2, which was under lower stress than that of Fig. 76. It was fractured after 134,100 cycles at 65 ksi. It is evident that the fatigue zone of this specimen is larger than that of specimen of Fig. 76. X10.





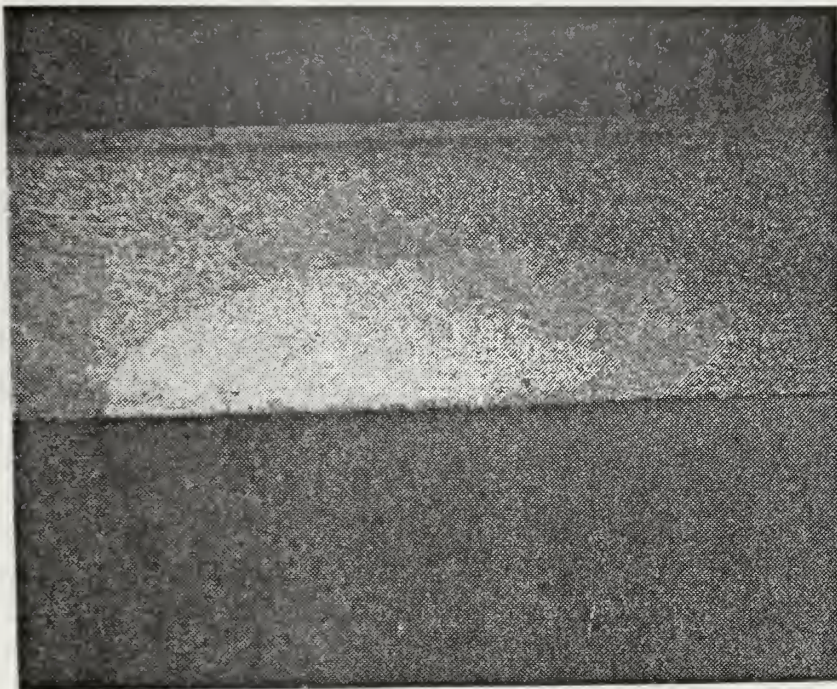


Figure 78. Macro-fractograph of specimen RI-1-4, which was under lower stress than the RI-1-2 specimen in Fig. 77, showing a still larger fatigue zone than Fig. 77. This specimen was fractured after 271,100 cycles at 55 ksi. X10.

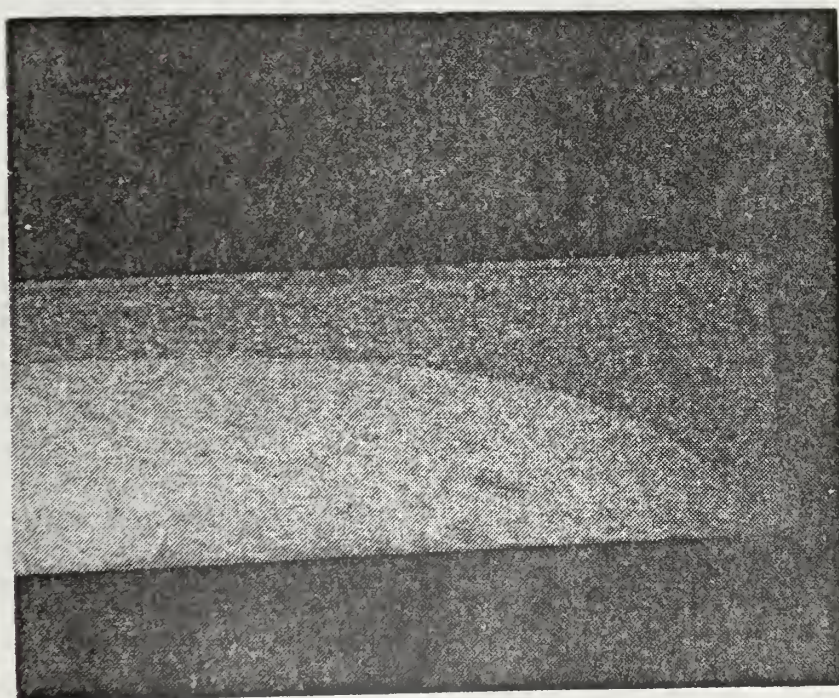


Figure 79. Macro-fractograph of specimen RI-1-6 which was under lower stress than RI-1-4 specimen in Fig. 78, showing a larger fatigue zone than Fig. 78. This specimen was fractured after 3,400,600 cycles at 40 ksi.





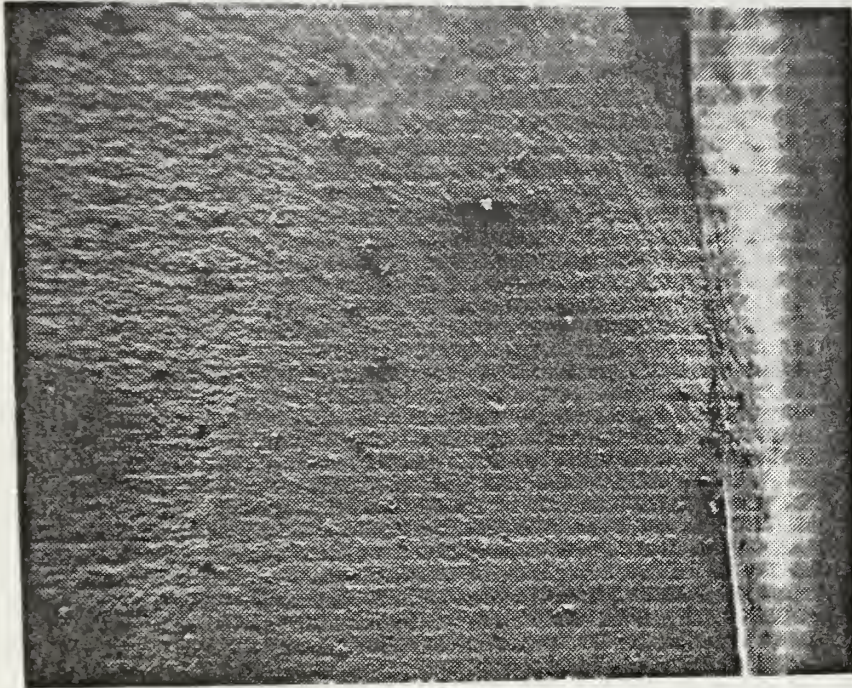


Figure 80. SEM fractograph at low magnification of the same specimen as in Fig. 76, showing the boundary between fatigue zone and fast fracture zone. X55.



Figure 81. Higher-magnification fractograph of the specimen shown in Fig. 80 (RI-1-6) in the vicinity of fracture nucleus (lower right corner in Fig. 80). X2200.





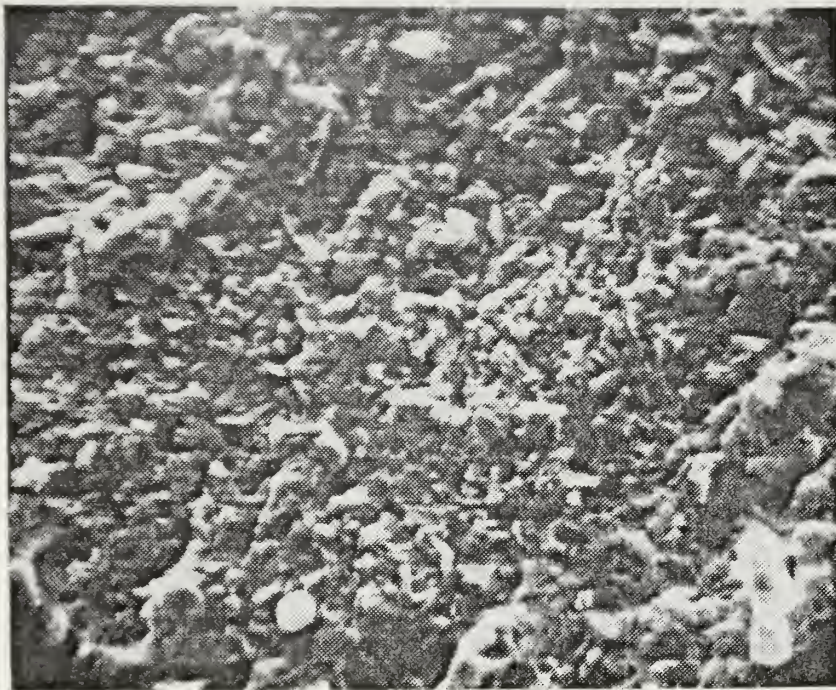


Figure 82. Higher magnification view of Fig. 80 fractograph in the center of the fatigue zone, showing ductile and brittle fracture areas. Note both cleavage facets and dimples. X2200.

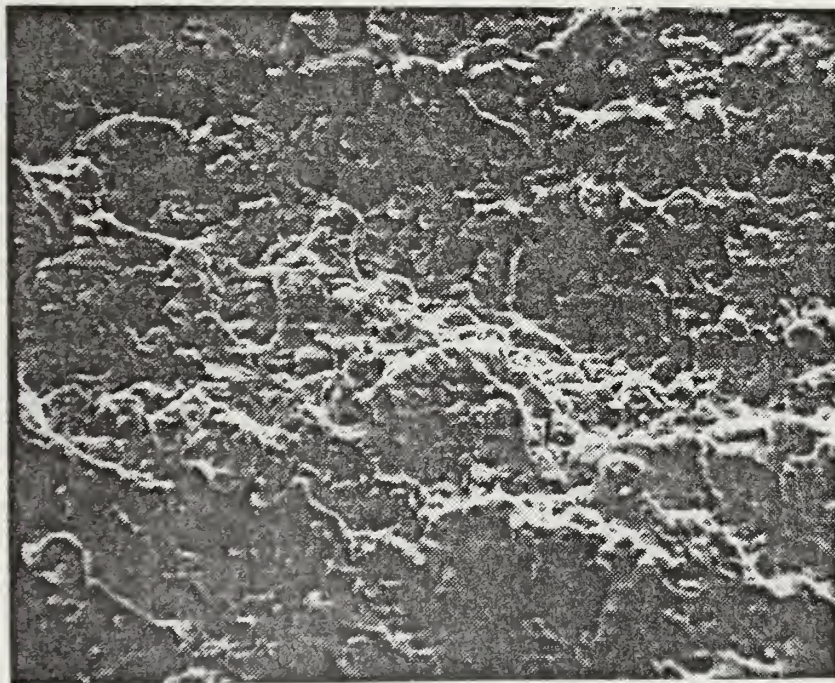


Figure 83. Fractograph of fast fracture zone of Fig. 80, showing shear dimples and tear ridges. The dimples indicate the direction of crack propagation as being from down to up. X1020.





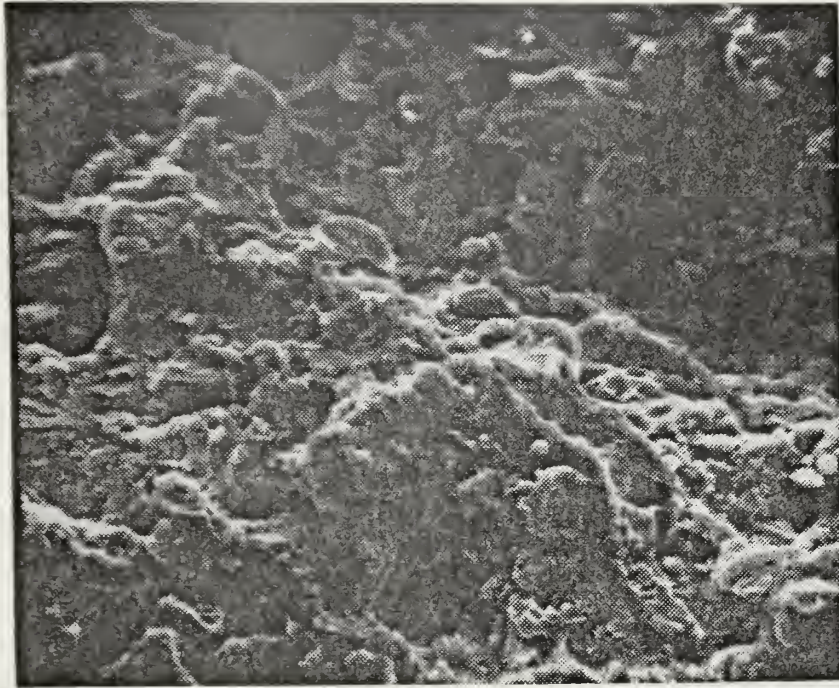


Figure 84. Higher magnification view of Fig. 83 fractograph showing brittle fracture surfaces consisting of cleavage facets with some dimples. X2000.

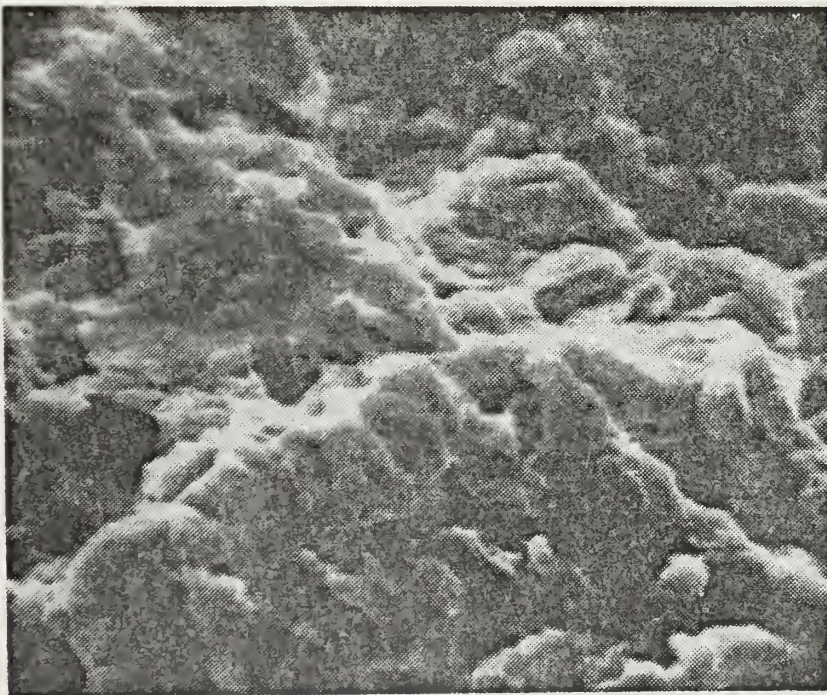


Figure 85. Higher magnification view of Fig. 84 fractograph showing tear ridges in quasicleavage fracture surfaces. X5000.







Figure 86. Microstructure of same specimen as in Fig. 85 (RI-1-6), etched in 2% nital + 2% picral solution for 10 seconds, showing banded carbide particles. X100.

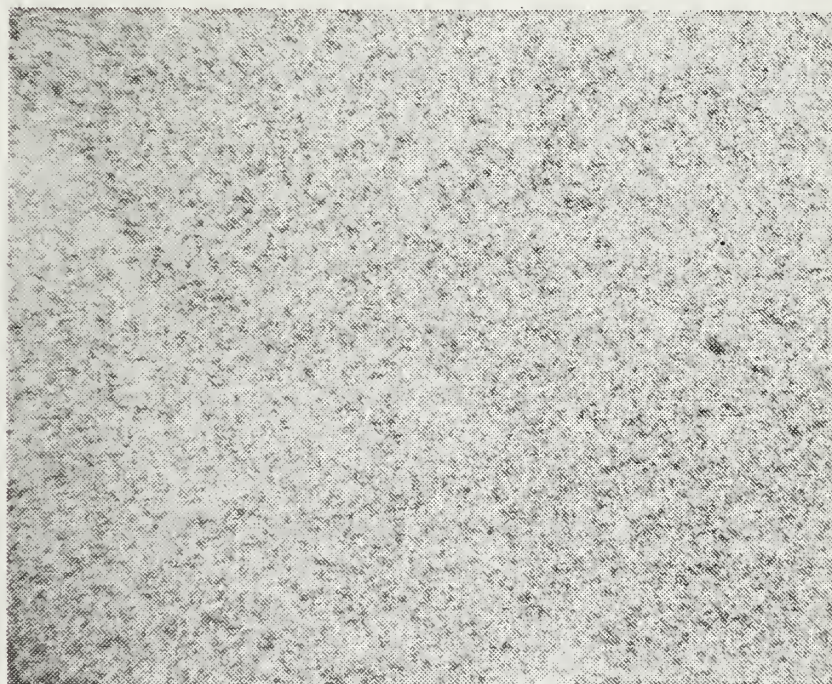


Figure 87. Higher magnification view of microstructure in Fig. 86, showing fine, spheroidal carbide particles distributed in a matrix of fine bainite and martensite. X400.





## 6. Specimen Group RI-2

The macro-fractographs showed uneven fracture surfaces with several sites for crack initiation. Every crack origin has a large fatigue zone, even for those tested under high stress. Ratchet marks, i.e. fatigue cracks emanating from several sites and later joining to form one primary crack front, are evident in Figure 88. Fatigue striations and shear lips are also visible in the fast-fracture zone. These fracture modes are indicative of the ductility and high toughness of this material. Other specimens, at maximum stresses of 100 KSI and 53 KSI, exhibited multi-crack origins and quite large fatigue zones (Figures 89 through 91). The microstructure (Figures 82 and 93) consists of a fine, spheriodal carbide particle distributed in a matrix of fine bainite and martensite. The grain size in the area of decarburization (Figure 92) was 3-5  $\mu\text{m}$ . Thus the grain size elsewhere in this specimen is below 3  $\mu\text{m}$ .

The SEM fractographs revealed quite ductile fracture modes with dimples and lamellar secondary cracks, also characteristics of warm-rolled material (Figures 94 through 96). Visual observation of a secondary crack which grew in a straight line into the specimen indicates a transgranular propagation mode. All of these micrographic results are summarized in Table III.





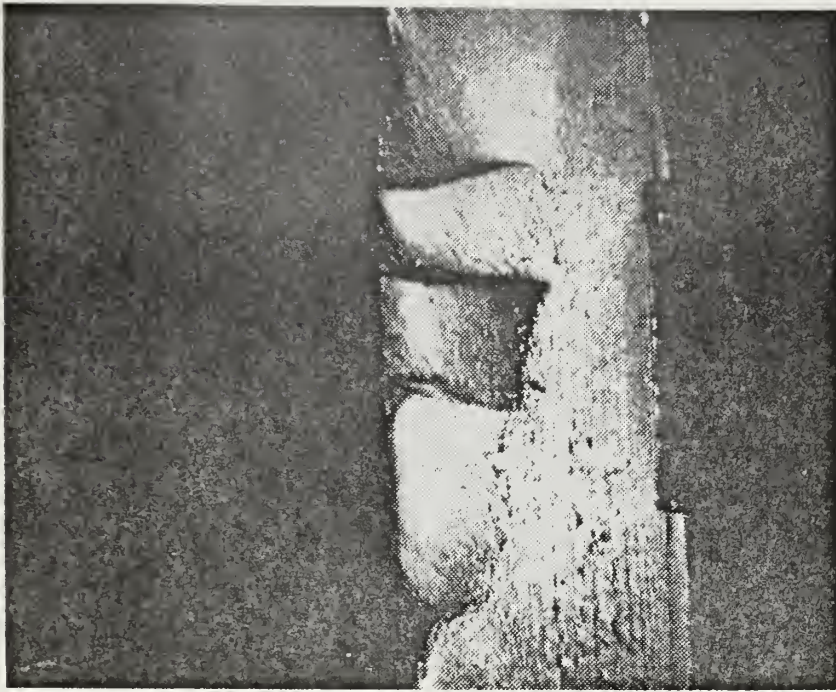


Figure 88. Macro-fractograph of specimen RI-2-2 which was fractured after 36,700 cycles at 100 ksi, showing that fatigue cracks emanate from several sites (left edge) and later join to form one primary crack front (Ratchet marks). Also, fatigue striations occupy the entire area of fast fracture. X10.

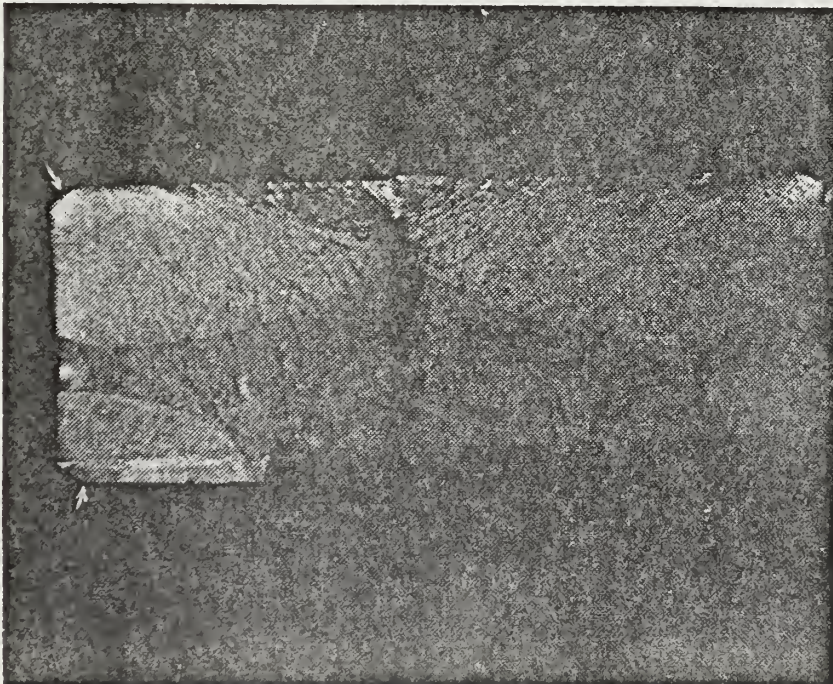


Figure 89. Macro-fractograph of a specimen RI-2-5, fractured after 20,500 cycles at 100 ksi, showing several crack initiation sites (arrows) and several fatigue zones. X10.







Figure 90. Macro-fractograph of a specimen RI-2-6 which was fractured after 215,700 cycles at 53 ksi, showing that the fatigue zone occupies almost the entire fracture surface. This means that this material has good fracture toughness and fatigue performance. X10.

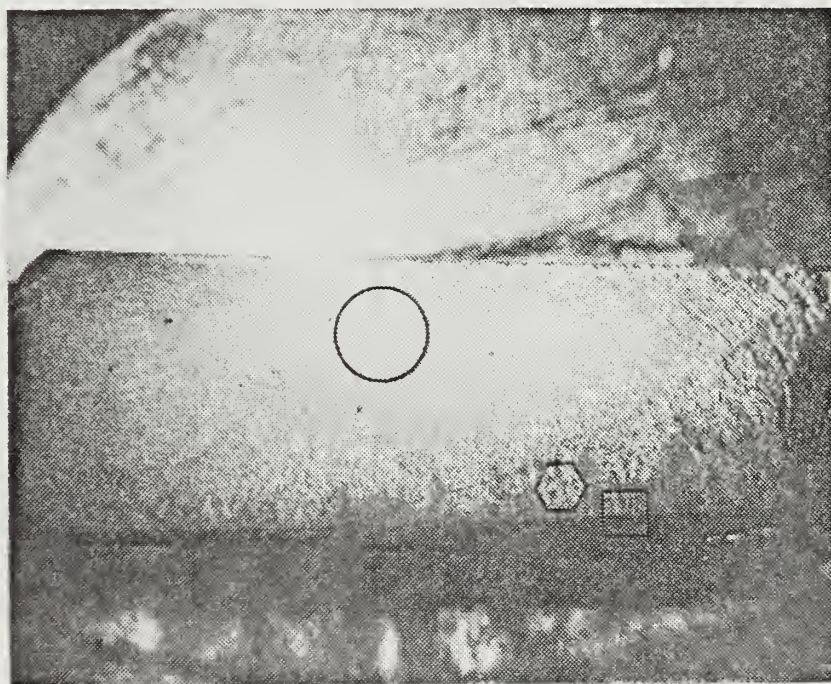


Figure 91. Macro-fractograph of a specimen RI-2-3 which was fractured after 477,600 cycles at 65 ksi. The entire area, except upper right hand corner, is a fatigue zone. Fatigue striations are evident at lower left corner. X10.





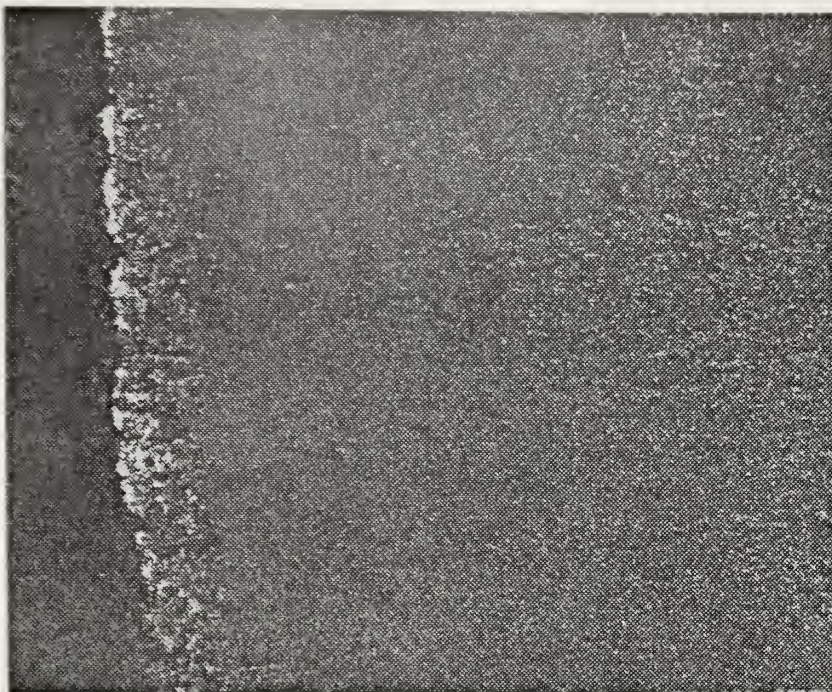


Figure 92. Micrograph of a specimen RI-2-3, showing decarburized layer around a drilled hole in the specimen. Grain size is evident, and is 3-5  $\mu\text{m}$ . X100.

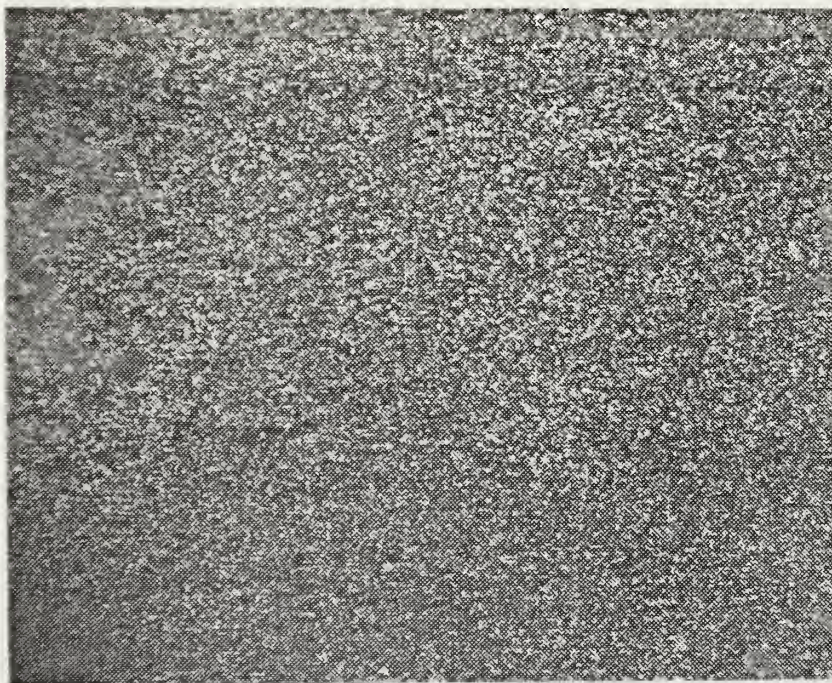


Figure 93. Higher magnification view of Fig. 92 micrograph, showing spheroidal, fine carbide particle distribution in a matrix of fine bainite and some martensite. X400.





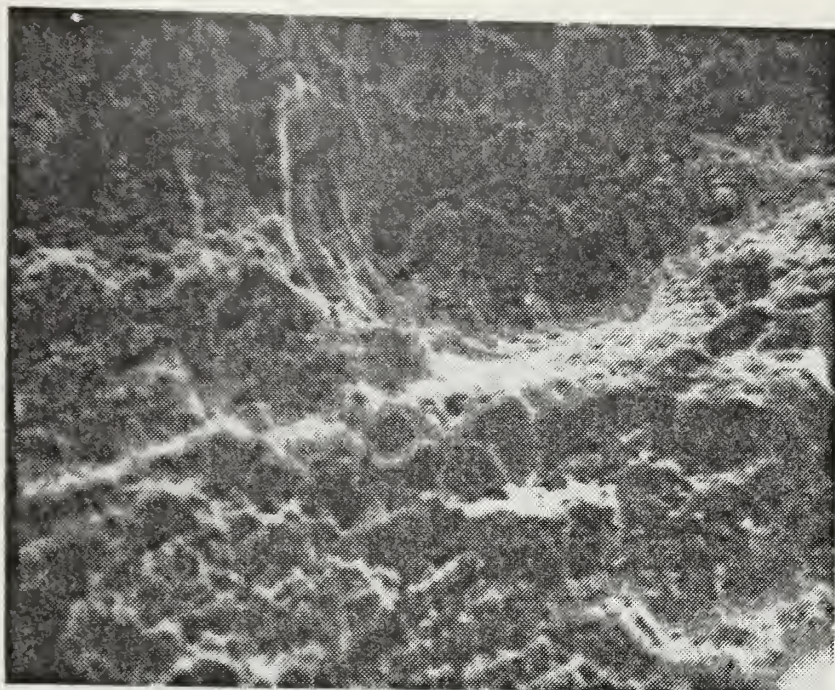


Figure 94. Area outlined by circle in micrograph of Fig. 91, showing mostly ductile fracture with dimples and tear ridges. X1100.

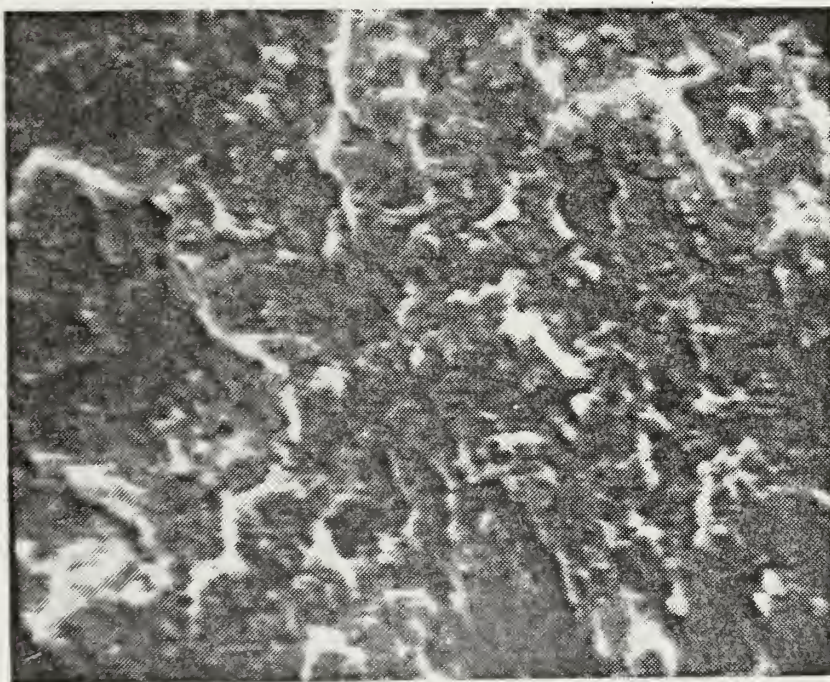


Figure 95. Higher magnification of upper area of Fig. 94 fractograph, showing lamellar secondary cracks, also characteristics of warm-rolled material. X2000.





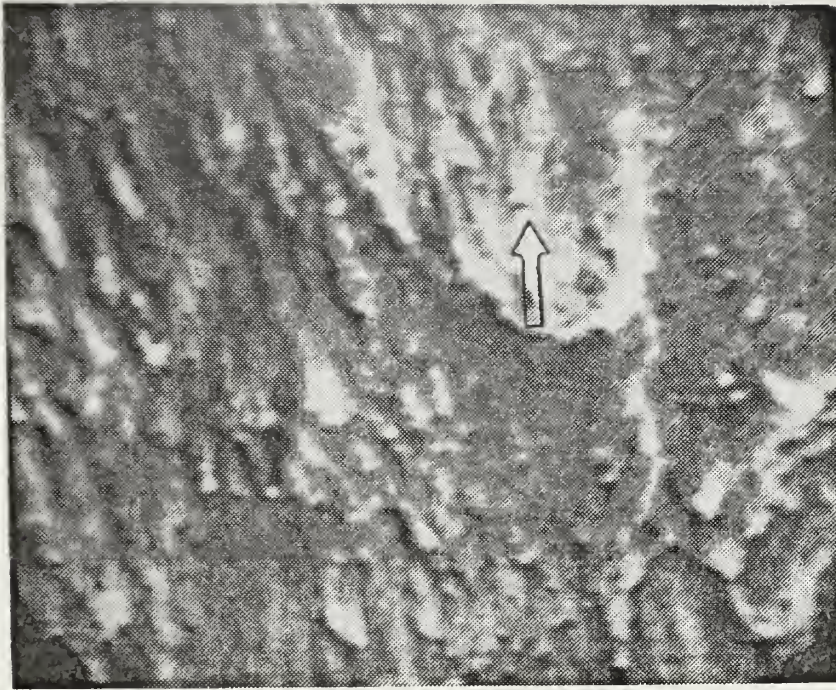


Figure 96. Area outlined by a hexagon, which is the fast fracture zone of Fig. 91 micrograph, showing radial marks which indicate the direction of fracture propagation (arrow). X2000.





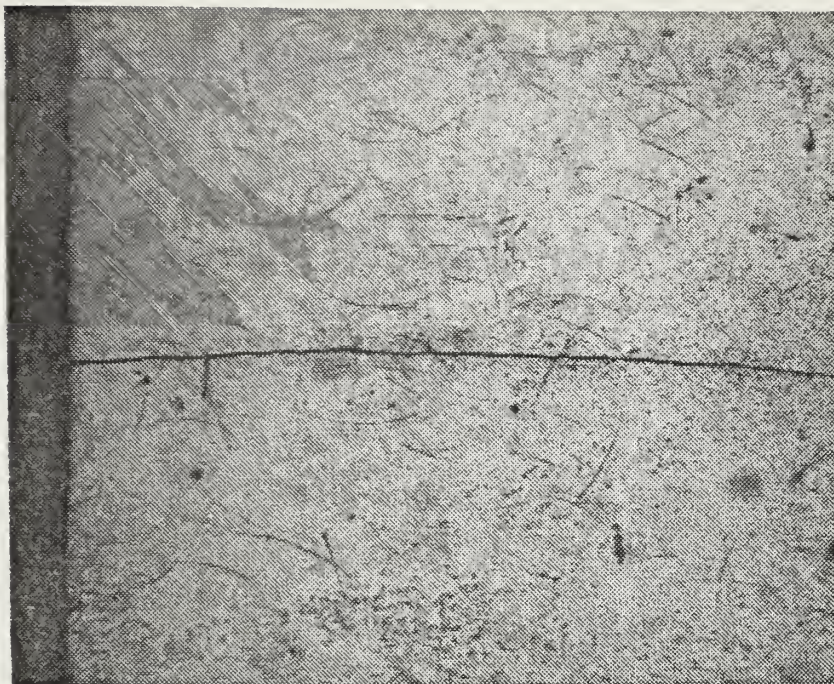


Figure 97. Macrograph of surface of specimen RI-2-8 showing a secondary crack. The surface was polished only. Short curves are polishing scratches and fine dispersed carbide particles are evident. X100.

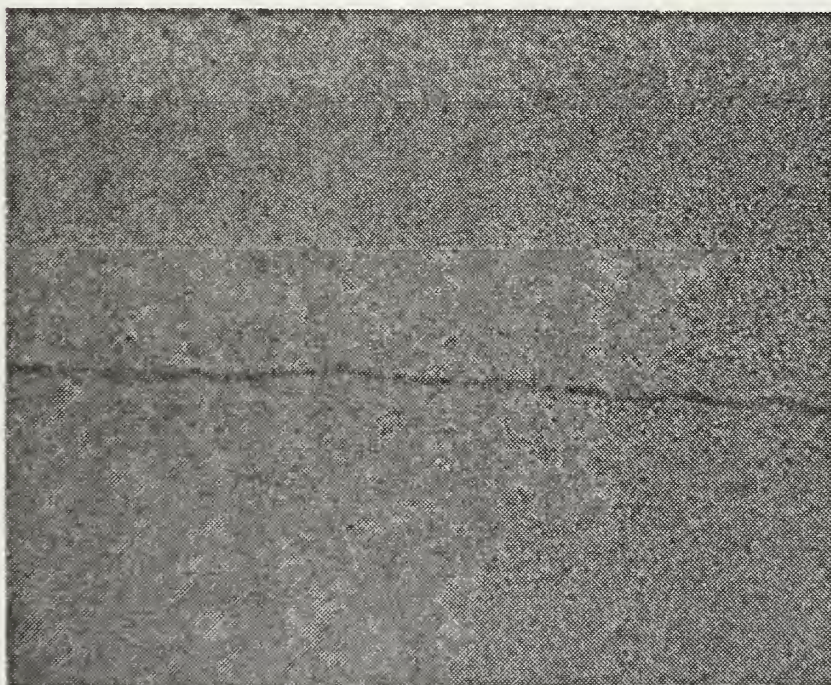


Figure 98. Higher magnification view of the same surface as in Fig. 97, polished only, showing spheroidal carbide particles. X400.







Figure 99. Same micrograph of Fig. 98 but etched by 2% nital + 2% picral solution for 10 seconds, showing that the secondary crack is transgranular. X400.



TABLE III

## COMPARISON OF FRACTOGRAPH OF EACH SPECIMEN GROUP

Specimen Group	Crack Origin	Roughness of Fracture Surface	Fracture Mode	Fatigue Zone	Micro-Structure
AR-1	one or two	irregular, coarse	ductile, brittle	present	fine carbide particles dispersed on fine ferrite matrix
AR-2	several	irregular, coarse	ductile, brittle	present	
AR-3,4	one or two	intermediate	ductile, brittle	present	
AR-5	one	irregular, coarse	ductile, brittle	present	
QT	one	intermediate	brittle	absent	coarse spheroidal carbide and tempered martensite
RQ	one	smooth	ductile, brittle	absent	fine spheroidal carbide and fine tempered martensite
QI	one	coarse	brittle, intergranular	absent	coarse bainite
RI-1	one	smooth	ductile, brittle	present	fine spheroidal carbide, fine bainite and martensite
RI-2	several	smooth	ductile	present	





## 7. Tensile Test Specimens

Macro-fractography of a tensile specimen from the RI-2 specimen group showed a fractograph typical of ductile material, i.e., a fibrous zone in the center area, a radial zone and large shear lips (Figure 11). Considering its tensile strength and yield strength, 258 KSI and 231 KSI, respectively, the ductile fracture mode was unexpected. The SEM fractography confirmed the ductile fracture mode and transgranular fracture path with the presence of various size dimples as shown earlier in Figures 12 through 15. The macro-fractograph of a tensile specimen of the RQ specimen group showed the crack origin to be at the surface of the specimen (Figure 100). The SEM fractograph, in Figure 101, revealed a prior quenching micro-crack at the crack origin on the fracture surface. The larger magnification SEM fractographs showed a quite brittle fracture mode with cleavage facets and microvoid coalescence (Figures 102 through 105).



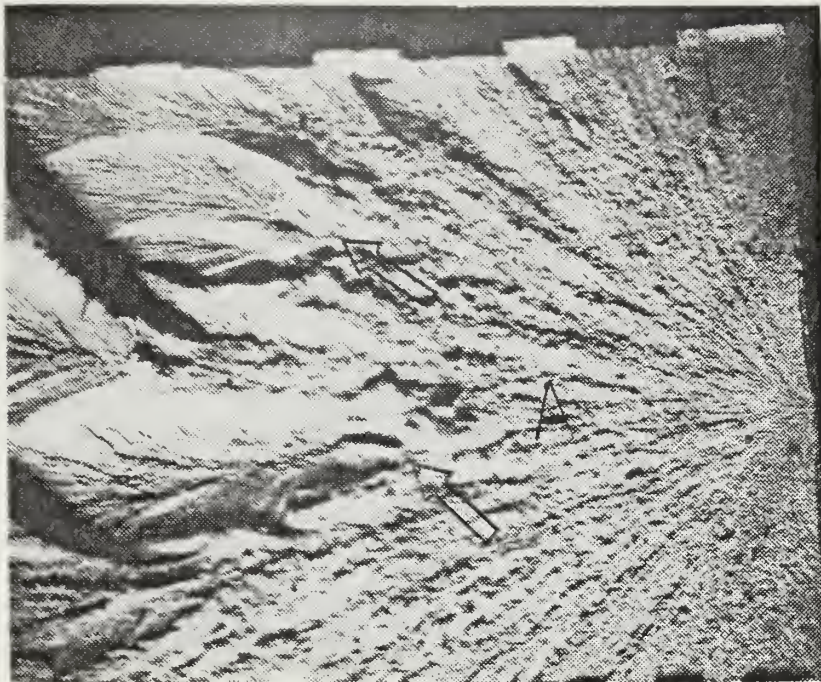


Figure 100. Macro-fractograph of a tensile test specimen from specimen group RQ showing that fracture initiates from the surface of specimen. Chevron marks on fibrous zone (A) are evident. Two tear-drop shaped concave fractures means that crack halted at the root (arrow) of the tear drop. X18.

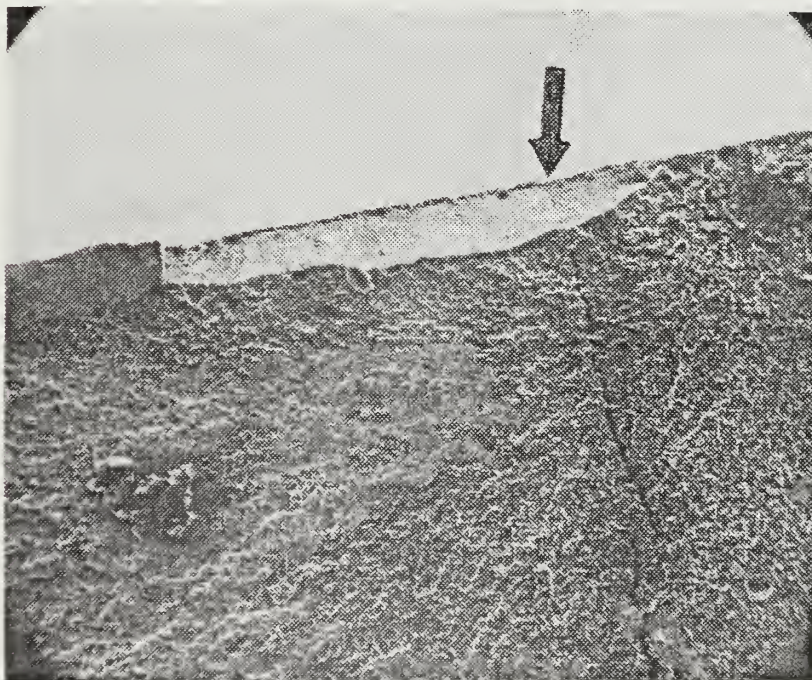


Figure 101. SEM fractograph of Fig. 100 is the vicinity of crack origin (arrow), the site of a quenching crack. The upper white area is a concaved shear lip zone. X200.





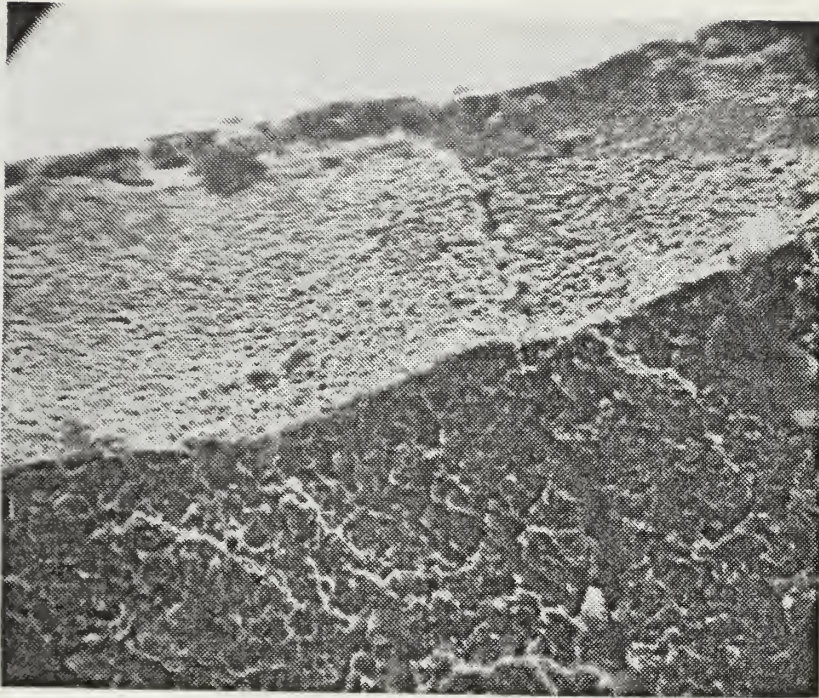


Figure 102. Higher magnification view of the crack origin in Fig. 101. Fracture surface shows quasi-cleavage facets with tear ridges. Deep quenching crack is evident. X1000.

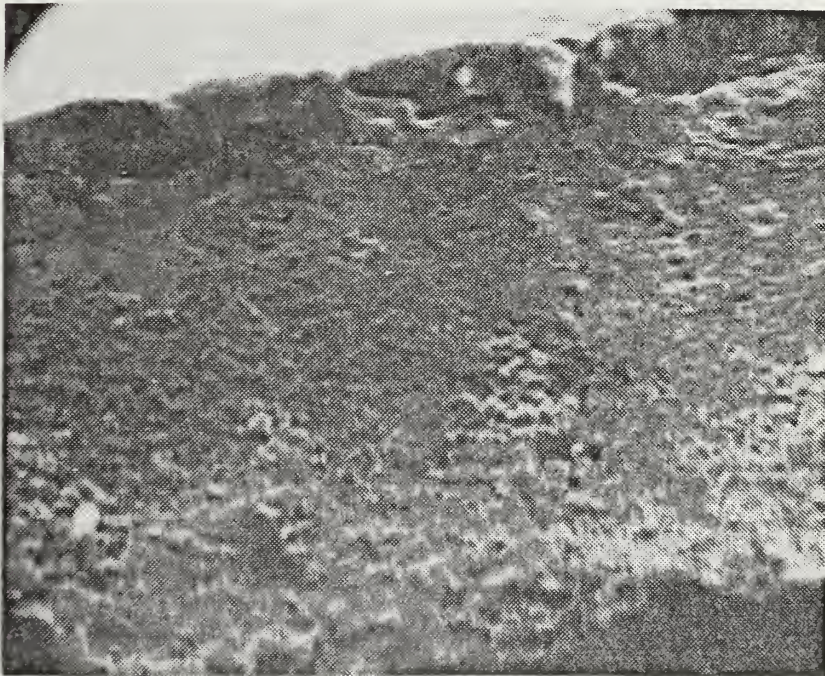


Figure 103. Higher magnification view of Fig. 102 in concaved shear lip zone. Fine microvoids are visible. X5000.





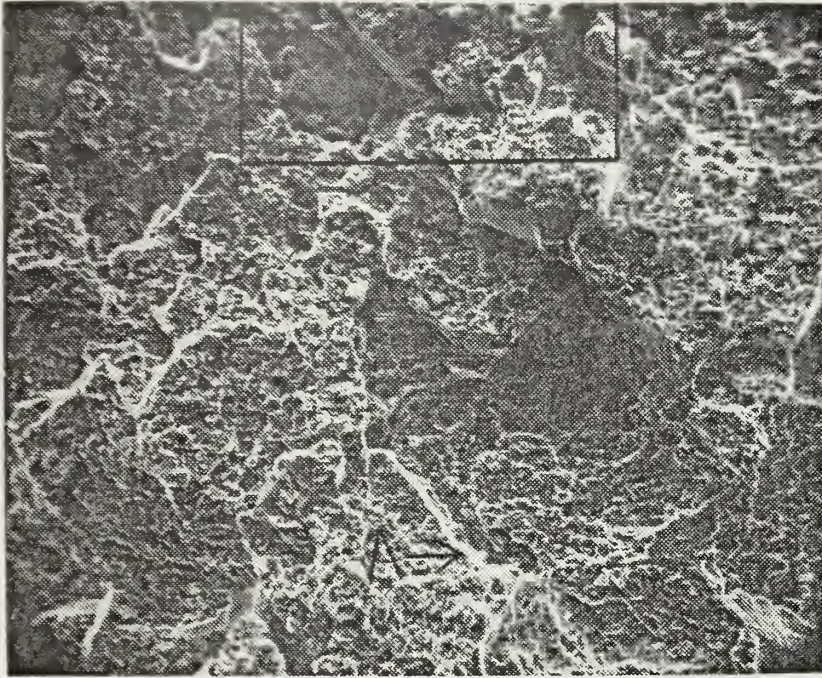


Figure 104. Fractograph of the fibrous zone of Fig. 100, showing tear ridges (A) and cleavage facets with some equiaxed dimples. Fracture surface shows brittle and ductile fracture. X500.

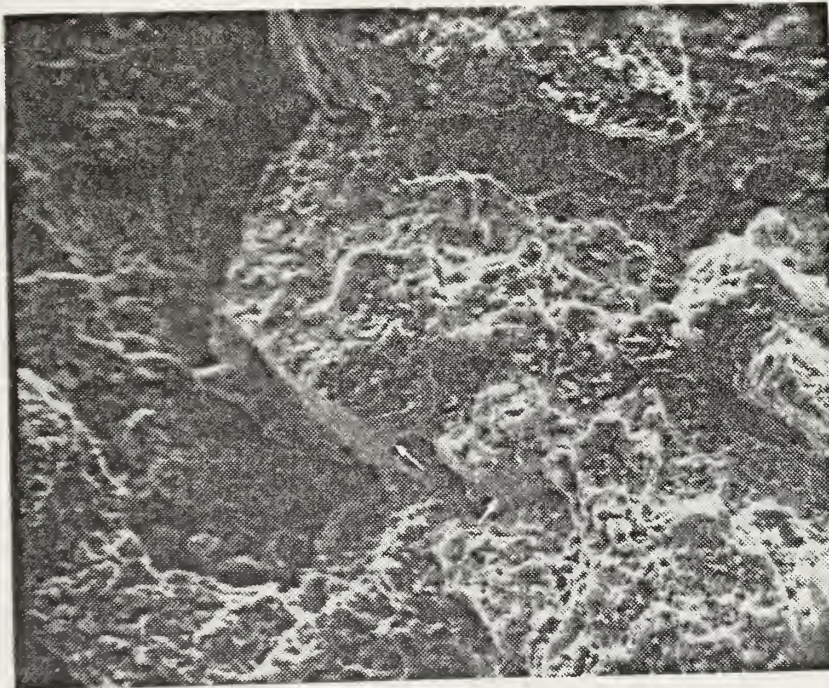


Figure 105. Area outlined by rectangle in Fig. 104 fractograph at higher magnification, showing cleavage facets (arrow) and dimples. X1000.





#### IV. DISCUSSION

##### A. GENERAL

The fatigue behavior of a material is the result of a complex interaction of a number of metallurgical factors including strength, crystal structure resistance to crack propagation and grain size. The fine-grained structures, produced in the "Sherby processed" high-carbon steel, coupled with the inherent toughness of these materials, suggested the possibility of significant improvement in fatigue properties. This study was, therefore, undertaken to evaluate these structural effects on the fatigue properties of these materials.

##### B. EFFECTS OF THERMOMECHANICAL PROCESSING ON MICROSTRUCTURE AND MECHANICAL PROPERTIES

The fatigue properties of metals are quite structure sensitive. Thus, fatigue properties can often be improved by producing the optimum structure often involving special heat treatment. The structural sensitivity of the fatigue limit of a plain carbon eutectoid steel can be seen in a material that is heat treated either to coarse pearlite or to spheroidite of the same tensile strength. Even though the steel in the two structural conditions have the same tensile strength, the pearlite structure results in a significantly lower fatigue limit due to the more severe notch effects of the pearlitic carbide lamellae [14]. J. C. Grosskreutz [15] proposed that high fatigue resistance can be achieved by homogenizing slip



deformation so that local concentrations of plastic deformation are avoided. This is in agreement with the observation that fatigue strength is directly proportional to the difficulty of dislocation cross slip. Grain size has its greatest effect on fatigue life in the low-stress, high-cycle regime in which Stage I cracking predominates [11]. In general, quenched and tempered microstructures result in the optimum fatigue properties in heat-treated, low-alloy steels. F. Borik and R. D. Chapman [16], however, demonstrated that a bainitic structure produced by austempering results in better fatigue properties than a quenched and tempered structure with the same hardness.

It is of interest, then, to compare the results of this study of microstructural effects on the fatigue behavior of 52100 steel. Figure 106 is a plot of endurance limit versus hardness for each specimen group. In the AR specimen group, the endurance limit increased linearly with increasing hardness. The highest value of the endurance limit was provided by the RI-2 specimen group (rolled and isothermally transformed with a hardness of HRC 44). The endurance limit was expected to increase with increasing hardness.

Hardness is related to tensile properties and endurance limit is often found to be a constant function of the strength for a given material. However, the higher hardness specimen groups QI, QT and RQ show drops in endurance limit. The endurance limit to yield-strength ratios (the fatigue ratios) in QI, QT and RQ specimen groups was below 0.15, while that of the AR and RI-2 specimen groups was above 0.41. The apparent reason for the premature failure of the





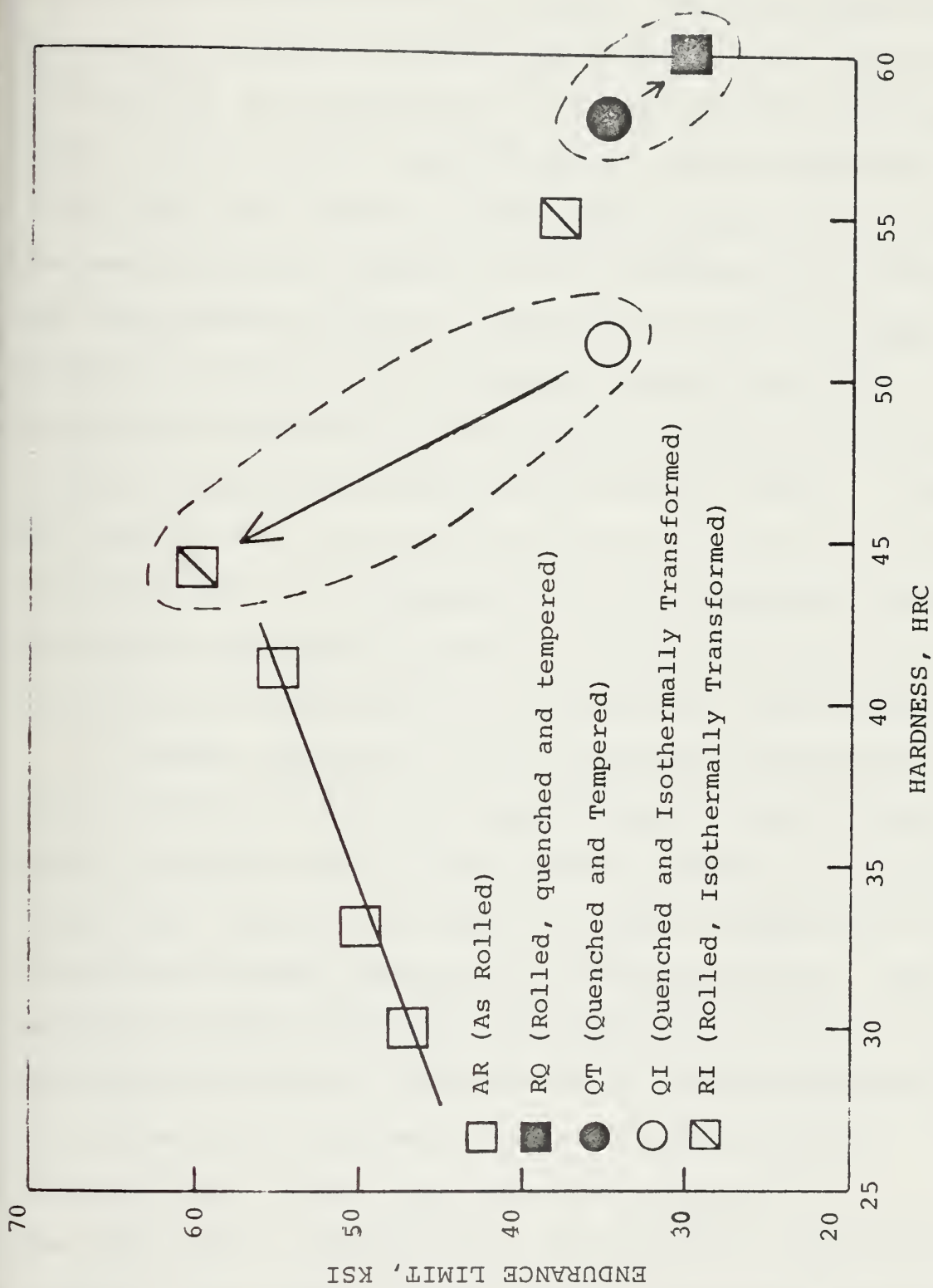


Figure 106. Plot of endurance limit versus hardness for each specimen group.



quenched specimens is the stress-concentration effects of either a thin carbide film that forms during the tempering of the martensite structure or micro-quenching cracking. The isothermal mechanical processing (rolling) improved the endurance limit from 35 KSI to 60 KSI in the quenched and isothermally transformed specimen group. It is evident from the results of the experiments in this study that finer grain size and higher hardness can be obtained by decreasing rolling temperature and increasing total rolling strain. The fine microstructures in isothermally rolled specimens were difficult to resolve using standard optical techniques. Because of the difficulty of etching these fine structures, scanning electron microscopy was not useful either. In addition, the fine bainitic structures produced by subsequent isothermal transformation heat treatment could not be properly delineated. Thin film transmission electron microscopy is required to fully characterize the structure of this extremely fine grained material.

To discuss the effect of the isothermal mechanical processing on cycles-to-failure at fixed maximum stress, a plot of cycles to failure (at 100 KSI) versus hardness is provided in Figure 107. Cycles-to-failure is in part a measurement of resistance to crack propagation in fatigue testing. The other component is the number of cycles required to initiate a crack. The cycles-to-failure increased with increasing material hardness for the as-rolled specimens. Higher hardness material resulted from a finer grain structure produced at the lower rolling temperature. The isothermal mechanical process (rolling) improved the fatigue life for specimens further processed





both by quenching and tempering and by quenching and isothermal transformation.

The standard austenitizing and quenching process involves carbide dissolution, austenite grain growth and martensite formation on cooling. This results in a material which is hard and strong but which has reduced fatigue life--at least in this series of tests. This decrease in fatigue life could be attributed to austenite grain growth and resulting coarse martensitic microstructures. The presence of micro-quench cracking is another reason for the sudden drop in both high and low stress in fatigue test. Figure 108 revealed grain growth during austenitizing and micro-quench cracking which propagates intergranularly.

The RI-2 specimen group processed by isothermal rolling and isothermal transformation results in the best endurance limit and good tensile strength and ductility. The rolling process broke down the carbide into fine particles and these dispersed fine carbide particles hold down austenitic grain growth and also require less time in intercritical temperature range (austenite and cementite). The isothermal transformation process results in a fine bainitic structure. The combination of this fine-grained bainitic structure and fine, dispersed carbide particles promise the best fatigue performance, strength, and toughness.



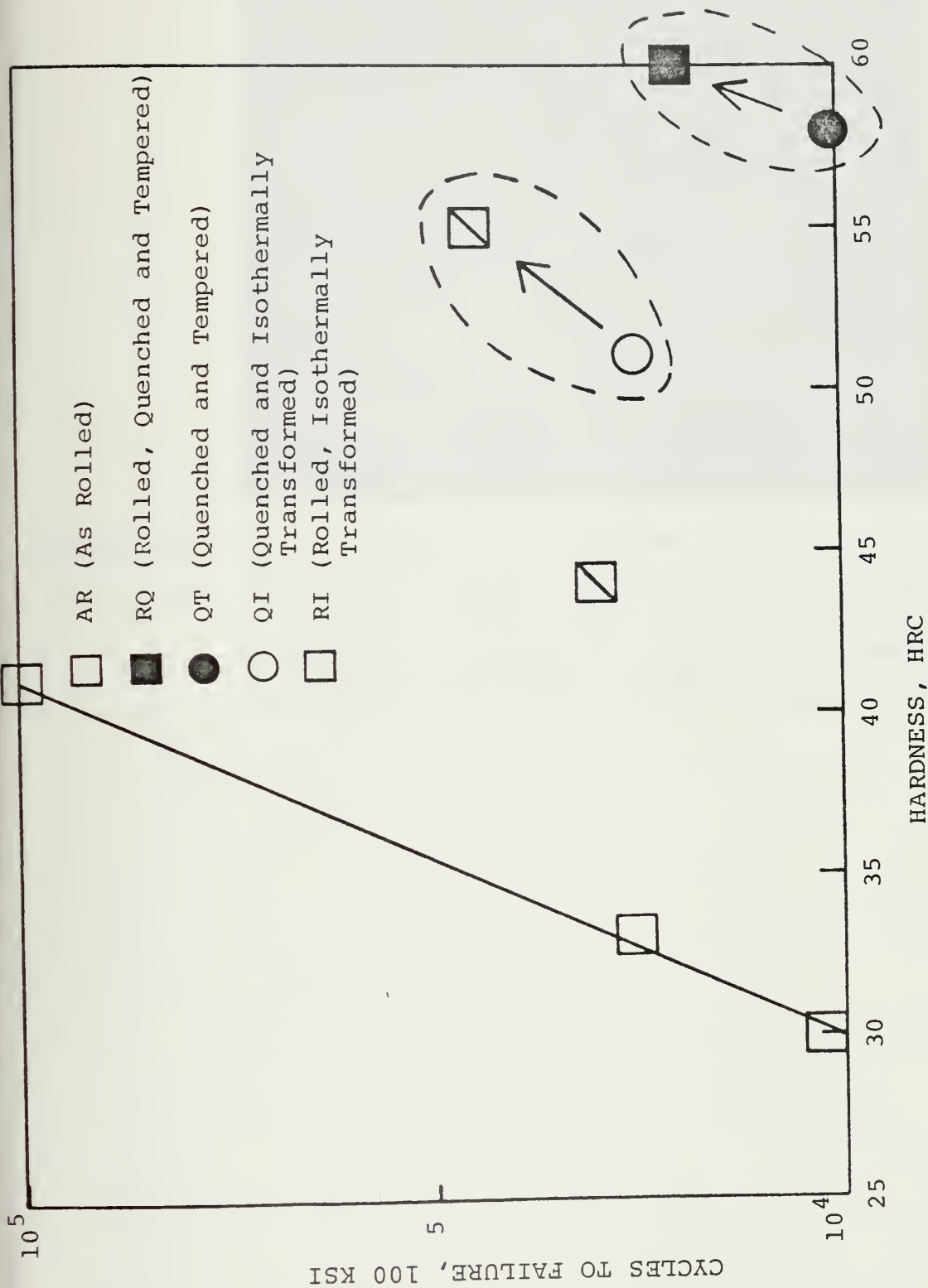


Figure 107. Plot of cycles to failure versus hardness for each specimen group.







Figure 108. Microstructure of a specimen from group AR-3, after oil quenching and before rolling, showing a quenching crack. Crack propagates intergranularly. Austenitized grain size can be inferred from the crack route; the martensitic structure is visible. Etched with 2% nital + 2% picral solution, 10 seconds. X400.



## V. CONCLUSIONS

Based on the experimental observations and results, the following conclusions are made:

1. The isothermal rolling process, resulting in the combination of an apparently fine ferrite grain size with a dispersion of fine carbides, improve the fatigue resistance of AISI 52100 steel under both low cycle and high cycle conditions. The lower finish rolling temperature provided the greatest improvement.

2. The presence of an extremely fine distribution of carbides produced by the isothermal deformation process is effective in refining the austenitic grain size of intercritically annealed high carbon steels and results in a significant change in resulting transformation products. A transformation product refinement is produced and an additional fine, carbide phase is present.

3. The combination of isothermal rolling and isothermal transformation results in the best endurance limit and good tensile strength and ductility.

4. Quenching and tempering of AISI 52100 steel produced the worst fatigue resistance as micro-quenching cracks resulted, with carbide films at the grain boundary.

The further optimization of these structures holds promise for a variety of applications requiring a combination of high strength, wear resistance, fatigue life, and toughness.





## VI. RECOMMENDATION FOR FURTHER RESEARCH

The encouraging results obtained from the steel, in rolled and isothermally transformed conditions, suggest that many possibilities exist for achieving higher toughness, hardness and fatigue performance. Variations of finish rolling temperature should be investigated since increased hardness and significantly improved fatigue life, both in low and high cycle fatigue performance, were observed at lower finish rolling temperature. Quenching and tempering processes were not encouraging in this series of test. The lowest austenitizing temperature should be used to prevent micro quench cracking and grain growth. More detailed structural analysis should be undertaken in conjunction with further heat treatment and other property studies. To optimize hardness, toughness, and fatigue life, recommendations are summarized as follows:

1. Combinations of various rolling temperature and isothermal transformation temperatures.
2. Reverse of sequence of heat treatment process in rolling and isothermal transformation processes to give alternate initial starting structures.
3. Alternate alloy compositions designed to modify the amount and stability of carbides could then be explored.



## LIST OF REFERENCES

1. Goesling, W. H., Ballistic Characterization of Ultra-High Carbon Steel, M.S. Thesis, Naval Postgraduate School, Monterey, California, 1977.
2. Rowe, D., and Hamilton, D. R., The Microstructural, Mechanical and Ballistic Characterization of Ultra-High Carbon Steel, M.S. Thesis, Naval Postgraduate School, 1977.
3. Hillier, R., Evaluation of Superplastic Ultra-High Carbon Steel as Armor Plate for Critical Component Protection, M.S. Thesis, Naval Postgraduate School, Monterey, California, 1979.
4. Martin, R. R. and Phillips, J. W., Ballistic Performance, Shear Band Formation and Mechanical Behavior of Thermo-Mechanically Processed Ultra-High Carbon Steel, M.S. Thesis, Naval Postgraduate School, 1978.
5. Taylor, J. L., Fracture Toughness Characterization of Selected Ultra-High Carbon Steels, M.S. Thesis, Naval Postgraduate School, Monterey, California, 1979.
6. Sherby, O. D. and others, "Development of Fine Spheroidized Structures by Warm Rolling of High Carbon Steels," Transactions of the ASM, V. 62, 1969.
7. Third Semi-Annual Progress Report to Advanced Progress Research Agency under Grant DAHC-15-73-G15, Superplastic Ultra-High Carbon Steels, Stanford University Press, by O. D. Sherby and others, February 1975.
8. Metals Handbook, 8th Ed., V. 10, American Society for Metals, 1975.
9. Ransom, J. T., "The Effect of Inclusions on the Fatigue Strength of SAE 4340 Steels," Transactions of the ASM, V. 46, pp. 1254-1269, 1954.
10. ASTM Report 73, Tension, Compression, and Fatigue Properties of Several Steels for Aircraft Bearing Applications, by G. Sachs and others, 1959.
11. Dieter, G. E., Mechanical Metallurgy, pp. 403-449, McGraw-Hill, 1976.





12. NASA Technical Note D-7033, Rolling-Element Fatigue Lives of Four M-Series Steels and AISI 52100 at 150°F, by Parker, R. J., Zaretsky, E. V., Dietrich, M. W., February 1971.
13. Kar, R. J., Optimization of Strength and Toughness in a High Carbon Steel, M.S. Thesis, University of California, Berkeley, California, 1976.



# INITIAL DISTRIBUTION LIST

	No. Copies
1. Defense Technical Information Center Cameron Station Alexandria, Virginia 22314	2
2. Library, Code 0142 Naval Postgraduate School Monterey, California 93940	2
3. Department Chairman, Code 69 Department of Mechanical Engineering Naval Postgraduate School Monterey, California 93940	1
4. Associate Professor T. R. McNelley, Code 69Mc Department of Mechanical Engineering Naval Postgraduate School Monterey, California 93940	5
5. Adjunct Associate Professor D. H. Boone, Code 69B1 Department of Mechanical Engineering Naval Postgraduate School Monterey, California 93940	5
6. CDR Ik Sik Chung Bureau of Ordnance of Naval HQ Daebang-dong, Kwamak-ku, Seoul, KOREA	10









Thesis  
C47845 Chung  
c.1

188009

The influence of  
thermomechanical pro-  
cessing and heat  
treatment on the fa-  
tigue resistance and  
fractographic charac-  
teristics of a high-  
carbon bearing steel.

Thesis  
C47845 Chung  
c.1

188009

The influence of  
thermomechanical pro-  
cessing and heat  
treatment on the fa-  
tigue resistance and  
fractographic charac-  
teristics of a high-  
carbon bearing steel.



thesC47845  
The influence of thermomechanical proces



3 2768 002 10423 4  
DUDLEY KNOX LIBRARY